



TECHNISCHE  
UNIVERSITÄT  
WIEN

Vienna University of Technology

## DIPLOMARBEIT

# Surface Proton Dosimetry and its clinical application

zur Erlangung des akademischen Grades

## Diplom-Ingenieurin

im Rahmen des Studiums

**Biomedical Engineering**

an der Technischen Universität Wien

ausgeführt am

Atominstitut

Fakultät für Physik

Technische Universität Wien

in Zusammenarbeit mit der

Universitätsklinik für Strahlentherapie

Medizinische Universität Wien und MedAustron

durch

**Andrea Balz, BSc**

Matrikelnummer 01025332

Betreuer: **Univ.-Prof.DI.Dr. Dietmar Georg**

Mitwirkung: **Mag. Barbara Knäusl, PhD**

Wien, 22.10.2018

\_\_\_\_\_  
Unterschrift Studentin

\_\_\_\_\_  
Unterschrift Betreuer



## **Acknowledgement**

First of all, I would like to thank Univ.-Prof. DI Dr. Dietmar Georg for supervising me in the course of this thesis. I'm grateful for getting the opportunity to gain experience at the Department of Radiotherapy of the Medical University of Vienna.

Furthermore I want to thank Mag. Barbara Knäusl, PhD for her tireless support, patience and time. Additionally, I would like to thank all people from the Medical University Vienna and MedAustron I had the chance to work with. Special thanks go to Mag. Peter Kuess, PhD, Hugo Palmans, PhD, Dr. Monika Clausen, Andreas Resch, MSc and Natalia Kostiukhina, MSc for providing advice and assistance for any kind of questions.

Moreover, I want to thank my family for the support during my studies.

## **Statutory declaration**

I declare that I have authored this thesis independently, that I have not used other than the declared sources / resources, and that I have explicitly marked all material which has been quoted either literally or by content from the used sources.

Vienna, October 2018



# Kurzfassung

In der Strahlentherapie werden Protonen und Kohlenstoffionen vor allem zur Behandlung von komplex geformten Tumoren, die sich in der Nähe von strahlenempfindlichen Organen befinden, verwendet. Im Vergleich zur konventionellen Strahlentherapie mit Photonen kann mit Protonen die Energieabgabe im Gewebe weit besser kontrolliert werden. Der Hauptteil der Energie wird am Ende der Reichweite des Strahls, im so genannten Bragg-Peak, abgegeben. Das führt zu einer verbesserten Treffgenauigkeit, Schonung von umliegenden Organen und Gewebe, und somit zur Reduktion möglicher Nebenwirkungen.

Auch oberflächlich gelegene Tumore können von Ionentherapie profitieren. Dabei muss besonders die Haut vor einer Überdosierung geschützt werden, da die Protonendosis direkt an der Oberfläche höher ist als bei Photonen. Dies kann in der Dosisberechnung berücksichtigt und mit Messungen überprüft werden.

In dieser Arbeit wurde der Dosisaufbau eines Protonenstrahls an der Oberfläche *in vitro* untersucht. Die verwendeten passiven und aktiven Dosimeter – radiochromatische Filme und Ionisationskammern – wurden an der Oberfläche und innerhalb von wasserequivalenten Platten positioniert und mit unterschiedlichen Protonenenergien und Dosen bestrahlt. Weiters wurde die Auswirkung eines Range Shifters (RS) im Strahlengang untersucht.

In den Messungen wurden radiochromatische Filme vom Typ EBT3 (Ashland, Bridgewater, NJ, USA), die Advanced Markus Ionisationskammer und die Roos Elektronenkammer, beide von PTW (Freiburg, Deutschland), verwendet. Die Filme wurden vor und nach der Bestrahlung mit dem Expression 11000XL Graphik-Scanner der Seiko Epson Corporation (Nagano, Japan) gescannt und unter Referenzbedingungen kalibriert (8 cm × 8 cm Feldgröße in 2 cm wasserequivalenter Tiefe). Der Range Shifter aus 3 cm dickem Polymethylmethacrylat (PMMA) wurde in einem Teil der Messungen verwendet, um den Bragg-Peak an die Oberfläche zu verschieben. Bestrahlt wurde mit Protonenenergien von 97.4 MeV, 179.2 MeV und 195.2 MeV, teils mit RS. Alle Messungen wurden mit und ohne Filme mit Dosen von 0.5 Gy, 1 Gy und 2 Gy, und unter zwei verschiedenen Einstrahlwinkeln, 0 und 20 Grad, durchgeführt. Um den oberflächlichen Dosisaufbau genau zu untersuchen, wurden die EBT3-Filme in Stapeln von 1 bis 8 Filmen geordnet. Diese wurden an der Oberfläche der wasserequivalenten RW3-Platten (PTW, Freiburg, Deutschland) angebracht, wobei direkt dahinter die Markuskammer montiert wurde (aus der Strahlperspektive gesehen). Die Filmresultate wurden mit den Ergebnissen der Markuskammer und Monte Carlo Dosissimulationen mit Gate (v8.0)/Geant4.10.03.p1 verglichen. Für Vergleichsanalysen wurden die gemessenen Dosen zur Eintrittsdosis normalisiert.

Die Oberflächendosismessungen ergaben eine Übereinstimmung der Filmdosen mit den Markusammer-Ergebnissen innerhalb von 1.5 % für eine geplante Dosis von 2 Gy und unter Verwendung der entsprechenden Kalibrierkurven und Korrekturfaktoren. Bei Verwendung des Range Shifters wird der Abstand der Patienten- oder Phantomoberfläche zum Bestrahlungskopf so weit als möglich verringert, um eine Aufweitung der Spotgröße zu verhindern. Der Einfluss von Strahlverbreiterung und Streuung durch den Range Shifter lag in den Messungen bei bis zu 8 %. Die Verkürzung der Strahlreichweite durch den Range Shifter funktioniert gut und hat keinen Einfluss auf den Dosisverlauf, wie der Vergleich der skalierten Tiefendosiskurven bei 179.2 MeV ohne RS und 195.2 MeV mit RS für Filme und Markusammer zeigte. Um zu überprüfen, ob der Kurvenverlauf des Dosisaufbaus für beliebige Energien vorhergesagt werden kann, wurde ein einfaches Modell, basierend auf den Messungen der verschiedenen verwendeten Energien, erstellt. Es erlaubt die ungefähre Vorhersage der Tiefendosiskurve in Tiefen von 0 bis 2 mm für klinisch verwendete Energien und eine geplante Dosis von 2 Gy mit einer Abweichung von weniger als 1 %. Die Film- und Markusammer-Messungen mit einem um 20° gedrehten Phantom ergaben eine um ungefähr 8 % niedrigere Dosis im Vergleich zur geraden Oberfläche. Die geeigneten Filme zeigten einen starken Dosisverlust von bis zu 30 % in der rechten Filmhälfte, vermutlich verursacht durch Feldinhomogenitäten aufgrund des für diesen Winkel zu kleinen Bestrahlungsfeldes. Monte Carlo Simulationen wurden zum Vergleich herangezogen.

Die zweite Aufgabe in dieser Arbeit war die Erstellung von Bestrahlungsplänen für weit ausgedehnte Extremitätensarkome, die mindestens zwei sich überlappende Protonenfelder für die Volumenabdeckung benötigen. Sarkome befinden sich immer in Oberflächennähe, wodurch die Hautdosis vor allem im Überlappungsbereich hohe Bedeutung hat. Mithilfe des Planungssystems RayStation v6.99 wurden klinisch akzeptable Bestrahlungspläne erstellt und hinsichtlich ungewollter Patientenbewegung und Positionierungsungenauigkeiten untersucht. Im Rahmen der Analyse der Robustheit wurden separat eingezeichnete Teile des Tumors um jeweils 5 mm zu- und gegeneinander verschoben. Die Auswirkungen wurden anhand der Volumenabdeckung mithilfe von  $D_{50\%}$ ,  $D_{98\%}$  und  $D_{2\%}$  beurteilt. Die Hautdosis wurde für nominelle und verschobene Pläne verglichen und mittels  $V_{60\text{Gy(RBE)}}$ ,  $D_{98\%}$  und  $D_{2\%}$  analysiert, wobei zum Beispiel das Volumen  $V_{60\text{Gy(RBE)}}$  eine Grenze von 4 cm<sup>3</sup> nicht überschreiten sollte. Die Robustheits-Analyse ergab teils grobe Probleme bei der Abdeckung des Zielvolumens mit ausreichend Dosis, vor allem im Fall des größten Tumorumfanges mit 4.2 Litern, das mit drei Strahlungsfeldern geplant wurde. Generell ergaben die zueinander verschobenen Tumorteile, wie erwartet, eine Ansammlung der Dosis im Überlappungsbereich der Tumorfelder, während die oberen und unteren Enden des Planungsvolumens weniger Dosis erhielten. Jener Plan, der im nominellen Fall schon eine homogene Dosisverteilung gezeigt hatte –  $D_{98\%}=98\%$  bei einem Volumen von 0.4 Litern – schnitt auch bei der Robustheits-Analyse am besten ab. Allerdings enthielt er mit 16.6 % auch den größten prozentuellen Hautanteil, was zu einer starken Überschreitung des klinischen Ziels führte: 80 % im nominellen Fall und mehr als 400 % bei den Störungsszenarien. Bei zwei weiteren Patienten mit Zielvolumina von 1.6 und 2.2 Litern wurde die klinische Zielsetzung

für die Haut in nominellen und verschobenen Plänen erfüllt, wobei die Dosisabdeckung des Zielvolumens gering war. Dosis-Volumen-Histogramme und Liniendosen bestätigten die Beobachtungen.

Zusammenfassend zeigten die Oberflächendosismessungen, dass der Range Shifter keinen signifikanten Einfluss auf die Form des Dosisaufbaus und die Film- und Markuskamerdosen an der Oberfläche hat. Ein einfaches Modell kann die ungefähre Form des Dosisaufbaus für Energien von 60 MeV bis 250 MeV vorhersagen. Weiters wurde gezeigt, dass eine Annäherung an die reale Patientengeometrie mit geneigten oder gerundeten Oberflächen zu erheblichen Problemen bei der Dosisabgabe und -messung führen kann. Obwohl die Ursache für die starken Dosisabweichungen entlang der Filmbreite teilweise auf ein zu klein gewähltes Bestrahlungsfeld zurückgeführt werden konnte, ist eine deutlich intensivere Untersuchung des beobachteten Effekts notwendig.

Bei der Erstellung der Bestrahlungspläne für die Extremitätensarkome und die Untersuchung der Robustheit gegen Positionsunsicherheiten wurde in allen nominellen Plänen eine akzeptable Dosisabdeckung des Zielvolumens realisiert. Da fast alle Sarkome einen Hautanteil von 9% oder mehr aufwiesen, war es schwierig, hier eine ausreichende Schonung zu erreichen. Im Rahmen der mit Unsicherheiten versehenen, verschobenen Szenarien traten Probleme bezüglich Dosisabdeckung des Zielvolumens, überhöhter Dosis und Schonung der Risikoorgane auf. Die auseinandergeschobenen Isozentren verursachten gröbere Dosisinhomogenitäten als die zusammengeschobenen Isozentren. Beim Patienten mit der größten Tumorlänge, der mit drei Bestrahlungsfeldern geplant wurde, ergaben die verschobenen Szenarien starke Über- und Unterdosierung im Planungsvolumen und über dessen obere und untere Grenzen hinaus. Generell scheint die Anwesenheit von Knochen mitten im Planungsvolumen signifikanten Einfluss auf die homogene Dosisverteilung und die Dosisabdeckung zu haben. Die Robustheit gegen Positionsunsicherheiten hängt nicht ausschließlich von der Größe des geplanten Überlappungsbereiches ab, sondern auch an der Dosis, die im Zielvolumen und in der Haut appliziert wird. Des Weiteren ist die Anwendung von mehr als zwei Bestrahlungsfeldern – falls es nicht unbedingt nötig ist – nicht zu empfehlen, da der zusätzliche Überlappungsbereich die Robustheit des Bestrahlungsplans zusätzlich beeinträchtigt.



# Abstract

In radiation therapy protons and carbon ions are the ideal choice for treating complex shaped tumors that are located close to critical organs at risk (OARs). In comparison to conventional radiotherapy using photons the dose delivery to tumor cells can be controlled much more effectively since the main part of the energy is deposited at the end of the particle range, the so-called Bragg peak. This improves the accuracy of hitting the tumor while the surrounding organs and normal tissue is spared, which helps reducing possible treatment related side effects.

Tumors that potentially profit from ion therapy can be centrally located as well as at the patients' surface. Due to the shape of the Bragg peak, ions deliver a higher dose to the surface, compared to photon depth dose curves. Combined with the reduced number of fields used in ion beam therapy there is a risk of increased surface dose. Further special attention needs to be given with respect to surface dose calculation accuracy, thus measurements for dose validation are especially important.

During this work the dose build-up region of protons at the surface was investigated in-vitro by using several dosimetric devices, such as radiochromic films and ionization chambers. The dosimeters were positioned on the surface and behind several millimeters of water equivalent plates and irradiated using protons with varying proton energies and dose levels. Furthermore the effect of additional material in the beam path was investigated.

In more detail, the measurements were performed with radiochromic EBT3 films (Ashland, Bridgewater, NJ, USA), the Advanced Markus chamber and the ROOS electron chamber, both from PTW (Freiburg, Germany). The films were scanned before and after irradiation with an Expression 11000XL graphic scanner from Seiko Epson Corporation (Nagano, Japan) and calibrated in reference conditions (i.e. 8 cm × 8 cm field size in 2 cm water equivalent depth). The range shifter (RS) made of 3 cm thick polymethylmethacrylate (PMMA) was put into the beam path to shift the Bragg peak towards the surface. 97.4 MeV, 179.2 MeV and 195.2 MeV protons, with and without RS, were used to apply doses of 0.5 Gy, 1 Gy and 2 Gy in the target region and for two different beam angles, namely 0 and 20 degree. EBT3 films were composed into stacks of 1 up to 8 films in order to characterize the superficial build-up region up to 2 mm. The stacks were fixed on the surface of the RW3 water equivalent plates (PTW, Freiburg, Germany) which were positioned in the slab phantom holder while the Markus chamber was mounted on the foremost RW3 plate behind the film stack (from beam's eye view). Film results were compared to the Markus chamber values and Monte Carlo dose simulations using Gate (v8.0) /Geant4.10.03.p1. For relative analysis the dose was normalized to the entrance dose measured with the Markus chamber.

The film and Markus chamber measurements at the surface agreed within 1.5 % when irradiating at a dose level of 2 Gy and applying calibration curve and correction factors. When using a range shifter, the surface to nozzle distance is reduced as much as possible in order to decrease the spot size. The influence on the dose of the scattering and spot widening due to the range shifter was found to be up to 8 %. Furthermore, the range reduction by the range shifter was observed to work well and has no influence on the film doses, since the scaled depth-dose curves at 179.2 MeV without range shifter and 195.2 MeV with range shifter showed good agreement for film and Markus chamber results. In order to determine if the shape of the build-up at any arbitrary energy can be predicted, a simple model, based on the performed measurements at different energies, was established. It allows the approximate prediction of the depth-dose curve shape within the first 2 mm of the build-up at clinically used energies for a desired dose level of 2 Gy, with a deviation of lower than 1 %. Regarding the 20° tilted surface, the film and Markus chamber measurements revealed a lower dose of approximately 8 % compared to the perpendicular surface. The tilted films showed a severe dose loss of up to 30 % at their right half, which is supposed to be caused by field inhomogeneities due to a too tight irradiation field for this inclination. Monte Carlo simulations were consulted for comparison.

The second task of this work was the creation of treatment plans for large extremity sarcomas, which can only be treated using two or more isocenters, namely two or more fields need to be matched together. Sarcomas are always located close to the surface, so the skin dose is one of the major concerns for these patients, especially in the overlapping region of the fields. Clinically acceptable treatment plans were created using the treatment planning system RayStation v6.99 and evaluated with respect to potential patient movement and positioning uncertainties. The robustness analysis was performed by shifting the separate parts of the delineated tumor in opposite directions by about 5 mm each. The results were evaluated with respect to target coverage by means of  $D_{50\%}$ ,  $D_{98\%}$  and  $D_{2\%}$ . The dose to the skin was evaluated by comparing the nominal and the disturbed scenarios by means of  $V_{60\text{Gy(RBE)}}$ ,  $D_{98\%}$  and  $D_{2\%}$ , whereby for example the  $V_{60\text{Gy(RBE)}}$  should not exceed  $4\text{cm}^3$ . The robust analysis revealed partially severe target coverage issues, especially for the largest PTV with about 4.2 liters, which was planned with three irradiation fields. As expected, for together shifted PTV parts, the dose accumulated in the matching area, whereas the superior and inferior PTV edges received less dose. The nominal plan with the most homogeneous dose distribution –  $D_{98\%}=98\%$  for a volume of 0.4 liters – turned out to be also the most robust plan in case of the disturbed scenarios. However, owing to the largest percentage skin amount of 16.6 %, the skin dose exceeded its clinical goal by 80 % in the nominal case and even more than 400 % in case of the together shifter PTV parts. Regarding two other patients with target volumes of 1.6 liters and 2.2 liters, the skin dose objective was fulfilled in the nominal plans as well as in the perturbed scenarios. However, the PTV coverage was critically low in all plans. Dose-volume histograms and line doses verified these observations.

Concluding, the surface dose measurements revealed that the range shifter has no significant influence on the build-up shape and on film or ionization chamber dose mea-

surements at the surface. Furthermore, a simple model is able to predict the approximate shape of the build-up within 2 mm for energies between 60 MeV and 250 MeV. A more human-like geometry, like tilted or curved surfaces, might lead to serious dose deviations. Though the origin of the large dose deviation that was observed over the film length was partially traced back to a too small field size, an effect needs to be examined in more detail.

Regarding the creation of treatment plans for extremity sarcomas and the investigation of plan robustness, an acceptable CTV coverage was achieved in all nominal cases. Skin sparing was difficult, since almost all of the sarcomas had a skin percentage of 9 % or more. In the perturbed cases problems concerning target coverage, appearance of high dose areas and OAR sparing occurred. The apart shifted scenarios caused higher dose inhomogeneities than the cases where the isocenters were shifted together. The patient with the largest longitudinal tumor extension, planned with three irradiation fields, showed in the shifted cases severe under- and overdosage over the whole PTV and beyond its superior and inferior borders. In general, the presence of bones within the PTV seemed to significantly disturb homogeneous dose deposition and target coverage. Plan robustness against position uncertainties does obviously not exclusively depend on the size of the planned overlapping region, but also on the dose delivered to the target and the skin. Furthermore, the application of more than two irradiation fields is – if not absolutely required – not recommendable, since the additional overlapping region further impairs the robustness.



# Contents

<b>1</b>	<b>Introduction</b>	<b>1</b>
1.1	History of radiotherapy and general aspects . . . . .	1
1.2	Physical and biological properties . . . . .	3
1.2.1	Interaction of photons with matter . . . . .	3
1.2.2	Interaction of charged particles with matter . . . . .	5
1.3	Dosimetric aspects . . . . .	9
1.3.1	Dose units . . . . .	9
1.3.2	Clinical dosimetry . . . . .	11
1.3.3	Dose calculation . . . . .	12
1.4	Treatment workflow . . . . .	13
1.4.1	Imaging and patient positioning . . . . .	13
1.4.2	Target delineation and treatment planning . . . . .	13
1.4.3	Treatment delivery and validation . . . . .	14
1.5	MedAustron . . . . .	15
1.6	Motivation and tasks of this thesis . . . . .	17
<b>2</b>	<b>Basics of irradiation methods, dosimetry and proton treatment planning</b>	<b>19</b>
2.1	Technical implementation of particle therapy . . . . .	19
2.2	Dosimetric devices . . . . .	21
2.2.1	Ionization chambers . . . . .	23
2.2.2	Films . . . . .	24
2.2.3	Other dosimeters . . . . .	25
2.2.4	Phantoms . . . . .	26
2.3	Proton treatment planning . . . . .	27
2.3.1	Imaging, structure definition and plan creation . . . . .	28
2.3.2	Dose calculation algorithms . . . . .	29
2.3.3	Dose optimization and evaluation . . . . .	30
2.3.4	Creation of matching fields . . . . .	31
<b>3</b>	<b>Materials and methods</b>	<b>33</b>
3.1	Radiochromic film dosimetry . . . . .	33
3.1.1	Equipment . . . . .	33
3.1.2	Measurement setup . . . . .	34
3.1.3	Film irradiation . . . . .	38
3.1.4	Film scanning and analysis . . . . .	39
3.1.5	Data analysis . . . . .	41

3.2	Treatment planning on extremity sarcoma . . . . .	41
3.2.1	Treatment plan creation . . . . .	42
3.2.2	Robust treatment plan analysis . . . . .	44
<b>4</b>	<b>Results</b>	<b>47</b>
4.1	Surface dose measurements . . . . .	47
4.1.1	Preliminary investigations . . . . .	47
4.1.2	Influence of the range shifter on film and Markus chamber doses . . . . .	48
4.1.3	Build-up characterization . . . . .	49
4.1.4	Tilted surface . . . . .	52
4.1.5	SOBP measurements . . . . .	57
4.1.6	Film and Markus chamber measurements at low dose levels . . . . .	57
4.2	Treatment planning . . . . .	59
4.2.1	Treatment plan setup . . . . .	60
4.2.2	Plan design . . . . .	60
4.2.3	Plan analysis . . . . .	62
<b>5</b>	<b>Discussion</b>	<b>73</b>
5.1	Surface dose measurements . . . . .	73
5.1.1	Preliminary investigations . . . . .	73
5.1.2	Influence of the range shifter on film and Markus chamber doses . . . . .	74
5.1.3	Build-up characterization . . . . .	74
5.1.4	Tilted surface . . . . .	75
5.1.5	SOBP measurements . . . . .	76
5.1.6	Film and Markus chamber measurements at low dose levels . . . . .	79
5.1.7	Outlook . . . . .	79
5.2	Treatment planning . . . . .	79

# List of Figures

1.1	Important physicists in history of radiotherapy . . . . .	2
1.2	Dominant regions for occurrence of photoelectric effect, Compton effect and pair production depending on the atomic number of the absorber and the energy of the incident photon . . . . .	4
1.3	Depth dose curves of different radiation types . . . . .	6
1.4	Coulomb force interaction categories of charged particles traversing matter . . . . .	7
1.5	Collision stopping power plotted over the charged particle kinetic energy . . . . .	8
1.6	Volume definition stated by the International Commission on Radiation Units and Measurements in the ICRU report 62 . . . . .	14
1.7	Model photo of the accelerator layout . . . . .	16
1.8	Positioning robot with patient table and imaging ring . . . . .	17
2.1	Principle of passive scattering and active scanning . . . . .	21
2.2	Designs of (a) a parallel-plate chamber with the sensitive volume located in the center and (b) a cylindrical chamber at the example of a Farmer Chamber . . . . .	22
2.3	Operation regions of gas filled detectors, with curves (a) and (b) representing different energies . . . . .	23
2.4	Selected ionization chambers from PTW (Freiburg, Germany) . . . . .	24
2.5	Structure of the GAFChromic EBT3 dosimetry film . . . . .	25
2.6	Designs of two types of semiconductor dosimeters: (a) Silicon diode, (b) MOSFET . . . . .	26
2.7	RW3 water-equivalent slab phantom from PTW (Freiburg, Germany) . . . . .	27
3.1	Measurement setup with part of the RW3 phantom, Advanced Markus chamber and films from a bird's eye view . . . . .	37
3.2	Measurement setup: (a) with RW3 phantom (gray), delineation of the irradiation field (orange) and films (petrol) from beam's eye view; (b) for irradiation: nozzle (dark gray), RW3 phantom (gray) and films (orange) straight and tilted by 20° . . . . .	37
3.3	Delineation example (P5) with superior PTV part (green), inferior PTV part (blue), intersection part, and skin treatment area (from right PTV edges until red delineation) . . . . .	44
4.1	Comparison of original and corrected film doses for 195.2 MeV with RS, combined with Markus chamber results . . . . .	48
4.2	Comparison of 62.4 MeV, acquired with RS, and 97.4 MeV, regarding film and Markus chamber results . . . . .	49

4.3	Comparison of 179.2 MeV (nominal) and 179.2 MeV acquired by RS . . .	50
4.4	Plateau depth (red) in weighted logarithmic fit (blue line) of film and Markus chamber results (black points) for 62.4 MeV (97.4 MeV with RS) and 97.4 MeV (upper row), and 179.2 MeV acquired nominally and from 195.2 MeV with RS (lower row) . . . . .	51
4.5	Build-up for different energies . . . . .	52
4.6	Build-up model: first part from 0 to 360 $\mu\text{m}$ . . . . .	53
4.7	Build-up model: second part from 360 to 1800 $\mu\text{m}$ , fit acquired from measurements at the displayed energies . . . . .	53
4.8	Comparison of Markus chamber results from measurements on straight and tilted surface at 62.4 MeV (RS) . . . . .	54
4.9	Example of tilted film . . . . .	55
4.10	Dose distribution over film length in case of tilted films . . . . .	56
4.11	Comparison of film and Markus chamber measurements on straight and tilted surfaces at 62.4 MeV . . . . .	56
4.12	Comparison of SOBP measurements on straight and tilted surface with films and Markus chamber . . . . .	58
4.13	Application of model on the single energies used for the SOBP, compared to the Markus chamber results . . . . .	58
4.14	Measured Markus chamber results for a dose level of 1 Gy at different energies . . . . .	59
4.15	Schematic illustration of matching technique . . . . .	60
4.16	Dose difference map of nominal and RA- case for P5 (own illustration) . .	65
4.17	Dose-volume histograms of CTV, femur and 2 mm skin treatment area for P2 . . . . .	65
4.18	Line doses of nominal and RA cases for P2 . . . . .	66
4.19	Dose distribution in nominal and RA plans of P2 . . . . .	66
4.20	DVH for CTV, humerus and skin treatment area for nominal and RA cases of P3 . . . . .	67
4.21	Line doses of nominal and RA cases for P3 . . . . .	68
4.22	Dose distribution in nominal and RA plans of P3 . . . . .	68
4.23	Schematic illustration of PTV sections for P4 . . . . .	69
4.24	Dose distribution in nominal plan of P4 . . . . .	69
4.25	Dose distributions of cases a, b, c and d of the robust analysis for P4 . . .	70
4.26	DVH of the femur of P4 for nominal and RA cases . . . . .	71
4.27	Line doses of P4 for nominal and RA cases . . . . .	71
5.1	Comparison of simulation and film measurements at a straight surface . .	77
5.2	Comparison of simulation and film measurements at a 20° tilted surface .	77
5.3	Result of Monte Carlo simulation on 4 cm $\times$ 4 cm field for different angles	78
5.4	Result of Monte Carlo simulation on 7 cm $\times$ 7 cm field for different angles	78
A.1	Dose-volume histogram of P4: nominal case . . . . .	89
A.2	Dose-volume histogram of P4: comparisons of nominal and perturbed cases regarding the PTV . . . . .	89

A.3	Dose-volume histogram of P4: comparisons of nominal and perturbed cases regarding the femur . . . . .	90
A.4	Dose-volume histogram of P4: comparisons of nominal and perturbed cases regarding the 2 mm skin treatment area . . . . .	90
A.5	Calibration certificate of Advanced Markus chamber . . . . .	91
A.6	continued . . . . .	92
A.7	Calibration certificate of Roos chamber . . . . .	93
A.8	continued . . . . .	94

## List of Tables

2.1	Selected energies with corresponding ranges of protons at MedAustron . . . . .	20
3.1	Ionization chamber measurements . . . . .	35
3.2	Reference measurements . . . . .	36
3.3	Film measurements . . . . .	38
3.4	Details for film measurements at constant energies . . . . .	39
3.5	Sarcoma and planning dimensions and volumes for patients P1 to P5 (own naming) . . . . .	42
3.6	Clinical goals . . . . .	43
3.7	Objectives . . . . .	43
4.1	Plan details . . . . .	61
4.2	Dose statistics: dose values exceeding the acceptable tolerance for the CTV . . . . .	63



# List of Abbreviations

<b>CT</b>	Computed tomography
<b>CTV</b>	Clinical target volume
<b>DVH</b>	Dose-volume histogram
<b>EL</b>	Energy layer
<b>GTV</b>	Gross tumor volume
<b>IC</b>	Ionization chamber
<b>ICRU</b>	International Commission on Radiation Units and Measurements
<b>IM</b>	Internal margin
<b>ISD</b>	Isocenter-source distance
<b>ITV</b>	Internal Target Volume
<b>LET</b>	Linear energy transfer
<b>LINAC</b>	Linear accelerator
<b>MC</b>	Monte Carlo
<b>MOSFET</b>	Metal-oxide-semiconductor field-effect transistor
<b>MRI</b>	Magnetic resonance imaging
<b>NP</b>	Number of particles
<b>OAR</b>	Organ at risk
<b>OD</b>	Optical density
<b>PB</b>	Pencil beam
<b>PRV</b>	Planning organ at risk volume
<b>PTV</b>	Planning target volume
<b>QA</b>	Quality assurance
<b>RA</b>	Robust analysis

<b>RBE</b>	Relative biological effectiveness
<b>ROI</b>	Region of interest
<b>RS</b>	Range shifter
<b>RT</b>	Radiation therapy
<b>SFUD</b>	Single-field uniform dose
<b>SM</b>	Setup margin
<b>SOBP</b>	Spread-out Bragg peak
<b>SSD</b>	Source to surface distance
<b>TPS</b>	Treatment planning system
<b>TV</b>	Treated volume
<b>VOI</b>	Volume of interest
<b>WET</b>	Water equivalent thickness

# 1 Introduction

Beside surgery and chemotherapy, radiotherapy is one of the three major cancer treatment methods worldwide. In radiation therapy (RT) malignant cells are bombarded and destroyed by photons, electrons or ions (protons or carbon ions) whereas the surrounding tissue is spared as much as possible.

Radiotherapy using protons or carbon ions is currently one of the most advanced technologies in this branch of cancer treatment. The main advantage of ion beam therapy over conventional radiation types is the energy deposition, described by the Bethe-Bloch formula. In the so-called Bragg peak the major amount of the energy deposition takes place at the end of the particle range. This is the ideal basis for an optimal destruction of tumor tissue and the largest possible sparing of the neighboring organs. Thus the occurrence of common adverse reactions, for example inflammation, in organs at risk, nerves and blood vessels, depending on the effectively irradiated body parts respectively, are essentially reduced (Linz 2012, DEGRO 2015).

## 1.1 History of radiotherapy and general aspects

The following section is mainly based on the first chapter of "Ion Beam Therapy" (Linz 2012).

The research advances of Wilhelm Conrad Röntgen, Antoine-Henri Becquerel, Marie and Pierre Curie in the late 19<sup>th</sup> century made first medical treatments with ionizing radiation possible – of course not yet as effective and controllable as today. After some time it was recognized that fractionated therapy results in much less acute and long-term side effects than former high dose application. Moreover, healthy cells have a higher recovery rate after radiation exposure than cancer cells.

Ernest Rutherford was the one who discovered and differentiated alpha and beta radiation, and later named the gamma radiation, which was discovered by Paul Villard in 1900 (Gerward 1999). In the beginning of the 20<sup>th</sup> century some more sophisticated atomic models than the simple plum pudding model by Joseph John Thomson were postulated. They resulted in the nowadays common understanding of the atomic structure consisting of protons, neutrons and electrons.

In the early and middle 20<sup>th</sup> century the construction of particle accelerators, cyclotrons and synchrotrons, started. This major advance facilitated the medical therapy using electrons and neutrons. During the second half of the 20<sup>th</sup> century linear electron



Figure 1.1: Important physicists in history of radiotherapy: W. C. Röntgen, A.-H. Becquerel, Marie and Pierre Curie (top row, from left to right); Ernest Rutherford, Paul Villard (bottom row, from l.t.r.) (Time Inc., Smithsonian Institution Libraries, Association Curie Joliot-Curie, Library of Congress, Wikidata, accessed at 2018-08-03)

accelerators with X-ray or gamma (Cobalt) sources evolved, producing higher energies up to 20 MeV and thus the basis of today's photon radiotherapy.

In 1946 accelerated protons were considered to be used for medical treatment. Compared to other charged particles they showed the longest range for a given energy. The first proton treatments of humans took place at the University of California, Berkeley, in 1954. Further investigations were performed concerning the effects of ionizing radiation on living cells. In the following decades the idea of clinical treatments with protons and later on with carbon ions spread all around the world.

Nowadays three major fields of radiotherapy exist: radiotherapy with "conventional" beams (kV, MV photons and electrons), ion therapy and brachytherapy. The historical development of photon and particle therapy were already outlined and their physical and biological properties will be described later in section 1.2.

Irradiation with X-rays is usually performed using linear accelerators (LINAC). The rough principle of a linear accelerator is the following: a power generator delivers high voltage to an electron gun that produces electrons which are accelerated in a waveguide and stopped in an X-ray target. In the head of the LINAC several components are located, for example flattening filters, collimators, ionization chambers (IC) and optical distance indicators, that allow beam shaping and monitoring. If necessary, each spot can be corrected in size, position and intensity during irradiation.

For irradiation with electrons the same LINAC can be used, but it is necessary to

remove the X-ray target and the flattening filters, and to insert a scatterer, collimators and electron applicators (cf. Lynn J. Verhey 2010).

When using ions for treatment, a synchrotron or cyclotron has to be used for acceleration. Particles are produced by ion sources, pre-accelerated by a LINAC and injected into the synchrotron. They are accelerated by a radiofrequency electromagnetic field and kept in a circular orbit by strong magnets. The principle of treatment delivery in particle therapy will be explained in section 2.1. The biggest advantage of protons over photons is the controlled dose delivery in the Bragg peak region at the end of the proton range, which is driven by their energy. Consequently, the damage to surrounding healthy or radiation sensitive tissue can be dramatically reduced. Heavier ions like helium, oxygen or carbon ions could have advantages like higher precision due to less scattering and increased biological effectiveness, but their clinical advantage has not been demonstrated yet. Anyhow, carbon ion therapy is an up-and-coming treatment method and is already successfully in use at several facilities.

In brachytherapy a different approach is used. Small sealed radiation sources, mostly gamma emitters, are placed directly on or inside the tumor region. In most cases a small surgical operation under local or full anaesthesia is required. One possibility is the permanent implantation of so-called “seeds”. They emit radiation for several months and stay in the body for that time. Another possibility is the afterloading method. One or more applicators are temporally implanted and fixated in the respective body part. They are intended to stay in the body during the whole treatment period. During every treatment fraction a radiation source is automatically put in by a specific afterloading device. This kind of treatment takes a few minutes per fraction, and is executed once a day for a few weeks, or sometimes also every few hours per day.

## 1.2 Physical and biological properties

The following section is based on the books by Linz (Linz 2012) and Podgorsak (Podgoršak 2010), the IAEA handbook (Dance et al. 2014) and online articles provided by the Johannes Gutenberg University Mainz (Wagner 2006), an engineer at CERN (Meroli s.a.) and the RÖMPP chemical encyclopedia provided by the Georg Thieme Verlag (Wesener and Günther s.a.).

### 1.2.1 Interaction of photons with matter

As already explained in section 1.1, for the first radiation treatments X-rays, i.e. photons, were used. In matter they show a short build-up, then deliver almost their whole energy along a certain range while slowly falling off (see Fig. 1.3). The three most important interaction processes of photons with matter are the Compton effect, the photoelectric effect and pair production (see Fig. 1.2), but there are other effects like Thomson scattering, Rayleigh scattering and photonuclear reaction, which are usually neglected in radiation therapy and are listed for the sake of completeness. The attenuation of an incident photon beam is not a degradation in energy, but a degradation in intensity. It can be described as follows:

$$I(x) = I_0 e^{-\mu x} \quad (1.1)$$

where  $I_0$  is the incident beam intensity,  $\mu$  is the linear attenuation coefficient and  $x$  is the path length in matter.

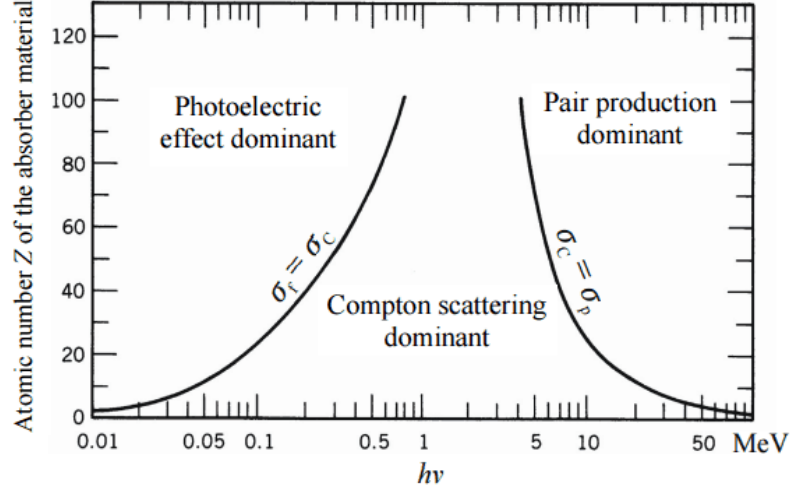


Figure 1.2: Dominant regions for occurrence of photoelectric effect, Compton effect and pair production depending on the atomic number of the absorber and the energy of the incident photon (www.nuclear-power.net s.a., accessed at 2018-08-05)

### Photoelectric effect

The photoelectric effect is predominant at low photon energies ( $E$ ) and in absorbers with high atomic number  $Z$ . An incoming photon is absorbed by an atomic electron with an initial energy  $E_{kin}$ . After the energy  $E_{h\nu}$ , which is gained through the absorption process, is added, the energy of the electron exceeds the binding energy  $E_B$ , as pointed out in Formula 1.2. Consequently, the electron leaves the shell which causes an ionization of the atom.

$$E_{h\nu} + E_{kin} > E_B \quad (1.2)$$

The resulting energy of the electron is now the difference of the total energy after photon absorption and the binding energy. It might be high enough to cause further ionizations by collisions, called secondary ionizations. If the hole in the electron shell is filled by an electron of a higher shell, the remaining energy can be released by either characteristic X-rays or passed to an electron in an outer shell, which is then called Auger electron and leaves the atom. The probability of the photo effect depends on  $E^{-3}$  and  $Z^n$  with  $n$  between 3 and 5, depending on the atomic number of the absorber.

### **Thomson scattering (elastic scattering)**

It describes the scattering process of a low energy photon on a loosely bound electron of one of the outermost electron shells. The photon causes the electron to oscillate, but leaves the atom without transmission of energy.

### **Compton effect (inelastic scattering)**

The Compton effect is the most dominant interaction mechanism in tissue at medium photon energies. An incoming photon collides with an atomic electron and knocks it out of the energy shell. The now less energetic photon is deflected. Since the energy of the interacting electron is very low compared to the photon energy, it is considered as free. Hence the Compton effect is independent of the atomic number and the occurrence probability decreases with increasing photon energy.

### **Rayleigh scattering**

A photon interacts with the whole atom and is deflected without any influence on the atom itself. Rayleigh scattering occurs only at low energies. The higher the energy, the less is the deflection of the photon.

### **Pair production**

At very high energies a photon interacts with an electron or a nucleus resulting in the production of a positron-electron pair. The prerequisite is a photon energy of at least 1.022 MeV, i.e. twice the binding energy of a positron or an electron. The probability of pair production depends on the photon energy and approximately the square of the atomic number,  $Z^2$ .

### **Photonuclear reaction**

As the name indicates, a photon interacts directly with the nucleus. The photon is absorbed and most possibly a photoneutron is emitted.

## **1.2.2 Interaction of charged particles with matter**

Particle radiation consisting of electrons, alpha particles or accelerated ions is called directly ionizing. They show different dose delivery on their path through matter when comparing to X-rays, as it can be seen in Figure 1.3. While the electron dose falls off shortly after its entrance, the proton dose slightly increases with increasing depth until it segues into a sharp maximum, the Bragg peak, followed by a steep fall-off. In contrast, carbon ions show an unfavorable tailing at the fall-off, coming from nuclear fragmentation, as described later in this section.

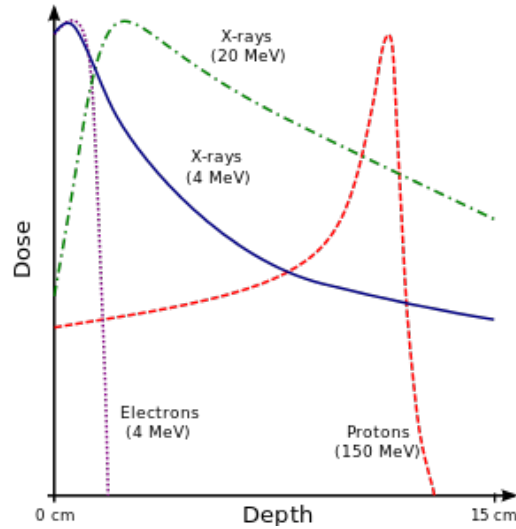


Figure 1.3: Depth dose curves of different radiation types (Creative Commons 2010)

Charged particle interaction consists mainly of Coulomb interaction with the traversed matter. It results in an energy loss of the charged particle that can be divided into collision loss by interaction of a charged particle with orbital electrons of the absorbing matter, and radiation loss by interaction with atomic nuclei of the absorbing matter. The energy loss is described by the stopping power and can also be separated into collision stopping power and radiation stopping power.

Depending on the distance  $b$  of the charged particle to the nucleus of the absorber atom and the atomic radius  $a$  of the absorber atom the interaction processes can be divided into three categories (see Fig. 1.4):

- for  $b \ll a$ : Coulomb force interaction of the charged particle with the external nuclear field of the absorber atom which results in elastic or inelastic scattering; the latter produces the so called bremsstrahlung
- for  $b \approx a$ : hard collision, i.e. Coulomb force interaction of the charged particle with an orbital electron of the absorber atom; this leads to a high energy transfer to the electron which leaves the atom as delta ray; there is only a low possibility of occurrence of these hard collisions
- for  $b \gg a$ : soft collision, i.e. Coulomb force interaction of the charged particle with an orbital electron of the absorber atom; this leads to a small energy transfer to the electron which might be ejected; the possibility of occurrence of soft collisions is very high

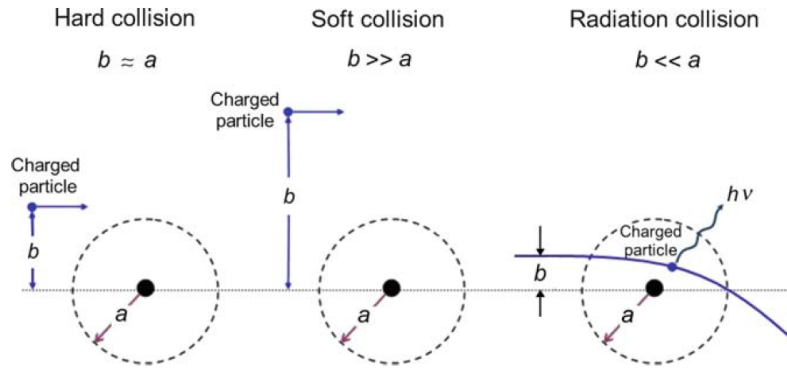


Figure 1.4: Coulomb force interaction categories of charged particles traversing matter (Podgoršak 2010)

### LET, stopping power and RBE

Coulomb interactions cause excitation and ionization of atoms along the path of the charged particle. This implies an energy transfer of the particle per unit path length, called LET. The LET equals the stopping power if all secondary electron energies are included. The collision stopping power of heavy charged particles in matter can be described by the Bethe-Bloch formula, originally formulated by Hans Albrecht Bethe and Felix Bloch, including corrections for low kinetic energies and polarization or density effect by Ugo Fano:

$$S_{col} = 4\pi \frac{N_A}{A} \left( \frac{e^2}{4\pi\epsilon_0} \right)^2 \frac{z^2}{m_e c^2 \beta^2} Z \left\{ \ln \frac{2m_e c^2}{I} + \ln \frac{\beta^2}{1 - \beta^2} - \beta^2 - \frac{C}{Z} - \delta \right\} \quad (1.3)$$

where

$N_A$	...	Avogadro constant	$\beta$	...	$\beta = \frac{v}{c}$
$A$	...	atomic mass number of absorber	$v$	...	particle velocity
$e$	...	elementary charge	$Z$	...	atomic number of absorber
$\epsilon_0$	...	vacuum permittivity	$I$	...	mean ionization potential of absorber
$z$	...	charge of particle in units of $e$	$C$	...	shell correction
$m_e$	...	electron rest mass	$\delta$	...	density correction
$c$	...	speed of light			

The corresponding stopping power curve is shown in Figure 1.5. It shows a steep and almost linear increase in the low energy region until a maximum at 250I. During the intermediate energy region the stopping power decreases steeply. At a minimum at approximately  $2.5M_0c^2$  the intermediate energy region segues into the relativistic energy region with another increase of the stopping power. The higher the atomic number of the used particle, the higher is the energy loss due to the stopping in the absorbing

material. The equation shall apply for alpha particles and heavier particles, but not for the lighter electrons or positrons. In that case, the particles become indistinguishable, the assumption of a high particle mass is not applicable any more and energy loss due to bremsstrahlung has to be considered.

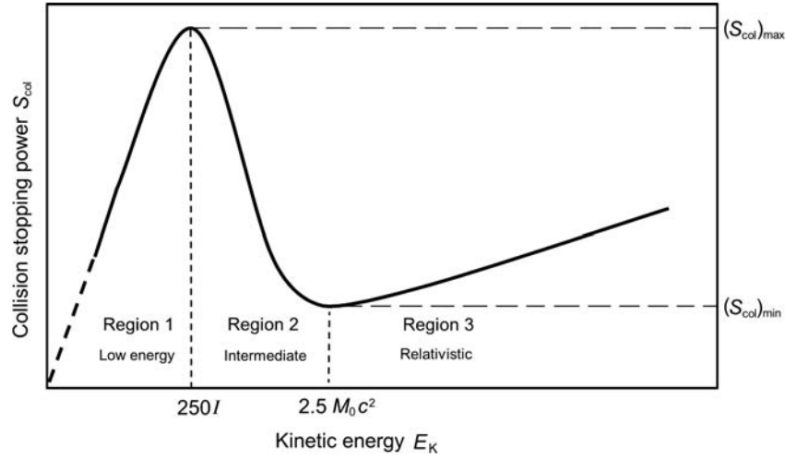


Figure 1.5: Collision stopping power plotted over the charged particle kinetic energy (Podgoršak 2010)

Electrons are also used in radiation therapy, especially for superficial tumors, but they show strong lateral scattering. This causes a severe energy loss with increasing penetration depth. The lateral scattering is heavily reduced for protons and other ions due to their higher mass.

An important term for discrimination of radiation types and regarding their application for medical purposes is the relative biological effectiveness (RBE). It describes the biological effectiveness of an accelerated ion compared to the same physical dose of a reference radiation, e.g. 250 kV X-rays or  $^{60}\text{Co}$  gamma rays:

$$RBE_{\alpha_i} = \frac{\alpha_i}{\alpha_{x\text{-ray}}} \quad (1.4)$$

where  $\alpha_i$  and  $\alpha_{x\text{-ray}}$  are the slopes of dose response curves for an investigated,  $i$ , and a standard radiation, here X-rays (cf. Paganetti et al. 1997).

For protons the RBE is assumed to be 1.1 in all clinical applications, which means that the biological dose is a factor 1.1 times the physical dose. Anyhow, the constant RBE of protons is currently a topic of intensive discussions and might be revised in the upcoming years. For heavier ions the RBE increases with increasing atomic number  $Z$  and increasing LET, but after reaching a LET of approximately  $200 \text{ keV}/\mu\text{m}$  it decreases due to a so-called energy overkill. The RBE further depends on the target material and the particle characteristics.

Heavier ions than protons or carbon ions show less scattering and therefore higher precision due to their higher mass. After nuclear collisions they often decay into smaller and lighter fragments which in turn impair the precision. Because of their high entrance LET, the fragmentation tails and high production costs, ions with atomic numbers  $Z$  higher than 6 will probably never be used clinically.

## 1.3 Dosimetric aspects

The term “dose“ is used to describe the effect of radiation on matter. It depends on activity, distance to the radiation source, energy, type of radiation and the physical characteristics of the absorbing material. The dose rate is defined as the dose per time unit.

The information in this section is based on ”Strahlungsmessung und Dosimetrie“ (Krieger 2011, chapter 9) and the course documents by Lechner 2018 and Fuchs 2018.

### 1.3.1 Dose units

There are different dose units that have to be distinguished. A rough differentiation can be made between physical dose units and body dose units. They can be further divided as follows.

#### Physical dose units

- The exposure is defined as the electrical charge per air mass that is produced by ionizing radiation, as it can be seen in Formula 1.5. The former unit was Röntgen (R), the actual SI unit is Coulomb per kilogram (C/kg).

$$J = \frac{dQ}{dm_a} \quad (1.5)$$

with  $dQ$  the electrical charge and  $dm_a$  the mass of the irradiated air.

- The absorbed dose is the medium absorbed energy of incident radiation per mass unit (see Formula 1.6). It depends on the absorbing material. The former unit was rad, nowadays Gray (Gy) is used, which is equal to J/kg.

$$D = \frac{dE_{abs}}{dm} \quad (1.6)$$

with  $dE_{abs}$  the local absorbed energy and  $dm$  the mass of the irradiated volume element.

- Kerma is the abbreviation for the Kinetic Energy Released per unit Mass (see Formula 1.7). It defines the transferred energy to secondary particles by the incident radiation per unit mass. The Kerma is depending on the absorbing material. It is measured in Gy.

$$K = \frac{dE_{trans}}{dm} \quad (1.7)$$

with  $dE_{trans}$  the transferred kinetic energy and  $dm$  the mass of the irradiated volume element.

- The equivalent dose is defined as the product of the absorbed dose and a quality factor (see Formula 1.8). This weighting factor depends on the linear energy transfer (LET) and is therefore different for different radiation types. The unit of the equivalent dose is Sievert (Sv) which equals J/kg. The former unit was radiation equivalent man, shortly called rem.

$$H = Q * D_{st} \quad (1.8)$$

with  $Q$  the quality factor and  $D_{st}$  the absorbed dose by soft tissue.

The equivalent dose forms the basis for local dose and personal dose. The local dose is defined as the dose at a certain point in space and is used in radiation protection. The personal dose describes the radiation exposure of a person in an external radiation field.

- The LET is the energy per length that is released in a material. It does not describe the stopping of radiation, but the energy transfer by interactions via collisions. The higher the LET, the higher is the radiobiological effectiveness. The unit of the LET is keV/ $\mu$ m.

### Body dose units

Body dose units are used to assess a stochastic risk; they do not describe physical effects.

- The organ equivalent dose is defined as the product of the mean dose to an organ and a radiation weighting factor (see Formula 1.9). For X-rays, electrons, gamma- and beta radiation the factor is 1, for protons it is 2, for alpha radiation it is 20, and for neutrons between 5 and 20, depending on their energy. The organ dose is indicated in Sv.

$$H_T = w_R * D_T \quad (1.9)$$

with  $w_R$  the radiation weighting factor and  $D_T$  the mean absorbed dose of the respective body part.

- The effective dose is the sum of all organ doses multiplied by the corresponding tissue weighting factors (see Formula 1.10). Its unit is also Sv.

$$E = \sum_T w_T * H_T \quad (1.10)$$

with  $w_T$  the tissue weighting factors and  $H_T$  the organ doses.

Similar to the organ equivalent dose (if averaged over several organs in case of stochastic radiation effect), the effective dose cannot be measured directly. Both quantities are used for stochastic risk assessment and definition of personal dose limits.

### 1.3.2 Clinical dosimetry

Dosimetry in the clinical context focusses on the dosimetric assessment of therapeutic radiation sources – for example accelerators, radiation equipment for X-ray and particle irradiation, gamma and afterloading facilities –, as well as dosimetric assessment of diagnostic and therapeutic radionuclides, radiation protection and quality assurance (QA).

The detection of the absorbed dose and its distribution in the patient is a main issue that can be determined in detail by means of a patient substitute, which is called a phantom. Commonly used detection methods are ionization dosimetry – i.e. with ionization chambers –, solid state dosimetry, semiconductor dosimetry, thermoluminescence dosimetry and film dosimetry. Dosimetric information together with basic beam data, like field sizes, depth doses, dose rates, scatter factors and dose profiles at different energies, can be used for example by treatment planning systems (TPS) and are taken into account for dose calculation.

Dosimetry in radiation therapy aims to determine the dose in space and time in a clinical context or to characterize a therapeutic beam, either by experimental methods or by calculations. While dose determination implies dose validation with in-vivo dosimetry or phantom measurements and dose prediction by means of dose calculation algorithms, beam characterization includes examination of beam geometry and radiation quality. The obtained information is necessary for proper dose calculation, which is described in subsection 1.3.3. Beside these dedicated applications in clinical routine, dosimetry is the basis for implementing new techniques and new ionization chambers.

In nuclear medicine the dosimetric tasks are confined to determination of specimen activity and radiation protection responsibilities.

In diagnostic radiology dosimetry is required for radiation quality assurance, determination of X-ray dose rate and the assessment of imaging doses associated with diagnostic imaging. Anatomic imaging is also gaining more and more importance in radiotherapy for positioning verification and response assessment while the additional dose burden cannot be neglected.

### 1.3.3 Dose calculation

A treatment planning process consists of several steps including diagnosis, imaging, prescription, design of dose distribution and dose calculation, dose delivery and treatment response assessment. Dose calculation is thereby a very crucial and also critical step. Its purpose is to predict the dose for the treated target volume as well as for the surrounding tissue.

Looking at historical and present approaches in dose calculation, it is apparent that the dose calculation process has improved significantly. In earlier times dose was assessed by means of drawings of anatomy and beam geometry according to the doctor's or physicist's experience. In the 1950ies the calculation was simplified by the emergence of calculation machines. Later the target and OAR definition was facilitated by CT images, which also facilitated the attenuation calculation based on CT gray values representing certain tissue densities. All these technologies together allow for a three-dimensional treatment planning nowadays.

For dose calculation the following information is required:

- Machine data and all related beam characteristics
- Patient/phantom density and material composition information
- Dose calculation algorithm

Machine and beam data include parameters like machine geometry, scatter elements, physical effects, scatter products, treatment field size and energy. Patient data, i.e. geometry and density information, are assessed from the CT images. Phantom data can either be geometrically designed or also assessed from CT images. Hounsfield units from CT images have to be converted into electron density and for particle therapy into the respective material stopping power values. Together, machine data and patient data build the base for thorough and precise dose calculation.

Precision is an important aspect in dose calculation. Only a small change in the calculated dose can have a significant impact on the clinical outcome. The higher the accuracy and quality requirement on the radiation, the higher is the precision requirement on the dose calculation.

There are different types of algorithms: point dose calculation, 2D calculations and 3D calculations. The latter includes multi source models, pencil beam (PB) kernel, point kernel and Monte Carlo (MC). Dose calculation for protons is described in more detail in subsection 2.3.2.

## 1.4 Treatment workflow

A treatment process can be divided roughly in imaging, treatment planning, treatment validation and delivery. Imaging, including precise patient positioning, is the basis of the whole process, a treatment plan is needed to define the dose application to the patient, and dosimetric validation is required to check if the desired target dose obtainment was achieved. Dose calculation, as part of the planning process, was already explained in the previous subsection 1.3.3. The treatment planning process will be extensively described at the example of proton therapy in section 2.3. As established and implemented for longer in photon therapy, improvements and simplifications in proton therapy were achieved by digital imaging and computer-assisted treatment planning. Treatment delivery, however, is completely different for photons and ions.

### 1.4.1 Imaging and patient positioning

The first and very important step in a radiotherapeutic treatment is the imaging, and thereby the localization and characterization of the tumor region by computed tomography (CT), magnetic resonance tomography (MRT), positron emission tomography (PET) or its combinations. Nowadays the target volume delineation and treatment planning process builds on these high-resolution 3D imaging techniques, whereas in earlier times only planar X-rays were available.

Prior to the imaging process, the patient position has to be reproducibly defined and documented. Positioning is performed with assistance of positioning aids (masks, vacuum mattresses, arm and leg rests), a precise laser system and kV imaging or a fast cone beam CT for verification. Markers and tattooed points help reproducing the position for every treatment fraction.

The combined image data is used for tumor and organ at risk (OAR) volume definition while the CT data is used for three-dimensional treatment planning. MRI shows a better soft tissue contrast than CT, but it cannot determine the Hounsfield units, i.e. the electron density within the images, which is the basis for the calculation of the particle attenuation in tissue and therefore for accurate treatment planning.

### 1.4.2 Target delineation and treatment planning

In terms of volume definition, tumor delineation passes various steps (see Fig. 1.6). It starts with the gross tumor volume (GTV) which defines the visible tumor. The GTV including the microscopic spread (lymph nodes, perivascular, perineural) is called clinical target volume (CTV). By adding internal margins (IM) this is expanded to the internal target volume (ITV). Combined with setup margins (SM) it results in the planning target volume (PTV). The margins stand for organ motion, tumor and patient movement and inaccuracies of the beam and patient setup, as defined in the ICRU report 62 (ICRU 1999). Thus the PTV considers now the effect of all possible geometrical variations. Or-

gans which are nearby the target volume or required for peripheral dose assessment are also delineated separately. They are called organs at risk or rather planning organ at risk volume (PRV) when margins are added. The treated volume (TV) is then defined as the volume enclosed by a specific isodose, i.e.  $D_{98\%}$  resulting in the volume which receives at least 98% of the planned dose. More details can be found e.g. in ICRU 1999 and Linz 2012, chapter 29.

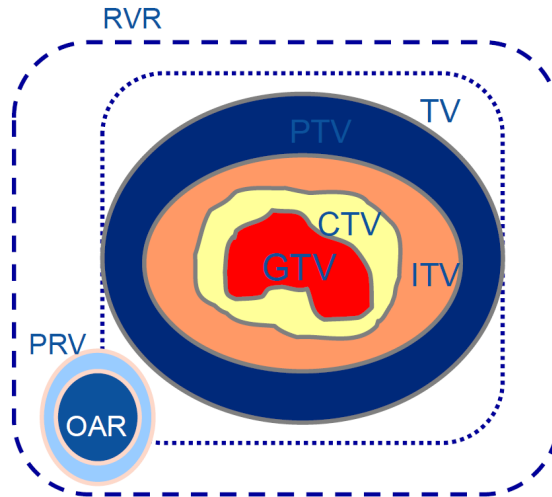


Figure 1.6: Volume definition stated by the International Commission on Radiation Units and Measurements in the ICRU report 62 (ICRU 1999)

In the treatment prescription target doses and clinical constraints for the OARs are given by the medical doctor. Plan creation includes then the definition of dose application to the target by means of beam geometry specification, energy selection, spot weighting etc. in consideration of the clinical constraints. Concerning accuracy of the treatment plan, it has to be taken into account that robustness with respect to uncertainties in beam delivery, patient positioning and patient and organ movement is an important issue, especially when treating with ions.

### 1.4.3 Treatment delivery and validation

Treatment with photons can be performed by image guided radiotherapy, intensity modulated radiotherapy (IMRT) or volumetric modulated arc therapy (VMAT). Proton treatment is delivered by passive scattering or active scanning, as it is described in more detail in section 2.1.

Before each irradiation the beam parameter and settings that were defined in the treatment plan are transmitted to the program that controls the irradiation. The patient treatment position is either transferred from the dicom RT plan, or the patient is positioned by means of tattooed marks and geometric information. In both cases the

patient position is checked by in-room imaging before every fraction.

The course of photon and proton treatment is usually fractionated over some weeks to allow recovery of the normal tissue. Depending on the tumor type and location, irradiations with photons or protons are performed up to five or six days a week, perhaps even twice a day, called hyperfractionation. At each session renewed imaging is performed and registered to the last image data in order to redefine and improve patient position and setup. The initial setup includes, among other things, setting of markers, delineation of the irradiation field on the patient's body, and a further check of all technical parameters by a medical physicist.

The initial setup needs approximately 10 to 30 minutes for photon and proton treatment, but the duration can vary for different facilities. In the following fractions, the setup of the patient including daily image guidance takes only about 5 to 15 minutes for photons, and can last between some minutes and an hour for protons, depending on the delivery technique and the tumor volume.

Before applying the plan which was approved via dual control principle, independent validation of the dose needs to be performed. This can either be done by an independent dose calculation with a separate software than the TPS or by measurements. The decision how to perform the dose validation is made according to the available equipment at the respective department, the legal requirements in the country and the complexity of the treatment plan. While independent dose calculation is usually based on Monte Carlo algorithms for photons as well as for protons, measurements differ between these two modalities. For photons for example a ionization chamber matrix, like the Delta 4 phantom from Elekta is a common device, while for particle therapy, especially for carbon ions, individual solutions are used. These can for example be measurements with an array of pin point chambers or with an ion chamber matrix in a dedicated phantom.

More information about accelerators and treatment time plans can be found in Georg 2018, Nesvacil and Kirisits 2018, Wiegel 2018, Luks and Stillger s.a., St. Vincentius-Kliniken Karlsruhe 2015, Nucletron s.a. and Drägerwerk AG & Co. KGaA 2009.

## 1.5 MedAustron

MedAustron is a center for ion therapy and research in Wr. Neustadt, Austria. It was built in 2011 and started patient care at the end of 2016. It consists of a particle accelerator and three irradiation rooms for clinical treatment. The beam is further available for research experiments in a dedicated irradiation room. All rooms are shown in Figure 1.7. Particle therapy is currently performed with protons with the horizontal and vertical beam line, while carbon ions are planned for 2019.

The general treatment workflow in radiation therapy is usually independent from the irradiation technique in most aspects. Though, the highly sophisticated treatment tech-

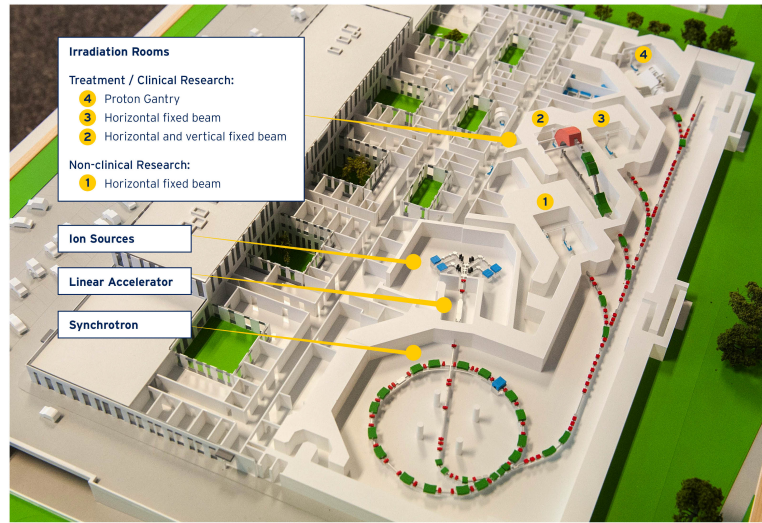


Figure 1.7: Model photo of the accelerator layout (MedAustron 2017)

niques, with protons or carbon ions, have high requirements to all the workflow steps like positioning, in-room imaging, and treatment planning to exploit their full potential. An ion therapy center like MedAustron cannot resort to standard procedures of conventional photon therapy, therefore individualized solutions need to be established. For photons a lot of research and developments were conducted yet, which partly needs to be done for protons. Ion therapy is a potentially promising branch and MedAustron is the only ion therapy facility in Austria. In order to perform academic research beside the patient treatment, the Austrian universities, especially the Medical University of Vienna and the Technical University of Vienna can use a certain amount of research beam time and the required research equipment at MedAustron for their projects.

The particle accelerator at MedAustron consists of a linear pre-accelerator and a synchrotron. It was developed with the collaboration of CERN in Switzerland. Protons and carbon ions are and will be produced by ion sources and accelerated up to 200 000 km/s. The beam is then guided by strong magnetic fields through vacuum tubes into the nozzle of the respective irradiation room.

Irradiation on a specific field is performed by the spot scanning technique. That means that magnets guide the particle beam over the field that shall be irradiated and apply the dose to single spots. The maximum field size that can be irradiated is  $20\text{ cm} \times 20\text{ cm}$  which is problematic for larger tumors. Besides the dose and beam delivery system which controls spot positioning and intensities, the nozzle contains a range shifter (RS) and different filters that can all be extended and retracted automatically and independently.

As already mentioned before, MedAustron includes four irradiation rooms. The three clinical rooms are equipped with once only a horizontal, then a horizontal and vertical beam line for protons and carbon ions and the third one with a gantry, which can move around the patient and will only be used for protons. Protons are clinically used with energies from 62.4 to 252.7 MeV, carbon ions will have a range of 120 to 400 MeV which is sufficient to treat all medical indications. In the research room there is a horizontal fixed beam currently for protons with up to 252.7 MeV, which will be increased up to 833 MeV in the near future.

In each irradiation room there is a modern patient positioning system consisting of an industrial robot that is installed on the ceiling, an optical monitoring system and an imaging ring that is mounted on the patient table and can perform planar X-rays and (dual) cone-beam CTs (see Fig. 1.8). Due to the special installation of the robot arm it allows for six independent movement directions. Lasers and a tracking camera embedded in the floor assist for right patient positioning and the imaging ring is used to check the position.



Figure 1.8: Positioning robot with patient table and imaging ring (MedAustron 2017)

More information about the MedAustron ion therapy center is provided by the MedAustron homepage (MedAustron 2017).

## 1.6 Motivation and tasks of this thesis

Ion therapy is particularly suitable for patients with tumors that are located close to radiation sensitive organs like the sensitive structures in the brain, e.g. hippocampi, temporal lobes and the optical structures, and tumors close to the spinal cord, heart, liver and lung. Especially children and adolescents benefit from this kind of radiation therapy, because they are still in the growing and development stadium and therefore the more radiation sensitive tissue can be potentially better protected than with conventional

radiotherapy.

Another organ that potentially benefits from ion therapy is the skin. Irradiation of near-surface tumors with photons and their behavior when impinging on human (or human-like) tissue are well investigated (Bilge et al. 2008, Chiu-Tsao and Chan 2009, Chung et al. 2005, Devic et al. 2006, Nakano et al. 2012, Roberson et al. 2008). Skin protection and dose application in this shallow depth are an important issue for proton treatment as well, but not well investigated. Therefore, further research is still required. In particular, the dose build-up at the outermost surface of the skin, which happens in the micrometer to millimeter range, is highly relevant with respect to the skin side effects, especially when applying doses higher than 60 Gy (RBE). The applied dose can be measured by various active and passive detectors, for example radiochromic films, thermoluminescence dosimeters (TLD) and ionization chambers, as extensively described in section 2.2. When aiming for in-vivo dosimetry passive detectors are gaining importance. The lowest energies available at synchrotron and cyclotron based facilities usually limit the minimum particle range to a few centimeters. This implies the need of using a range shifter out of polymethylmethacrylate (PMMA) to treat superficial tumors.

Also in in-silico studies the effects of the irradiation on near-surface tumors can be examined. By means of CT images imported in a treatment planning system the locations of the tumor and other structures can be determined. Treatment plans can be created and optimized in different ways to ensure best target coverage and OAR sparing as possible. Nevertheless, due to possible inaccuracies especially in the surface region when using a range shifter, measurements are essential to verify the prediction of dose distribution and skin dose.

One purpose of this work was to investigate the dose build-up on the surface during irradiation with protons in more detail. Therefore, experiments using several dose measurement devices in different superficial depths and at different angles were performed using various energies and dose levels. Furthermore it was investigated if and how the use of an external element in the beam path, like a range shifter, influences the dose build-up. Another purpose was to evaluate if radiochromic films are suitable for surface dosimetry.

In order to investigate surface dose application in a clinical example, clinical treatment plans were created for five patients with large superficial extremity sarcoma on arms or legs – which need two or more isocenters resulting in field patching for volume coverage – and a robustness analysis was performed on every plan. During this analysis the sensitivity of each treatment plan to patient movement or inexact positioning was investigated. The overlapping regions were observed when simulating the case of significant patient movement and inexact positioning. The resulting dose distribution in target and skin region was evaluated by means of various dose-volume specifications.

## 2 Basics of irradiation methods, dosimetry and proton treatment planning

### 2.1 Technical implementation of particle therapy

Tumor irradiation with protons or carbon ions can be performed by active beam scanning or by passive beam delivery. Active scanning is also known as raster scanning or pencil beam scanning. During active scanning a small beam spot is directed by strong magnets to a dedicated position and scanned over the whole treatment area that was defined in the treatment planning process (see Fig. 2.1). It allows for almost all possible dose delivery patterns and depth dose modulations. Different depths can be achieved by applying different energies; the higher the energy, the larger the range of the beam. In clinical operations, the commonly used energy range with protons is about 60 to 250 MeV, corresponding to ranges from 3 to 38 cm in water. As example, a detailed list of energies and corresponding ranges of protons at MedAustron is shown in Table 2.1. Pencil beam scanning is always based on intensity modulated particle therapy (IMPT), either by single-field uniform dose (SFUD) with minimized in-field modulation (cf. Lomax 2016) or by highly modulated proton therapy. In both cases, the individual spot weights are inversely optimized to achieve the desired dose distribution. The intensity, i.e. the spot weight, at spot position of the irradiated volume is defined by the number of particles (NP) per spot. Besides beam intensity, the speed of dose delivery and therefore the treatment time depends on the beam extraction system, the transport efficiency and the energy modulation technique. In order to achieve a homogeneous dose distribution, certain energy layer (EL) and spot spacing is required. In order to achieve a clinically acceptable homogeneous dose over the full tumor area, an EL spacing below 3.3 MeV and spot spacing around 5 mm is recommended, based on experience of running ion beam centers and internal guidelines at MedAustron. However, these values strongly depend on the individual tumor characteristics, including tumor type and position, and the need of external elements, like a range shifter. The larger the spacing between energy layers or spots, the higher the risk of dose inhomogeneities and insufficient target coverage but the faster the dose delivery. The lateral penumbra around the target depends on the divergence of the pencil beam spots, the beam-scanning pattern and the target margins that are set. Special care has to be taken in terms of target and organ motion, which can lead to under- or overdosage in and around the target. Advantages of the active scanning technique are the flexible dose delivery patterns and the independency from patient-specific calibrations and devices in the beam line. On the other hand, it is expensive, not very robust, it needs a high accuracy in patient positioning and is prone to errors due to organ movements (cf. Schwarz 2011).

Table 2.1: Selected energies with corresponding ranges of protons at MedAustron (own compilation)

Energy [MeV/n]	Range [mm]	Energy [MeV/n]	Range [mm]
62.4	30	179.2	210
67.5	35	188.7	230
72.4	40	198.0	250
81.3	50	207.0	270
97.4	70	211.4	280
104.7	80	215.7	290
111.6	90	224.2	310
124.7	110	232.6	330
136.8	130	240.8	350
148.2	150	244.8	360
153.6	160	248.8	370
159.0	170	252.7	380
169.3	190		

In contrast to active scanning, passive delivery is performed by a scattered beam that traverses a series of mechanical devices for appropriate target irradiation (see Fig. 2.1). The system consists usually of two scatterers that widen the beam, a range modulator, a collimator and a compensator. As range modulator, a ridge filter or a range modulator wheel, for example, is used. It consists of numerous steps of different thicknesses and is responsible for the design of the spread out Bragg peak. The collimator or multi leaf collimator maps the shape of the region to be treated (cf. Durante and Paganetti 2016). The compensator consists of a bolus for depth modulation in the patient. Additionally, some dosimetric devices can be positioned in the beam line. As all this equipment implies more material in front of the patient, the energy loss increases and therefore a higher beam intensity is needed in order to achieve a certain range in the tissue. The lateral penumbra depends on the accelerator characteristics as well as on the diffusing materials between nozzle and patient. Since passive scattering is much more robust than active scanning, organ motion and related uncertainties do not influence the dose distribution outcome that much. On the other hand, a scattered beam is more difficult to model for dose calculation because of the number of devices consisting of different materials in the beam line. Moreover, secondary particles like neutrons that result from scatter interactions of protons with the material in the beam line, which have a high biological effectiveness, can lead to an unintended dose deposition. Passive scattering can only deliver a homogeneous dose to the target from every beam direction and further not be used for IMPT. The necessity of a new bolus and collimator shape production for each target, and the still not optimal conformity in the proximal and lateral tumor parts are further disadvantages of passive scattering. Due to today's increasing number of implementations of active beam scanning, and the above mentioned disadvantages of

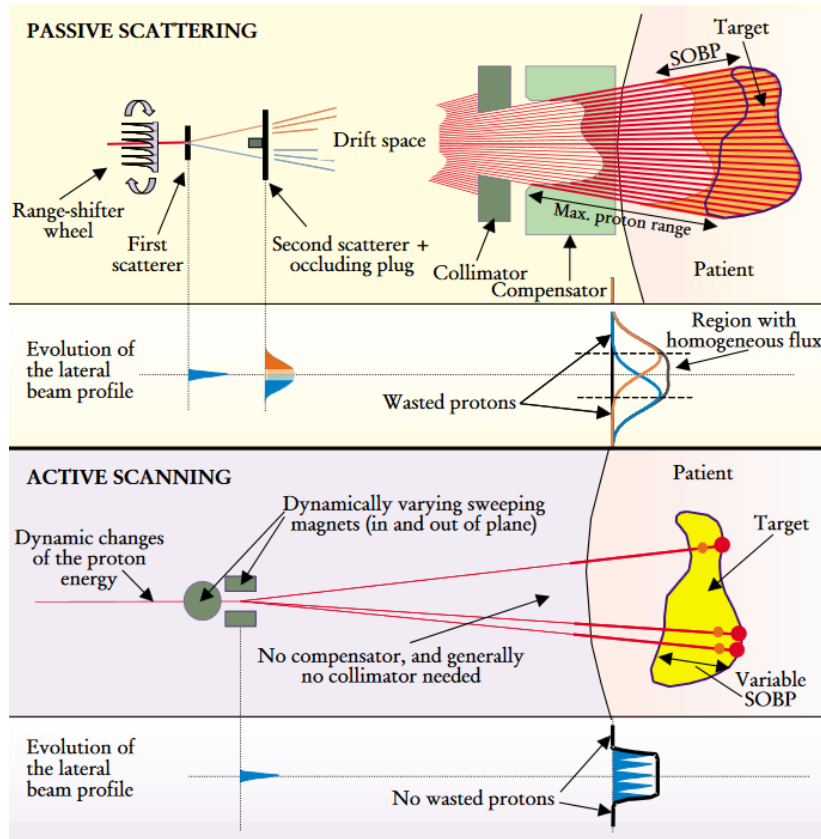


Figure 2.1: Principle of passive scattering and active scanning (Goitein et al. 2002)

passive scattering, this method is becoming outdated.

More information about active and passive beam delivery can be found e.g. in chapters 26, 30, 40 of "Ion Beam Therapy" (Linz 2012), Fujimoto et al. 2011, Schwarz 2011 and Stock and Georg 2018.

## 2.2 Dosimetric devices

There are different measurement devices for dose detection which can be separated in active and passive detectors. That means that either the dose is determined during irradiation or the final dose is read out after irradiation. Examples for active modalities are ionization chambers (IC) and metal-oxide-semiconductor field-effect transistors (MOSFET). Passive modalities are for example image plates, radiosensitive films, thermoluminescence dosimeters (TLD) and Alanin dosimeters. The active devices, the radiosensitive films and Alanin dosimeters allow for absolute dosimetry, with the Alanin dosimeters known to be so far the most accurate passive device. Common relative dosimeters are for example TLDs, but also ionization chambers and films can be used in relative dosimetry.

The information in this section is mainly based on "Strahlungsmessung und Dosimetrie" (Krieger 2011), "Radiation Oncology Physics" (Podgoršak 2005, chapter 3) and "Diagnostic Radiology Physics" (Dance et al. 2014, chapter 21).

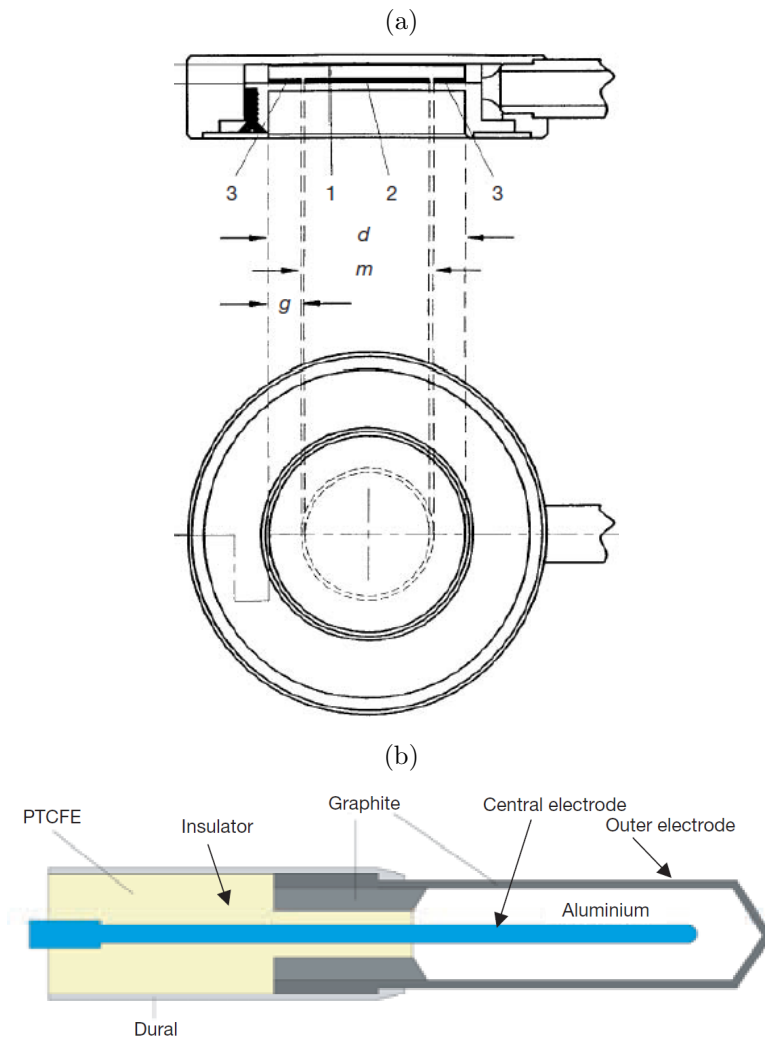


Figure 2.2: Designs of (a) a parallel-plate chamber with the sensitive volume located in the center (with 1: polarizing electrode, 2: measuring electrode, 3: guard ring, and  $d$ ,  $m$  and  $g$  the corresponding diameters and width), and (b) a cylindrical chamber at the example of a Farmer Chamber (Podgoršak 2005)

## 2.2.1 Ionization chambers

Ionization chambers can be divided in cylindrical detector chambers and plane-parallel chambers. Both consist of a gas filled chamber and two condenser plates or otherwise shaped electrodes (Fig. 2.2), which represent anode and cathode, with an applied voltage. When an ionizing particle enters the chamber it produces ion pairs which separately move to the opposite charged electrodes. This movement corresponds to a current flow which is recorded by an electrometer. To avoid recombination (in low voltage region) or secondary charge production (proportional region at high voltages), the applied voltage should always be in the saturation region (see Fig. 2.3). Each chamber needs a different voltage that has to be defined in the electrometer settings before connecting. The signal output by the electrometer is the accumulated charge, counted in Coulomb – mostly nC or pC –, and needs to be converted into dose (in Gy) in consideration of a calibration factor for the chamber and several correction factors for the room temperature and pressure.

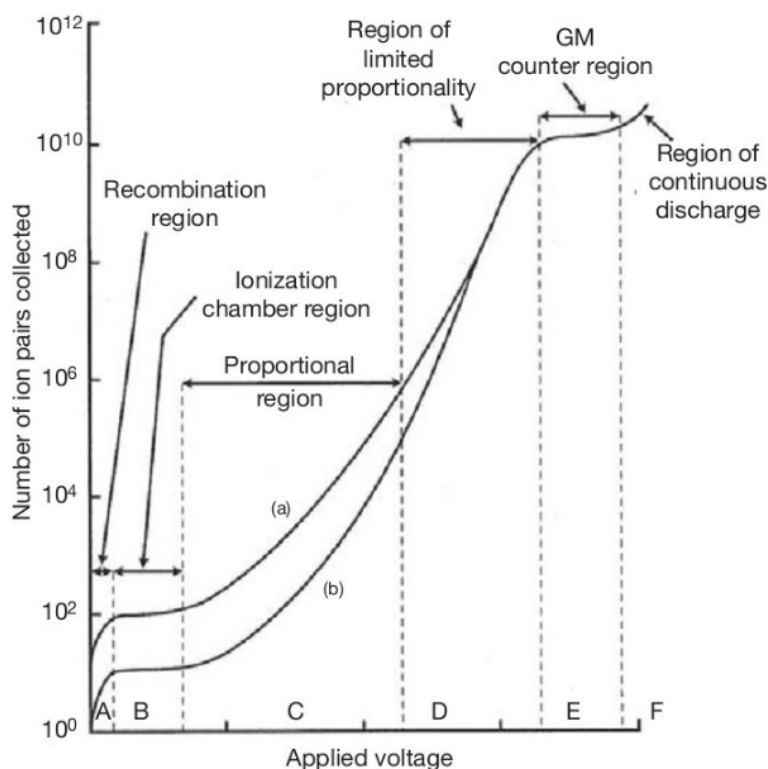


Figure 2.3: Operation regions of gas filled detectors, with curves (a) and (b) representing different energies (Podgoršak 2005, p. 103)

In radiation therapy and research, ionization chambers are basically used for daily beam performance checks, calibration of other dosimetric devices and for dosimetric measurements. For research purposes, they can be inserted in various phantoms, requir-

ing specific holders to impede shifting. There is a variety of ionization chambers with different measuring volumes available on the market. Figure 2.4 shows some types of commonly used chambers from PTW (Freiburg, Germany).



Figure 2.4: Selected ionization chambers from PTW (Freiburg, Germany): a) Farmer Chamber, b) Advanced Markus Chamber, c) Bragg Peak Chamber (PTW 2017/18)

## 2.2.2 Films

Radiosensitive films are a type of dosimeter preferably used in investigation of lateral dose distribution or transmission radiation doses. Their low thickness and customizable size allows for 2D dose determination, as well as "quasi"-3D when stacking more films on top of each other. There is a clear distinction between radiographic and radiochromic films. The first consist of an emulsion of silver halide crystals on a transparent film base. The silver grains need to absorb a couple of photons to establish a latent image. Radiographic films are very light-sensitive and not self-developing, i.e. they require a chemical process of development, fixing and washing in order to get a viewable permanent image. In contrast, radiochromic films consist of polyester bases embedding an active layer. This layer contains a dye which is originally colorless, but changes to blue by a polymerization process when irradiated. Radiochromic films should be almost insensitive to light and self-developing.

Hereafter, only radiochromic films and their usage will be further explained, based on the example of the GAFChromic EBT3 film type, since they were used in the practical part of this thesis. The EBT3 films consist of a  $28\ \mu\text{m}$  thin active layer which is sandwiched between two layers of a matte surface clear polyester base of each  $125\ \mu\text{m}$  thickness, as it is shown in Figure 2.5. The active layer is composed of the active component, a marker dye, stabilizers and others. Consequently, the film has a total physical thickness of  $278\ \mu\text{m}$ , while the water equivalent thickness (WET) of the film is  $360\ \mu\text{m}$ .

The GAFChromic films have an original size of approximately  $20\ \text{cm} \times 25\ \text{cm}$ . They can be cut into pieces of any size, though a reasonable size should not be undercut since the edges are prone to decomposition. Since films are not water resistant, a specific protection sleeve is required when using films in water, whereas for fixation on solid

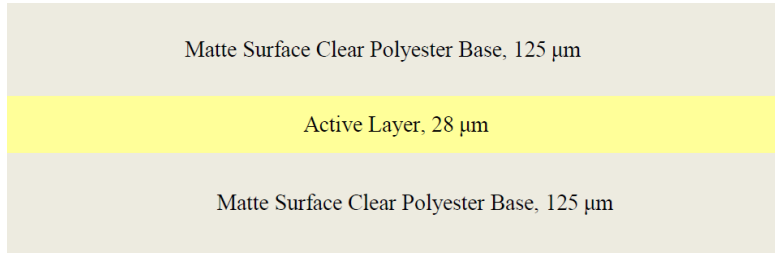


Figure 2.5: Structure of the GAFChromic EBT3 dosimetry film (Ashland s.a.)

phantoms a standard tape can be used. To avoid falsification and uncertainties, the film surface must never be touched by bare skin. After irradiation the darkening of the films intensifies in the following hours until saturation is reached. Therefore reading should be performed soonest 24 hours after irradiation (cf. Devic et al. 2016, Devic et al. 2005, Dreindl et al. 2017).

In order to determine the “stored” dose, a special flatbed scanner and a dedicated software are used to read out the pixel values of the films. The pixel values can be converted into the net optical density, which is then converted into dose by means of a calibration curve. Calibration is performed in reference conditions for every film batch prior to any other measurements. For the creation of the calibration curve the films are irradiated at several dose levels, which results in different darkenings (optical density) of the films that are subsequently plotted against the administered dose. The dependency of optical density (OD) and dose (D) can then be described for example by a 4<sup>th</sup> order polynomial fit. The complete procedure of film scanning and analysis is explained in subsection 3.1.4.

### 2.2.3 Other dosimeters

Another dosimeter type is the thermoluminescence dosimeter. It consists of crystalline materials with the ability of storing energy of ionizing radiation. Later, when stimulated by heating, this energy is emitted as light. Physically this corresponds to a recombination of electrons and holes. The emitted luminescence is proportional to the absorbed dose and can be detected by a photomultiplier tube and further processed in the reader electronics. The used crystals are either naturally occurring or artificially produced. Usually lithium fluoride (LiF) is used with different doping agents. As relative dosimeters, TLDs need to be calibrated against an absolute dosimeter, e.g. a calibrated ionization chamber (cf. Shani 2001, chapter 4). The advantages of TLDs are the large effective range, high energy independence, low fading and therefore a high storage capacity (cf. Krieger 1998). The most important disadvantage is the high WET, which impedes the study of superficial processes.

Semiconductor dosimeters can be divided into silicon diodes and MOSFETs. Silicon diodes consist of a p- and an n-doped region and a depletion region in the middle, as

Figure 2.6 shows. Radiation produces electron hole pairs in the diode which results in a current in opposite directions that can be measured. MOSFETs are similar to planar capacitors with a semiconductor instead of one electrode. As in the silicon diodes, electron hole pairs are produced during irradiation. This leads to an accumulation of positive charge carriers in the region between source and drain and disturbs the current in the n-type channel. The result is a shifted threshold voltage that is linear proportional to the absorbed dose.

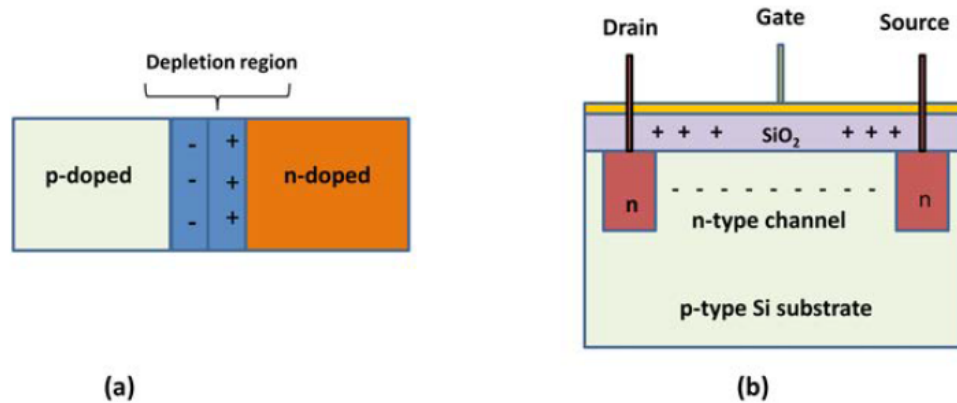


Figure 2.6: Designs of two types of semiconductor dosimeters: (a) Silicon diode, (b) MOSFET (Dance et al. 2014, p. 535)

## 2.2.4 Phantoms

Different types of phantoms are used to perform detector calibrations, investigate depth dose curves, dose rates, radiation quality, etc. The most common phantom materials are water and acrylic materials. Water is used as substitute for soft tissue, since it consists of water to a large extend and water shows a similar absorption and scattering behavior.

Due to its soft tissue equivalent properties and the flexible usage possibilities the most common phantom type used in radiotherapy is a water phantom, which is available in different sizes and designs and from different vendors. It consists of a hollow transparent solid cube, filled with water, where specific holders for ionization chambers and other dosimeters can be mounted. Exact positioning can be guaranteed by a highly accurate motoric system which moves the arm where the chambers are mounted. At the entrance window a reference chamber can be mounted since many measurements gain accuracy when the results are determined with respect to a reference chamber. Most dosimetric devices need waterproof protection caps. Depending on the radiation type and energy used, the phantom should provide sufficient space in order to prevent scattering on the walls.

The dosimetric devices described in this chapter, i.e. ionization chambers, films and

TLDs, can also be inserted or fixated for example on water-equivalent slabs. Figure 2.7 shows the RW3 slab phantom from PTW (Freiburg, Germany). The single plates are available in thicknesses of 1, 2, 5 and 10 mm and have dimensions of 30 cm × 30 cm. The phantom was designed for monitoring calibration and quality assurance measurements. Though the solid water phantom is easier to handle than the above described water-filled phantom, it is disadvantageous because the material composition and density are not exactly equivalent to water and therefore can cause inaccuracies regarding range and dose calculation. Moreover, any arbitrary depths cannot be reached due to the limited slab thickness of 1mm. In general, the water phantom is the standard phantom used for all types of ionization chambers. (PTW 2017)



Figure 2.7: RW3 water-equivalent slab phantom from PTW (Freiburg, Germany) (own research)

In order to mimic the patient geometry, anthropomorphic phantoms are used. They consist of materials with similar characteristics as human tissue. This type of phantom can be customized by the manufacturer, providing recesses for diverse dosimetric devices. Furthermore different sizes for man, woman and children, or single body parts, e.g. pelvis or head, are available. (CIRS 2013, RSD 2014)

## 2.3 Proton treatment planning

The whole treatment planning process, independent of the respective target location, consists of several steps:

- Imaging
- Target and OAR definition
- Treatment plan (TP) creation

- Dose calculation
- Optimization and evaluation
- Patient specific QA

Imaging is as first step the basis for the following treatment process. Image data are required for patient positioning as well as for treatment plan creation. After target and OAR definition and delineation, all beam configurations have to be defined in the treatment plan. This is a prerequisite for the optimization of the spot distribution within each energy layer and a subsequent reliable dose calculation and further optimization procedures. The calculation of spot positions and weights as well as the optimization and final dose calculation can be performed by different algorithms. When the plan shows good target coverage and dose homogeneity as well as OAR sparing according to the clinical prescription, it is approved by the medical doctor and transferred to the beam delivery system for quality assurance and patient irradiation.

### **2.3.1 Imaging, structure definition and plan creation**

#### **Imaging**

During imaging, CT, MRI or PET images are acquired with specific settings and a fixed patient position, the same that will be used in the later irradiation process. The CT images are imported into a treatment planning system and the respective measured values (Hounsfield units (HU) in CT images) are converted into electron density values by using a scanner specific calibration curve. Attention should be paid to artefacts, e.g. due to metal implants, which can cause severe misrepresentation of electron density due to the high density that is above the limit of the CT calibration curve and the artefacts that cause a disturbance of the gray values over a big area of the CT scan (cf. Schwarz 2011). MRI and PET images are fused to the planning CT and used for target definition and OAR delineation.

#### **Structure definition**

Target region and organs at risk are delineated by a medical doctor with support from radiation technologists. Useful delineation tools in the TPS are for example the autosegmentation function with gray level thresholding or volume thresholding, semi-automatic model-based segmentation or atlas-based segmentation. All delineated structures are defined as regions of interest (ROIs). Depending on the target location, possible organs and structures at risk are heart, brain, spinal cord, glands, liver, nerves, vessels, bones and skin. In treatment planning on superficial tumors, the skin is a very important and sensitive organ at risk. (RaySearch 2017b)

## Plan creation

In the course of treatment plan creation, several parameters are to be defined, e.g. irradiation modality, treatment technique, treatment machine, prescribed dose and number of fractions. The number of used beams depends on the prescribed target dose, the possible irradiation directions and the sensitivity of the surrounding tissue. Sometimes the target volume exceeds the possible field size. In this case more fields have to be irradiated consecutively, aiming at an ideal dose distribution over the whole target size. The planning procedure for these matching fields is explained in subsection 2.3.4. Settings for the beams include isocenter definition, beam and couch angle, gap between patient and nozzle, and the possible necessity of a range shifter, which is always used in case of superficial tumors, as already mentioned in section 1.6.

### 2.3.2 Dose calculation algorithms

In proton therapy there are two main approaches for calculating dose: Pencil beam and Monte Carlo methods. Within both concepts, many different algorithms with varying importance of parameters, like geometry or scattering, exist and continually new algorithms are developed. In the following, the basics of Pencil beam and Monte Carlo algorithms are briefly explained, including possible parameter considerations.

#### Pencil beam (PB)

The pencil beam mode is probably the most widely used method for proton dose calculation. Originally it was designed for passive beam scattering. There are a number of different pencil beam algorithms developed so far, each considering more or less parameters in beam delivery. Nevertheless, all algorithms are based on the theory, that a beam is split into an infinitesimal number of pencil beams that pass through certain field coordinates. The single doses depend on the energy loss and the scattering in the traversed material. The total dose distribution is then a superposition of all pencil beam doses and can be roughly described by the integral over the convolutions of proton fluence and pencil beam dose kernel for all single pencil beams:  $\int(\textit{fluence} * \textit{kernel})$ .

Most pencil beam algorithms only consider scattering by material in the nozzle, e.g. range shifter or scatterers, and in the beam path between nozzle and patient. Some algorithms also try to take into account the energy loss in the tissue, range straggling (if not all particles undergo the same number of collisions) and nuclear interactions. However, there is still room for improvement concerning multiple Coulomb and nuclear scattering. (Fujimoto et al. 2011) (Knutson 2012) (Westerly et al. 2013)

#### Monte Carlo (MC)

Monte Carlo is said to be the gold standard amongst all proton dose calculation algorithms. It provides a yet unsurpassed accuracy and realism. A Monte Carlo algorithm

does not only take into account all primary protons and secondary ions, it also considers all or parts of the following issues: tissue inhomogeneities, a more sophisticated energy loss integration, range straggling, multiple scattering and nuclear interactions. It creates probability distributions including all interactions of every proton. Dose calculated with the MC algorithm is more accurate, for instance if a range shifter is used, or in presence of heterogeneous tissue, as it was recently shown for the used RayStation algorithm by Saini et al. 2017. The only drawback is the long computation time which up to now can only be improved at the expense of accuracy. Thus, Monte Carlo algorithms are currently not used in clinical routine. (Paganetti 2009) (Knutson 2012) (RaySearch 2017a)

### 2.3.3 Dose optimization and evaluation

Optimization concerns mainly the settings for the beam(s) and objectives for the target and organs at risk. The goal is to find a compromise between target coverage with the prescribed dose and organ at risk sparing. Beam computation settings include e.g. energy layer and spot spacing, target margins, and minimal and maximal spot weighting. Objectives are defined by assigning cost functions to parameters, as for example the maximum dose in a given volume. They shall avoid or at least limit over- and underdosage in the target and in organs at risk. The efficiency can be checked by means of clinical goals that can be set manually; a cost function for a region of interest is performing well if the respective clinical goal is fulfilled.

Robust optimization is needed in case of positioning errors, range errors or anatomical changes during the course of the treatment. There is always a present risk of occurrence of one or more of these issues in proton therapy, especially in active beam delivery, i.e. pencil beam scanning. While with passive scattering range uncertainties and setup errors result in dose fluctuations at the target edges, the impact is potentially higher when using the precise active scanning where a homogeneous dose distribution over the whole target is planned and accurately limited to the target edges. Any uncertainty can lead to strong deviations in dose distribution, potentially jeopardizing organs at risk.

Robustness may be improved directly by appropriate selection of beam directions, e.g. avoiding highly heterogeneous regions if possible. There are also attempts to consider uncertainties and errors by calculating probability distributions of variations (cf. Unkelbach et al. 2009) or so called “worst case optimizations” (cf. Pflugfelder et al. 2008, Fredriksson et al. 2011). In general, the better the spot weighting, cost function setting and therefore the target coverage in a treatment plan, the higher is the robustness.

Further information about robust dose optimization can be found in Schwarz 2011.

### **2.3.4 Creation of matching fields**

Usually the field size that can be irradiated with active beam scanning is limited by the scanning magnets to about  $20\text{ cm} \times 20\text{ cm}$ . Consequently, when very large tumors need to be treated, it is necessary to combine two or more irradiation fields. In order to achieve a homogeneous dose distribution without too intense hot or cold spots, the overlapping region(s), also called matching fields, must not fall below a certain size. The performance of the matching can be examined by means of dose-volume histograms (DVH) and line doses, which is described in more detail in subsection 3.2.2.

An important issue is the deviation in dose distribution that might occur during a treatment due to patient movement (more or less volitional, particularly by children, or involuntary as e.g. cardiac palpitations or breathing), positioning uncertainties and beam setup errors. Owing to the increased movement possibility within two or more fields, the robustness to such uncertainties is lower than in case of just one irradiation field.



# 3 Materials and methods

## 3.1 Radiochromic film dosimetry

### 3.1.1 Equipment

For the measurements in the scope of this thesis the following materials and measurement devices were used:

#### Films

- Radiochromic films of the type GAFchromic EBT-3 from Ashland (Bridgewater, NJ, USA), with a total thickness of  $278\ \mu\text{m}$  including an active layer of  $28\ \mu\text{m}$  thickness between two layers of matte surface clear polyester base of each  $125\ \mu\text{m}$  thickness (see Fig. 2.5), lot numbers: 12291502, 06291702. Films were calibrated in the range of 0.2 to 10 Gy.
- Expression 11000XL graphic scanner (Seiko Epson Corporation, Suwa, Nagano, Japan), provided for scanning up to A3 format with high resolution up to  $2400 \times 4800$  dpi (Epson s.a.)

#### Ionization chambers

- Advanced Markus electron chamber (PTW, Freiburg, Germany), sensitive volume of  $0.02\ \text{cm}^3$  and 2.5 mm radius, used without cap
  - Type number TM34045, serial number 001541, calibration factor 1.418, calibrated at 2017/11/29 in reference conditions in water
  - Type number TM34045, serial number 001540, calibration factor 1.34, calibrated at 2018/08/04 in reference conditions in water
- Roos electron chamber (PTW, Freiburg, Germany), type number TM34001, serial number 002460, calibration factor 0.0845 from cross calibration to absolute calibrated Farmer chamber
- UNIDOSwebline universal electrometer from PTW, type number T10021, serial number 000889, 000884 and 000883, cross calibrated with the respective ionization chambers

## Phantoms and software tools

- RW3 slab phantom with water equivalent plates (PTW, Freiburg, Germany), available plate thicknesses: 0.1, 0.2, 0.5, 1 cm
- Matlab software version *R2015a* from Mathworks (Natick, MA, USA) for readout of the optical density and dose calculation

### 3.1.2 Measurement setup

In order to investigate build-up effects on the surface, several measurements were performed with different energies, dose levels and in different depths. The reference measurements in 1 to 2 cm depth with films and ionization chambers should serve as reference for the other measurements on the surface and to check the reliability of the film calibration and the ionization chambers since calibration is always done in reference conditions. The measurements on the surface were performed with films in combination with ionization chambers and only with ionization chambers. The combination was necessary to have a direct reference and an additional measurement point. The ionization chambers were used without films when no depth dose profiles were intended and to have additional reference values. All irradiations were performed on a  $7\text{ cm} \times 7\text{ cm}$  field.

In the following paragraphs measurement settings are listed in the given Tables. The abbreviations M, R and F stand for Advanced Markus chamber, Roos chamber and films. Concerning the phantom position, usually the surface of the phantom was aligned with the isocenter of the beam (hereinafter called “ISD0”). When the range shifter was used, a position 50 cm closer to the nozzle was chosen to avoid spot widening. Furthermore this represents the clinical source to surface distance (SSD) for beams with range shifter and it was also used during the beam model commissioning. Hence, the positions “ISD0” and “ISD50” refer to 66.1 cm and 16.1 cm SSD, respectively.

#### Ionization chamber measurements

All used ionization chambers were pre-irradiated prior to the following measurements. In order to check the performance of the ionization chambers, numbers of particles were divided such as 4 or 6 times 0.5 Gy were measured successively. For the first measurements with two different energies one of the Markus chambers was used and the outcome was compared to the Roos chamber, as the used Markus chamber was not calibrated in the present irradiation room. After the second Markus chamber was calibrated, it was used as the only reference for the films in the subsequent measurements.

Irradiations without films were performed with the configurations and devices listed in Table 3.1. The  $6 \times 0.5\text{ Gy}$  with the Markus chamber were performed in most measurement cycles at least once.

Table 3.1: Ionization chamber measurements

Energy [MeV]	RS	Dose levels [Gy]	Position	Dosimetric devices	Ion chamber SN	Date of measurement
97.4		$3 \times 0.5$	ISD0	M	1541	29/12/2017
97.4		$6 \times 0.5$	ISD0	M	1541	29/12/2017
97.4		$6 \times 0.5$	ISD0	M	1541	24/02/2018
97.4		$6 \times 0.5$	ISD0	M	1540	01/06/2018
97.4	✓	$6 \times 0.5$	ISD0	M	1540	01/06/2018
97.4	✓	$6 \times 0.5$	ISD50	M	1541	24/02/2018
97.4	✓	$6 \times 0.5$	ISD50	M	1540	01/06/2018
179.2		$6 \times 0.5$	ISD0	M	1541	29/12/2017
195.2	✓	2	ISD0	M	1540	01/06/2018

### Measurements in reference conditions

The Roos chamber was used for cross-calibration of the Markus chamber. Due to the location of the sensitive volume of the Roos chamber behind 1 mm water equivalent material, it was positioned at the surface, as well as the Markus chamber positioned behind a 1 mm RW3 plate. This setup should be theoretically equivalent to the Markus chamber when having a stack of 3 films in front. Further measurements were performed with stacks of 3 films and ionization chambers at reference depths of 14 and 19 mm, depending on the energy. Another measurement with 13 mm in front of the Roos chamber was done, even though at this point of the Bragg curve the result should not be different. All performed measurements in reference conditions are listed in Table 3.2.

### Surface dose measurements

In order to investigate depth dose profiles in small depth intervals at a material surface, radiochromic EBT3 films were used. Each film consists of several layers, as it is described in more detail in subsection 2.2.2. Film sheets were cut into pieces of  $4 \text{ cm} \times 4 \text{ cm}$  and composed into stacks of up to 8 films. They were fixed on the surface of the RW3 water equivalent plates which were positioned in the slab holder. The Markus chamber was mounted in the foremost RW3 plate directly behind the film stack. The complete setup at the example of 8 films in front of the Markus chamber is shown in Figure 3.1 from a bird's eye view and in Figure 3.2 from beam's eye view.

In order to assure accurate positioning, the robot, the laser system and the tracking camera were used (cf. section 1.5).

The electrometer for the Markus chamber was set to medium range. The Advanced Markus chamber itself was operated at 300 V. The correction factor for the Markus chamber included corrections for temperature and pressure in the irradiation room, and a calibration correction.

Table 3.2: Reference measurements

Energy [MeV]	RS	Dose levels [Gy]	Position	Dosimetric devices	RW3 thickness [mm]	Film batch number / Ion chamber SN	Date of measurement
97.4		6 × 0.5	ISD0	M	1	1541	29/12/2017
97.4		6 × 0.5	ISD0	R		2460	29/12/2017
97.4		6 × 0.5	ISD0	R		2460	24/02/2018
97.4	✓	4 × 0.5	ISD50	3F+M		06291702/1540	01/06/2018
97.4		4 × 0.5	ISD0	3F	14	12291502	29/12/2017
97.4		4 × 0.5	ISD0	M	14	1541	29/12/2017
97.4		4 × 0.5	ISD0	3F+M	14	12291502/1541	24/02/2018
97.4		2 × 0.5	ISD0	3F+M	14	12291502/1541	24/02/2018
97.4		0.5	ISD0	3F+M	14	12291502/1541	24/02/2018
97.4		4 × 0.5	ISD0	R	14	2460	29/12/2017
97.4		4 × 0.5	ISD0	R	14	2460	24/02/2018
97.4		4 × 0.5	ISD0	R	13	2460	24/02/2018
179.2		6 × 0.5	ISD0	M	1	1541	29/12/2017
179.2		6 × 0.5	ISD0	R		2460	29/12/2017
179.2		4 × 0.5	ISD0	3F	19	12291502	29/12/2017
179.2		4 × 0.5	ISD0	M	19	1541	29/12/2017
179.2		4 × 0.5	ISD0	3F+M	19	12291502/1541	24/02/2018
179.2		2 × 0.5	ISD0	3F+M	19	12291502/1541	24/02/2018
179.2		0.5	ISD0	3F+M	19	12291502/1541	24/02/2018
179.2		4 × 0.5	ISD0	R	19	2460	29/12/2017
179.2		4 × 0.5	ISD0	R	19	2460	24/02/2018

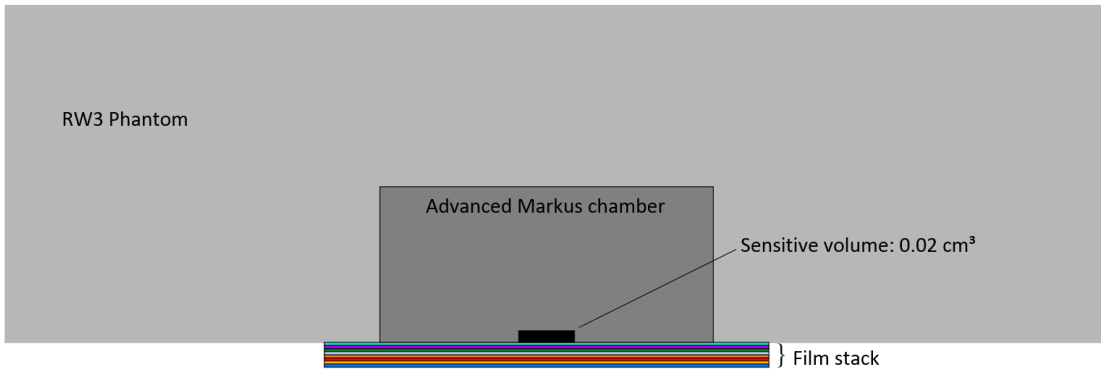


Figure 3.1: Measurement setup with part of the RW3 phantom, Advanced Markus chamber and films from a bird's eye view (own illustration)

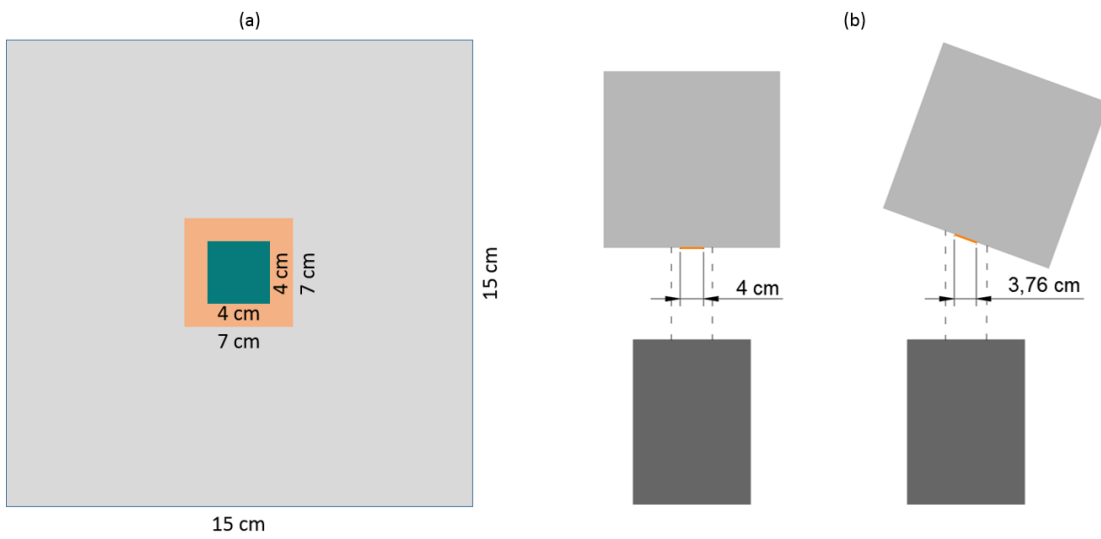


Figure 3.2: Measurement setup: (a) with RW3 phantom (gray), delineation of the irradiation field (orange) and films (petrol) from beam's eye view; (b) for irradiation: nozzle (dark gray), RW3 phantom (gray) and films (orange) straight and tilted by  $20^\circ$ ; (own illustrations)

### 3.1.3 Film irradiation

Irradiations were performed with films and Markus chamber at different dose levels, with three different single energy fields and partly with the range shifter at a lower distance to the nozzle. In addition, spread-out Bragg peak (SOBP) measurements were performed, which included several energies to cover the target region. Details about energies and particle numbers are given later in this subsection. In order to approach the patient geometry with curved surfaces, two measurements were performed on surfaces tilted by  $20^\circ$ , once with a single energy and then with a SOBP.

Concerning the film numbers, at 97.4 MeV with tilted surface up to 8 films were positioned in front of the Markus chamber. For all other energies up to 5 films were used. Table 3.3 shows a detailed list of the measurement settings. For the spread-out Bragg peak with straight beam and the two tilted irradiations the closest possible position was used, which resulted in a SSD of 15.75 cm and 17.35 cm at the center, respectively. The respective setup is shown in Figure 3.2. Note that in the tilted case the width of the films from beam's eye view is smaller because of the inclination (cf. section 4.1). If not otherwise specified, the phantom surface was oriented perpendicular to the beam line. In case of an inclination, the angle is given with respect to the perpendicular orientation.

Table 3.3: Film measurements

Energy [MeV]	RS	Dose levels [Gy]	Position	Angle	Film batch no./ Ion chamber SN	Date of measurement
97.4		1 / 2	ISD0		12291502/1541	29/12/2017
97.4		2	ISD0		6291702/1540	01/06/2018
97.4	✓	1 / 2	ISD50		12291502/1541	24/02/2018
97.4	✓	2	ISD48.75	$20^\circ$	6291702/1540	15/07/2018
179.2		1 / 2	ISD0		12291502/1541	29/12/2017
195.2	✓	1 / 2	ISD50		6291702/1540	01/06/2018
SOBP	✓	2.2(RBE)	ISD50.35		6291702/1540	15/07/2018
SOBP	✓	2.2(RBE)	ISD48.75	$20^\circ$	6291702/1540	15/07/2018

**Constant energies:** For the measurements with a single energy layer a  $7\text{ cm} \times 7\text{ cm}$  field was homogeneously irradiated. In order to achieve that, a spot spacing of 2 mm in x- and y-direction was chosen and the number of particles was defined according to the desired dose level.

For 97.4 MeV the range shifter reduced the range from 70.1 cm to 30.0 cm, and for 195.2 MeV it was reduced from 244.1 cm to 210.2 cm, which equals the range of 179.2 MeV.

**SOBP:** In case of the SOBP plans a volume of  $7\text{ cm} \times 7\text{ cm} \times 3\text{ cm}$  was irradiated with a prescribed dose of 2.2 Gy (RBE). For the straight SOBP plan energies from 71.4 to 101.1 MeV were used. An energy layer spacing of 0.25 cm resulted in 19 energy layers. The total number of spots was 9257 with a spot spacing of 0.5 cm and the spot weight ranging from  $0.9646 \cdot 10^6$  to  $67.1873 \cdot 10^6$  particles per fraction (NP/fx). Concerning the

Table 3.4: Details for film measurements at constant energies

Energy [MeV]	RS	Desired dose [Gy]	NP [ $10^7$ ]	Range [cm]
97.4	✓	0.5	1.465	30.0
97.4	✓	1	2.930	30.0
97.4	✓	2	5.860	30.0
97.4		0.5	1.465	70.1
97.4		1	2.930	70.1
97.4		2	5.860	70.1
179.2		0.5	2.317	210.2
179.2		1	4.634	210.2
179.2		2	9.268	210.2
195.2	✓	1	4.954	210.2
195.2	✓	2	9.908	210.2

tilted SOBP plan, the plan characteristics were similar. The energies ranged from 70.50 to 103.30 MeV through 21 energy layers. In total, 9601 spots were used with a spot weight from  $0.9381 \cdot 10^6$  to  $94.5847 \cdot 10^6$  NP/fx.

### 3.1.4 Film scanning and analysis

#### Film scanning

In order to use films for high resolution dose measurements, they were scanned prior to the irradiation to get the single background doses. 24 to 48 hours after irradiation the scanning of the films was performed in order to account for the post-darkening, as commonly done. The films irradiated with the higher energy level (195.2 MeV) and the SOBP were scanned one week after irradiation because the same was done during calibration of this film batch. Prior to scanning the flatbed scanner was warmed up by performing five preview scans. The film pieces were placed in portrait orientation at the center of the scanner. As scanning program the Epson Scan software was used with the following settings:

- Mode: Professional Mode
- Film type: Positive film
- Image type: 48-bit Color
- Resolution: 150 dpi
- Document size: user-defined in the preview window
- Target size: Original
- Adjustments: no adjustments

- Color: no color correction, medium auto exposure level
- Image format: TIFF (\*.tif)

To ensure accuracy, each irradiated film was scanned three times, which was also used for calculation of standard deviations as described in subsection 3.1.5.

### Film calibration

In order to convert optical density into dose a calibration curve is needed. For each of the two used film batches (lot numbers 12291502 and 6291702) a calibration curve was created in July 2017 and April 2018 at MedAustron. The calibration was established and is explained in more detail in the publication by Khachonkham et al. 2017. For this calibration, films were irradiated with different dose levels (i.e. 0.5, 1, 2, 3, 5, 8, 12 Gy) in a proton beam of 148.2 MeV in standard reference conditions (reference depth 2 cm) in water and RW3 for the first and second calibration curve, respectively. The dependency of optical density (OD) and dose (D) can be described by a 4<sup>th</sup> order polynomial fit using the parameters a to e. The calibration curves were first created for doses up to 10 and 12 Gy, respectively. However, during the analysis only the low dose level part up to 5 Gy was used. The polynomial with the corresponding parameters are as follows:

$$D = a \cdot OD^4 + b \cdot OD^3 + c \cdot OD^2 + d \cdot OD + e \quad (3.1)$$

with  $a = 121.856$ ,  $b = -72.842$ ,  $c = 38.5943$ ,  $d = 7.00571$  and  $e = 0.09519$  for the first film batch. For the second film batch the parameters were  $a = -192.2161$ ,  $b = 160.88287$ ,  $c = -14.37083$ ,  $d = 6.79962$  and  $e = 0$ .

### Film data analysis

The software Matlab was used to read out the pixel values of the three scans over a region of interest of about  $2 \text{ cm} \times 2 \text{ cm}$  in the center of the film. The pixel values were then averaged over the three scans and used for the further dose calculations. The box size of  $2 \text{ cm} \times 2 \text{ cm}$  was chosen because the exposure was assumed to be homogeneous in this field. Close to the edges the inhomogeneity may be worse due to the  $7 \text{ cm} \times 7 \text{ cm}$  irradiation field size and possible layer disintegration. For the tilted films at the single energy, a box size of  $1 \text{ cm} \times 1 \text{ cm}$  was used because of the inhomogeneity effect in the right half of the films. The box was positioned in the center of the left half of each film. Further explanation can be found in section 4.1.

The optical density, correcting for the background pixel value of every specific film piece, was calculated by

$$OD = \log_{10} \left( \frac{PV_B}{PV_I} \right) \quad (3.2)$$

where  $PV_B$  and  $PV_I$  are the background and irradiated pixel values (Devic et al. 2016).

For converting optical density into dose the calibration curves (3.1) were used.

For the second film batch the film results had to be corrected for overestimation of the dose values. The correction factor was generated by scaling the film curve at a depth of 1080  $\mu\text{m}$  to the mean value of the Markus chamber in the range of 720, 1080 and 1440  $\mu\text{m}$  (see subsection 4.1.1).

### 3.1.5 Data analysis

The calculation of the standard deviations was performed using error propagation with the general Formula 3.3.

$$\sigma_{f(p_i)} = \sqrt{\left(\frac{\partial f(p_i)}{\partial p_1}\right)^2 \sigma_{p_1}^2 + \left(\frac{\partial f(p_i)}{\partial p_2}\right)^2 \sigma_{p_2}^2 + \dots + \left(\frac{\partial f(p_i)}{\partial p_n}\right)^2 \sigma_{p_n}^2} \quad (3.3)$$

In the error propagation the following dose calculation steps were considered: original standard deviation from each film scan, averaging of the pixel values over three scans per film (see subsection 3.1.4), optical density calculation from the pixel values for each film, and dose calculation using the calibration curve (see subsection 3.1.4).

## 3.2 Treatment planning on extremity sarcoma

The treatment plans for the large extremity sarcoma were created with the RayStation<sup>®</sup> v6.99 treatment planning system of RaySearch Laboratories (Stockholm, Sweden). For plan creation and dose calculation the clinical CT data of the respective patients, which were treated with photon therapy at the AKH, were used employing a generic calibration curve. The fundamental treatment workflow is described in sections 1.4 and 2.3.

Since the scanning magnet at MedAustron (Wr. Neustadt, Austria) can only deflect the ion beam by 10 cm from the center in horizontal and vertical directions, there is an effective irradiation field of a maximum of 20 cm  $\times$  20 cm possible for each beam. Depending on the maximum length of each tumor, either two or three parallel proton beams with shifted isocenters were required to cover the whole field length. It was intended that the matching area, i.e. the overlapping irradiation field of the beams, were chosen as large as possible to have an ideal coverage of the tumor region.

In total, 5 patients were selected for this study. All of them suffered on extremity soft tissue sarcoma larger than 20 cm. For each sarcoma, the CTV was defined as the tumor region on the CT and the PTV was defined as the CTV including uncertainty margins. The dimensions of the CTVs, PTVs and matching fields are listed in Table 3.5. The tumor extension in beam direction is further referred to as thickness.

Table 3.5: Sarcoma and planning dimensions and volumes for patients P1 to P5 (own naming)

	<b>P1</b>	<b>P2</b>	<b>P3</b>	<b>P4</b>	<b>P5</b>
CTV volume [ $cm^3$ ]	1245	1875	296	n.a.	1642
PTV volume [ $cm^3$ ]	1622	2240	420	4221	2022
Skin (2mm) volume [ $cm^3$ ]	150	205	69	243	313
Bone volume [ $cm^3$ ]	444	548	134	492	491
CTV length [cm]	23	30	23	36	31
CTV thickness (BEV) [cm]	9	9	2.5 - 3	9	8.3
Matching field length (spots) [cm]	5.6	2.3	14	8.7 / 8	3.7
PTV intersection length [cm]	2.8	1.6	8.9	4.8 / 4.8	3.6
Extremity	left thigh	left thigh	left upper arm	right thigh	right thigh

The most important coverage criterion was the minimum dose to 98% of the clinical target volume ( $D_{98\%}$ ). Hot spots exceeding approximately 104%, or at least 107%, of the dose should be avoided, according to internal guidelines at MedAustron. Furthermore, bone and skin should be covered homogeneously by maximum 100% of the prescribed dose, in consideration of the clinical goals for bone and skin treatment area, which are shown in Table 3.6. The skin goal is based on clinical experiences of operating proton and carbon ion centers (cf. Yanagi et al. 2009). Accordingly, the maximum dose to the skin during a radiotherapy treatment should be limited to 60 Gy. When the received dose exceeds this limit, the risk of skin burns increases dramatically. The other clinical goals originate from the internal treatment planning guidelines for extremity sarcoma at MedAustron. The compliance or non-compliance with these clinical goals is directive during the optimization and evaluation process. In the end it reflects the quality of the respective plan.

### 3.2.1 Treatment plan creation

First the tumor ROI was separated in the required number of parts - usually two or three - and each was expanded in superior and/or inferior direction, with the aim of overlapping tumor ROI parts, as it can be seen in Figure 3.3. The two or three beams were then defined at the isocenters of the respective tumor parts. The treatment was planned for a total biological dose of 60 Gy (RBE), divided into 30 fractions of 2 Gy (RBE) each. The gantry angle was set to  $90^\circ$  as only a horizontal beam line was available at MedAustron at the moment. A 3 cm thick range shifter out of PMMA was set to degrade the beam energy in order to cover the superficial tumors. The gap between nozzle and patient was set to constant 20 cm. In order to achieve a homogeneous dose distribution and to avoid

Table 3.6: Clinical goals

PTV	Dose of at least 57.00 Gy at 98 % volume
PTV	Dose of at least 54.00 Gy at 98 % volume
PTV	Dose of at most 64.20 Gy at 0 % volume
PTV	Dose of at most 64.20 Gy at 2 % volume
Bone	Dose of at most 64.2 Gy at 2 % volume
Vessels	Dose of at most 70.00 Gy at 0.1 cm <sup>3</sup> volume
Nerves	Dose of at most 70.00 Gy at 0.1 cm <sup>3</sup> volume
Compartment	Dose of at most 60.00 Gy on average
Skin treatment area	Volume of at most 4.0 cm <sup>3</sup> at 60.00 Gy dose

significant over- or underdosage, objectives were defined for maximum and minimum doses and dose fall-offs for different body parts, such as the planning target volume and organs at risk (OARs), like bones, vessels and nerves. An example in Table 3.7 shows the approximate dose regions desired for every organ. A constraint was set on the 2 mm skin in the treatment area in order to spare this part explicitly as required. The PTV less the skin is called ‘help PTV’ and shall avoid spot positioning directly at the surface. The irradiated 2 mm skin part is called ‘skin treatment area’ (see Fig. 3.3); femur and humerus are grouped together as ‘bones’. Eventually, an additional intersection ROI between the single PTV parts was necessary, called ‘help PTV intersection’.

Table 3.7: Objectives

Function	ROI	Description	Weight
Dose fall-off	Body/External	[H]57–60 Gy [L]20–30 Gy, Low dose distance $\sim 1.5$ cm	0 up to 40
Uniform dose	help_PTV	60 Gy	50 up to 100
Minimum dose	help_PTV	59–60 Gy	100 up to 200
Maximum dose	help_PTV	60–61 Gy	100 up to 200
Maximum dose	Skin treatment area	58–60 Gy	0 up to 40
Maximum dose	Bones	56–60 Gy	0 to 80
Maximum dose	help_PTV_intersection	59.5–60.5 Gy	0 up to 200

The beam computation settings were set in the beginning and adapted during the planning. This includes energy layer (EL) spacing, spot spacing and further target margins. Energy layer and spot spacing can be set as user-defined constant values or as automatic distance with a definable scaling factor. In terms of EL spacing the automatically selected distance depends on the Bragg peak width; for the spot spacing it depends on the radial spread in the Bragg peak (cf. RaySearch 2017b, p.579). The aim was to achieve a continuous target coverage without hotspots in the skin region or other OARs, maximum 60 energy layers, an EL spacing smaller than 3.3 MeV and still no significant spot filtering, and a spot spacing of maximum 0.5 cm.

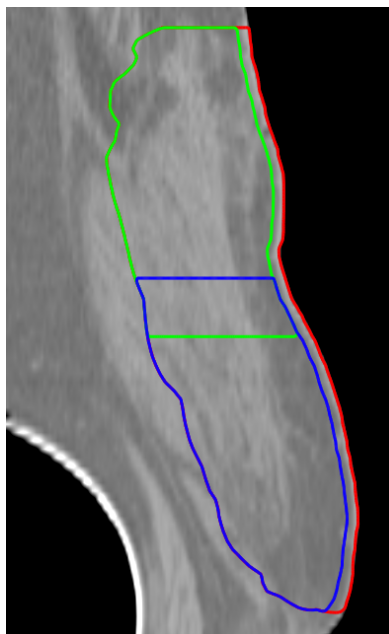


Figure 3.3: Delineation example (P5) with superior PTV part (green), inferior PTV part (blue), intersection part, and skin treatment area (from right PTV edges until red delineation); (own illustration)

The first few optimizations, intended to test rough settings, were performed using the PB algorithm since it needs much less computation time than the MC algorithm. The further calculations of spot positions and weights as well as the final dose calculations were performed using the Monte Carlo method, with 10000 ions per spot for optimization and 0.5% uncertainty for final dose calculation.

### 3.2.2 Robust treatment plan analysis

Uncertainties due to setup or patient positioning, for example, can result in dramatic changes in dose distribution (cf. subsection 2.3.3). As already mentioned in section 3.2, the isocenters of the beams were shifted in opposite directions by 5 mm each in longitudinal direction in order to get more and less overlapping tumor parts, respectively. The outcome was compared by means of skin dose and PTV coverage. This was performed by looking at 3-dimensional information provided by dose difference maps and line doses across the tumor volume, and 2-dimensional information from dose-volume histograms and dose-volume parameters.

Dose-volume histograms (DVHs) represent the dose values of a selected organ. The dose to volume can be plotted in absolute or relative values, whereas commonly the dose is given in Gray, i.e. absolute, and the volume is displayed in percent, i.e. relative. As the DVH summarizes the dose distribution to a volume of interest (VOI), it can be used

for determination of the above described dose-volume parameters, as for example the mean dose to a specific volume ( $D_{\text{mean}}$ ), the dose to 98% of the volume ( $D_{98\%}$ ) and the dose to 2% of the volume ( $D_{2\%}$ ). The best coverage of the target would be achieved if 100% of the volume received exactly 60 Gy, which would result in a rectangular DVH curve. (ICRU 2007)

The results of the robust analysis are presented in section 4.2.



## 4 Results

### 4.1 Surface dose measurements

Prior to analyzing the performed measurements in detail some preliminary investigations were necessary in order to investigate the dosimetric impact of a change in SSD and to determine a correction procedure in case of strongly deviating film calibration curves. They are described in subsection 4.1.1.

The first detailed analysis aimed at the investigation of possible influences by the range shifter on dosimetric film and Markus chamber measurements, in order to allow correct comparing of measurements with and without range shifter (see subsection 4.1.2). The further steps included a detailed characterization of the build-up in subsection 4.1.3, measurements on a tilted surface, getting closer to the real patient geometry (subsection 4.1.4) and analyses of SOBP irradiations (subsection 4.1.5). As listed in chapter 3 the build-up region was supposed to be investigated for three dose levels, 0.5 Gy, 1 Gy and 2 Gy. Since different challenges came along during the measurements the main focus was put on the 2 Gy level and the low dose levels were not included for detailed analysis but only in a side chapter (4.1.6) at the end of this section.

It has to be noted that the measured doses are given as physical doses, unless otherwise indicated.

#### 4.1.1 Preliminary investigations

##### Change of SSD

As described in section 3.1.2, a reduced distance between phantom and nozzle reduces the spot widening and scattering and results in a higher dose for a single energy field with the same spot weighting. In order to accurately compare the measurement results without RS at ISD0 and with RS at ISD50, the magnitude of the dose difference between the positions at ISD0 and ISD50 was investigated for the measurements which were acquired at both ISDs. The position shift by 50 cm in beam direction led to a dose increase of 34 % for 97.4 MeV and 17 % for 195.2 MeV, measured with the Markus chamber positioned at the center of a 7 cm × 7 cm single energy field and at the surface of an RW3 stack.

##### Film calibration curve corrections

In case of the 195.2 MeV measurement – performed with the second film batch (lot number 6291702), which was calibrated as described in subsection 3.1.4 – the film dose values exceeded the Markus chamber dose values by approximately 8 % and therefore had to be corrected by a correction factor. This factor was established by aligning film and Markus

chamber dose values at a depth of  $1080\ \mu\text{m}$ . To achieve the dose values at  $1080\ \mu\text{m}$  the film dose values for depths of  $900\ \mu\text{m}$  and  $1260\ \mu\text{m}$  and the Markus chamber dose values for depths of  $720\ \mu\text{m}$ ,  $1080\ \mu\text{m}$  and  $1440\ \mu\text{m}$  were interpolated. The corrected film doses showed deviations of approximately 1% compared to Markus chamber measurement values for depths up to  $700\ \mu\text{m}$  and deviations below 0.3% for depths larger than  $700\ \mu\text{m}$ , as depicted in Figure 4.1 for the 195.2 MeV measurement.

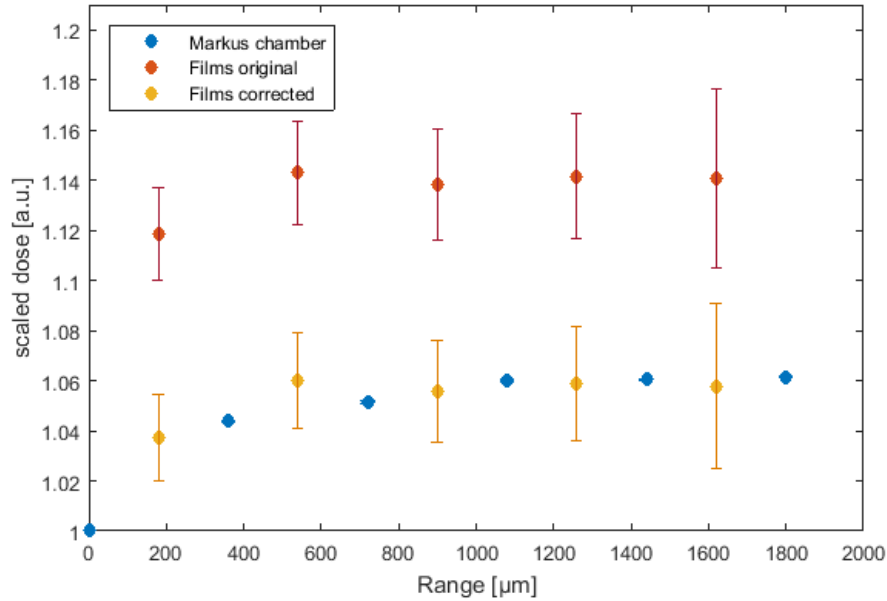


Figure 4.1: Comparison of original and corrected film doses for 195.2 MeV with RS, combined with Markus chamber results; the respective standard deviations are shown as error bars; (own illustration)

#### 4.1.2 Influence of the range shifter on film and Markus chamber doses

The range shifter is necessary for irradiation of volumes that are closer to the surface than 3 cm WET. The lowest energy achievable with the synchrotron at MedAustron is 62.4 MeV, which equals a minimum particle range of about 3 cm in tissue. The range shifter reduces the range (and therefore the energy), i.e. it shifts the Bragg peak to the surface. The range of the used 179.2 MeV without range shifter (21 cm) therefore corresponds to the range of 195.2 MeV with range shifter. The purpose of the following analyses was to investigate if the scattering and spot widening caused by the range shifter has an influence on the build-up shape itself or on dosimetric characteristics of films and Markus chamber.

For the low energy level of 97.4 MeV measurements were performed with and without range shifter, resulting in two low energy levels that can be considered, namely

97.4 MeV and 62.4 MeV. The dose values for 97.4 MeV with and without range shifter at ISD0, measured with the Markus chamber at the surface of an RW3 stack, agreed well (see Figure 4.2) and the dose difference caused by the different energies was only 0.14 Gy (8%). The Markus chamber measurements with 179.2 MeV without RS and 195.2 MeV with RS agreed perfectly, as depicted in Figure 4.3. Regarding the films, they showed a good agreement within 1.2% (without considering standard deviations) with the Markus chamber at 62.4 MeV, 97.4 MeV, and 179.2 MeV nominal and obtained with range shifter, respectively.

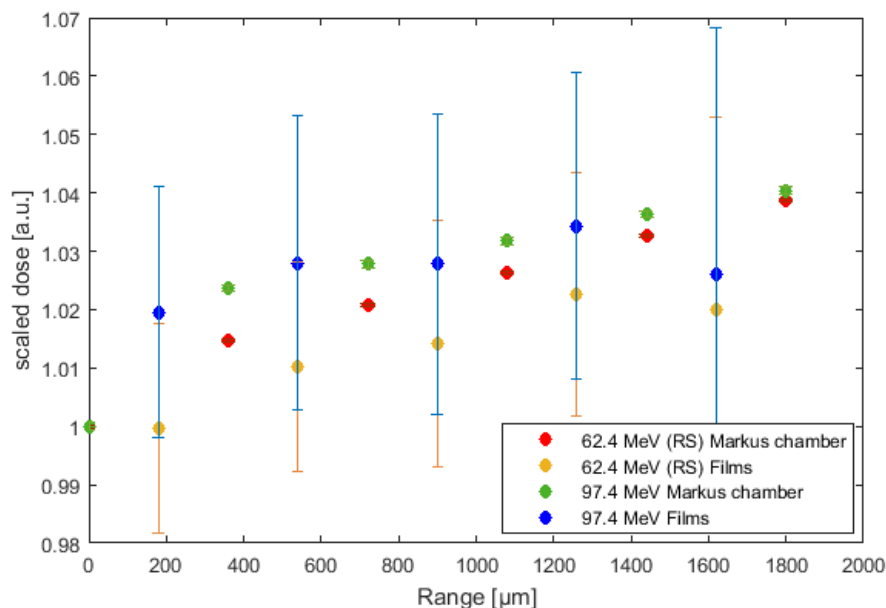


Figure 4.2: Comparison of 62.4 MeV, acquired with RS, and 97.4 MeV, regarding film and Markus chamber results; (own illustration)

This almost perfect agreement in the build-up shape measured with the Markus chamber as well as the agreement of the film measurements show that the range shifter only varies the energy and therefore the range, but has no further influences on the dosimetric characteristics of films and Markus chambers.

Regarding the combination of range shifter and ISD shift by 50 cm, as it was used in most of the performed measurements, the total dose increase summed up to 0.8 Gy (44%) for 97.4 MeV.

### 4.1.3 Build-up characterization

Energies of 62.4 MeV (97.4 MeV with RS), 97.4 MeV, 179.2 MeV and 179.2 MeV as result of 195.2 MeV with RS at 2 Gy (RBE) were compared in order to determine the differences in the build-up curves for different energies. The purpose of this part was to determine

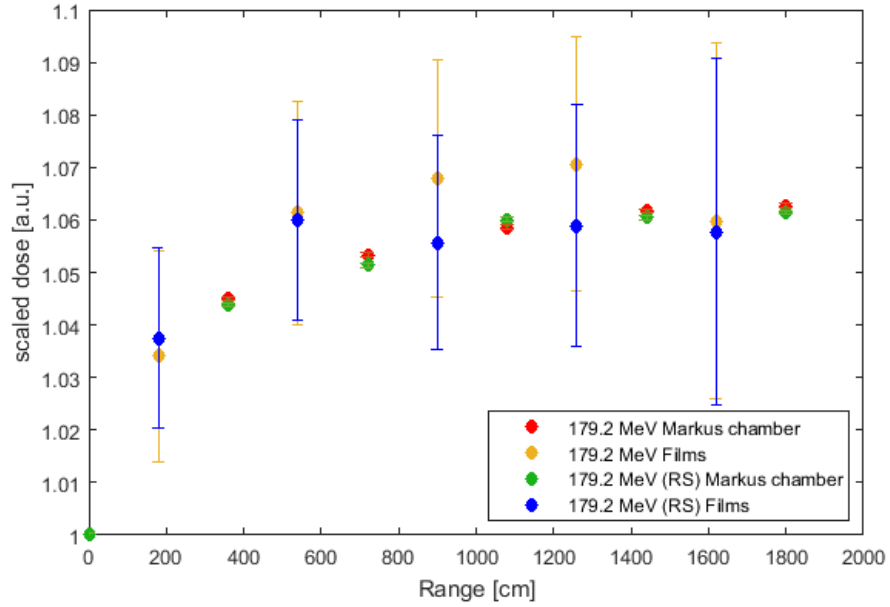


Figure 4.3: Comparison of 179.2 MeV (nominal) and 179.2 MeV acquired by RS; (own illustration)

if the shape of the build-up within the first 3 mm could be predicted for any arbitrary energy.

### Measurement analysis

All measurements showed a steep dose increase at the beginning of the build-up curve. This was observed directly at the surface within the first  $360 \mu\text{m}$ , independently of the use of the range shifter, followed by a moderated increase (see Figure 4.5). The gradient for the superficial part was higher with higher energies (see Figure 4.6), whereas the build-up progressions between  $360 \mu\text{m}$  and  $1800 \mu\text{m}$  was comparable, as shown in Figures 4.5 and 4.7. The film doses displayed a dose drop at the last measurement point (depth =  $1620 \mu\text{m}$ ) by 0.27 % for 62.4 MeV and 0.8 % for 97.4 MeV, compared to the dose at the previous depth ( $1260 \mu\text{m}$ ). This was only partly confirmed for the other energies, as the dose decreased by 0.1 % for 195.2 MeV with RS, i.e. 179.2 MeV, and increased by 1.1 % for 179.2 MeV (nominal).

Regarding the depth-dose curves of Markus chamber and films for the applied energies, a plateau could be defined using respective fit curves, weighted by the standard deviations, beginning from  $360 \mu\text{m}$ . The depth where the plateau was reached was defined as depth where the fit curve increased less than 0.08 % over a range of  $100 \mu\text{m}$ . As depicted in Figure 4.4, the plateau depths are  $1800 \mu\text{m}$ ,  $1300 \mu\text{m}$ ,  $1400 \mu\text{m}$  and  $1500 \mu\text{m}$  for energies of 62.4 MeV, 97.4 MeV and 179.2 MeV, acquired nominally and with range shifter, respectively.

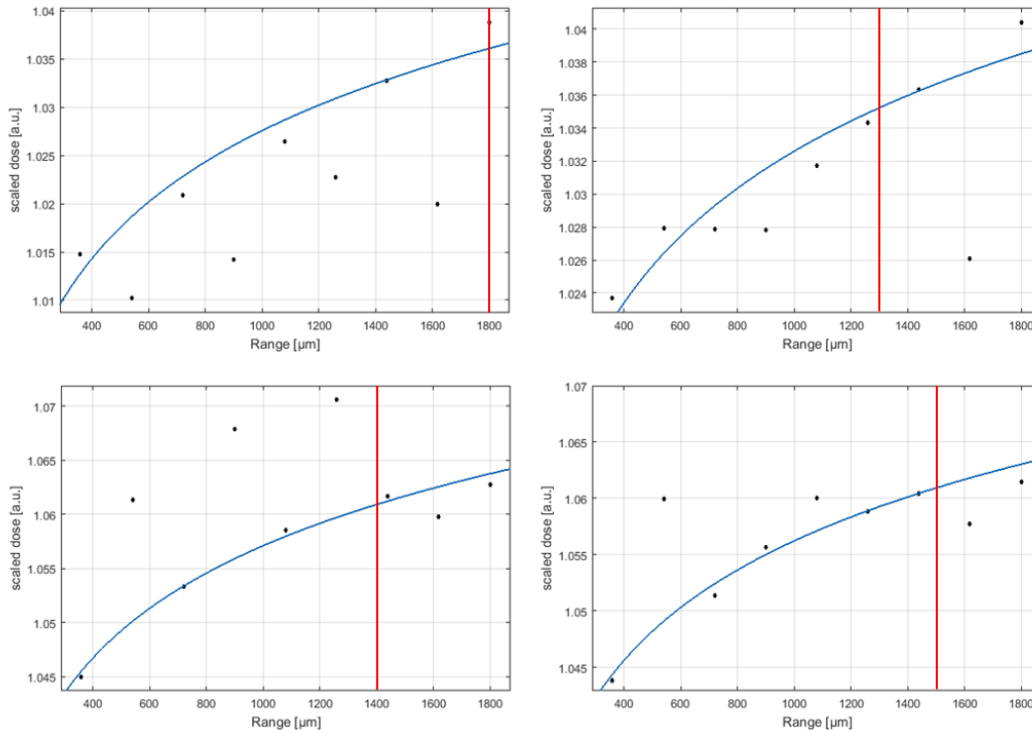


Figure 4.4: Plateau depth (red) in weighted logarithmic fit (blue line) of film and Markus chamber results (black points) for 62.4 MeV (97.4 MeV with RS) and 97.4 MeV (upper row), and 179.2 MeV acquired nominally and from 195.2 MeV with RS (lower row); (own illustration)

### Modelling of the build-up region

Since the films showed this dose drop at the end of the measured range and due to their standard deviations of 1 to 3 % only Markus chamber results (with standard deviations of about 0.5 %) were used for modelling of the build-up region.

In order to compare the shape of the build-up independently of the absolute dose, all values were scaled to the respective Markus chamber values at  $0 \mu\text{m}$ . Based on the findings presented in 4.1.3, the build-up region up to  $2000 \mu\text{m}$  was fitted in two parts. For the first part a linear fit (Formula 4.1) using energy dependent gradients was established. The gradient  $k$  can be determined from an energy dependent logarithmic function (see Fig. 4.6), presented by Formula 4.2.

$$y = kx + 1 \quad \text{with } x = \text{depth } [\mu\text{m}] \quad (4.1)$$

$$k = 5.695 \cdot 10^{-5} \cdot \log(x) - 0.0001939 \quad \text{with } x = \text{energy [MeV]} \quad (4.2)$$

In more detail, the initial steep build-up within the first  $360 \mu\text{m}$  was characterized by two Markus chamber measurement points ( $0 \mu\text{m}$  and  $360 \mu\text{m}$ ), investigated for all measured energies. Approximating this steep dose increase as a linear function with gradient  $k$ , it emerged that the lowest energy (97.4 MeV with RS, i.e. 62.4 MeV in fact) had the lowest gradient, the 97.4 MeV without RS were in the middle and the 179.2 MeV without RS and 195.2 MeV with RS (i.e. 179.2 MeV) had an almost equal and also the highest gradient. According to this observation, the gradient was plotted against the energy and a logarithmic fit was found to fit best. By means of this fit curve, the approximate gradients for different energies are determinable. The build-up between  $360 \mu\text{m}$  and  $2000 \mu\text{m}$  seems to be independent from the energy (see Fig. 4.7) and can be described using the energy independent logarithmic function in Formula 4.3.

$$y = 0.01157 \cdot \log(x) + 0.9313 \quad \text{with } x = \text{depth } [\mu\text{m}] \quad (4.3)$$

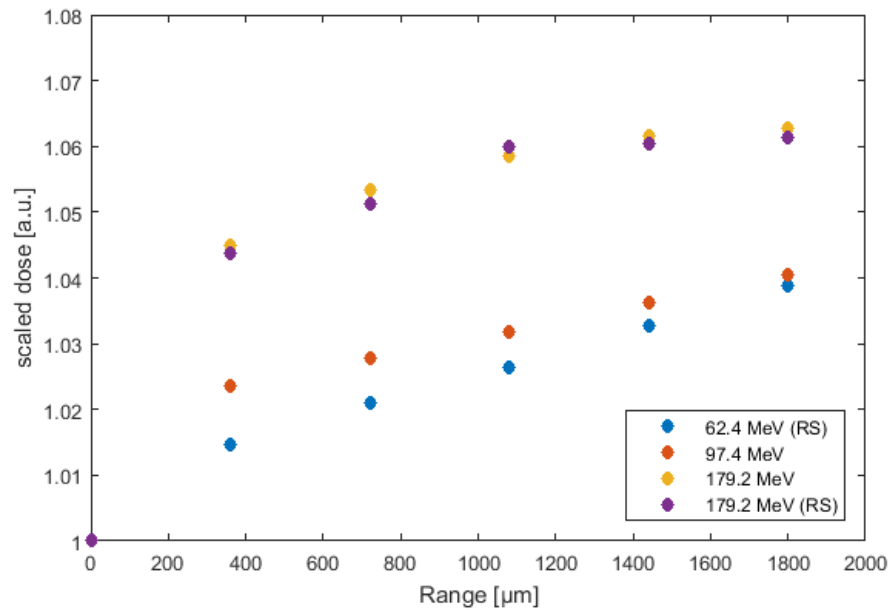


Figure 4.5: Build-up for different energies (note: since the standard deviations of the Markus chamber are very low, they were omitted); (own illustration)

#### 4.1.4 Tilted surface

In order to get closer to the real patient geometry with curved surfaces, the phantom was tilted by  $20^\circ$  with respect to the beam direction, as it was listed in chapter 3. To reduce

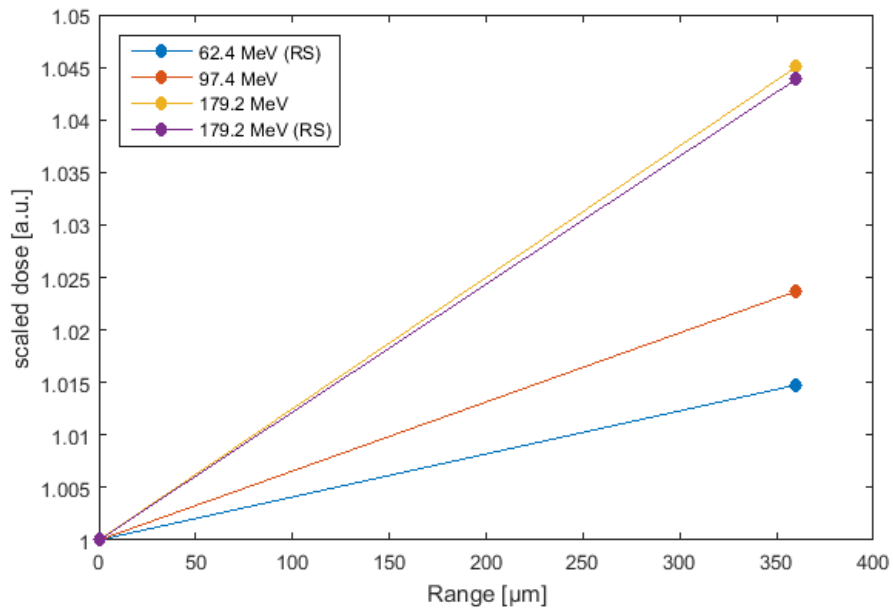


Figure 4.6: Build-up model: first part from 0 to 360  $\mu\text{m}$ ; (own illustration)

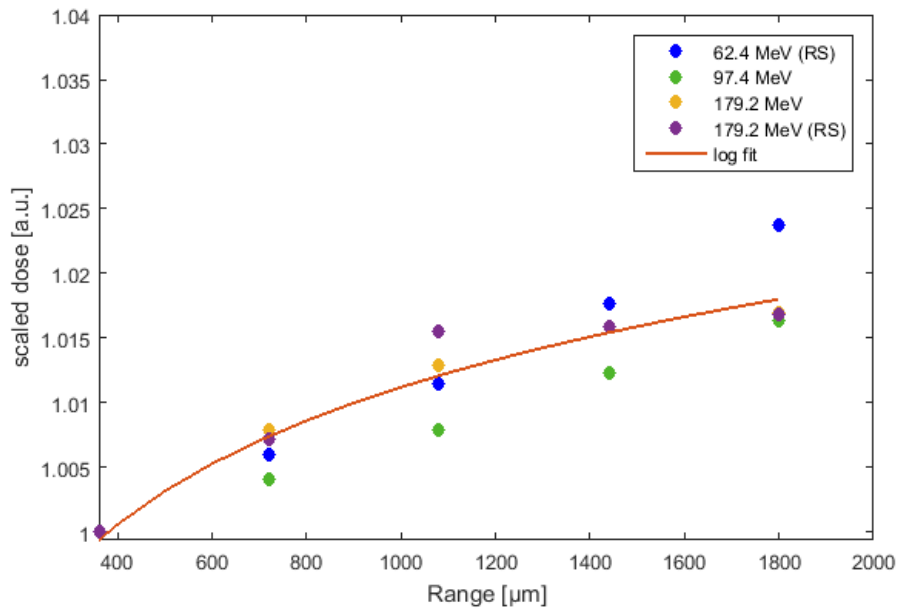


Figure 4.7: Build-up model: second part from 360 to 1800  $\mu\text{m}$ , fit acquired from measurements at the displayed energies; (own illustration)

the penumbra of the spots the phantom position was chosen as close as possible which resulted in a SSD of 17.35 cm, i.e. 1.25 cm further away than for the other irradiations with range shifter. In this position the build-up region was characterized for 97.4 MeV.

### Build-up region characterization

The Markus chamber values showed a good agreement between straight and tilted surface considering the shape of the build-up curve (Fig. 4.8). Comparing the absolute dose values of the tilted and the straight surface, the measured dose values for the tilted surface were on average lower by 8.6%. Anyhow, when normalizing to the entrance dose, the shapes of the build-up curves were comparable.

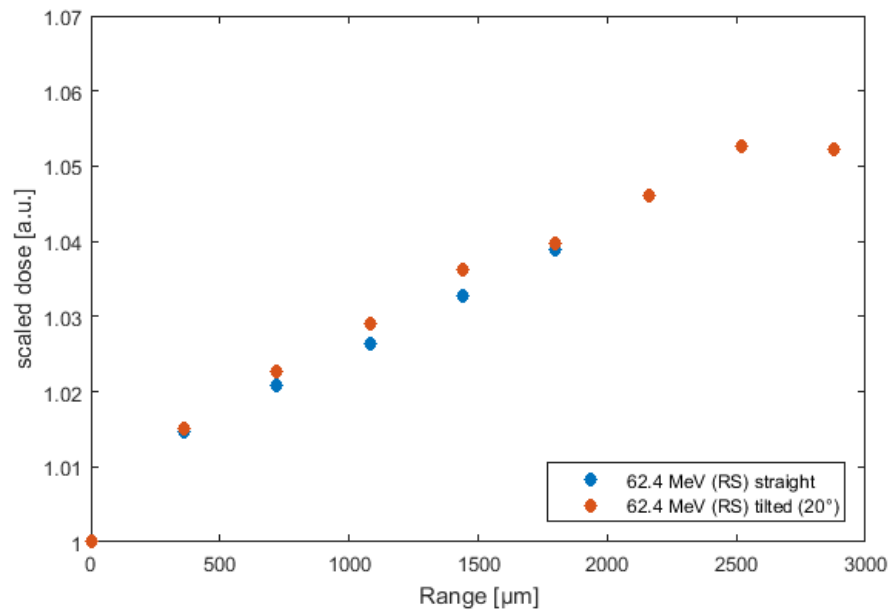


Figure 4.8: Comparison of Markus chamber results from measurements on straight and tilted surface at 62.4 MeV (RS); (own illustration)

### Film characteristics at tilted surfaces

For the films an unexpected lateral dose distribution was observed, as it can be seen in the example of Figure 4.9. All films that were irradiated with a tilted beam at 62.4 MeV (97.4 MeV with RS) showed a higher optical density and therefore a lower dose in the area that was located closer to the nozzle and a higher dose in the area that was further away due to the tilt. The dose over the whole film width (except 1.4 mm at the edges) ranged from 1.75 Gy to 2.50 Gy for a single film in front of the Markus chamber (measurement depth: 180 μm). This equals a dose difference within one film of 0.75 Gy (30% from the maximum value) for an SSD difference of 1.4 cm.

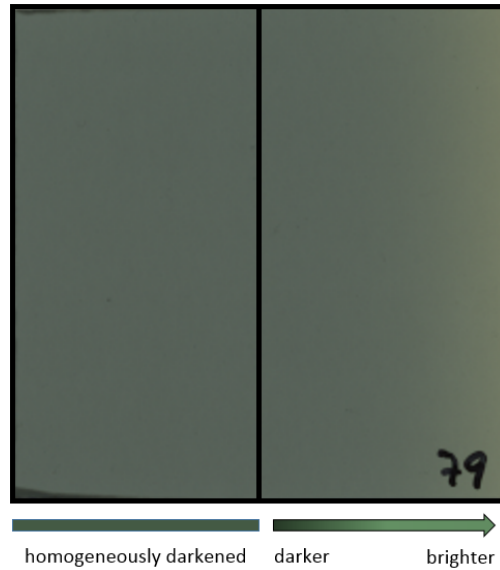


Figure 4.9: Example of tilted film: the left half was further away from the nozzle and homogeneously darkened, the right half was closer and showed inhomogeneous darkening; (own illustration)

In order to evaluate at which position on the film the dose loss starts, the film was analyzed over the length in  $1\text{ cm} \times 1\text{ cm}$  boxes, positioned every  $1.7\text{ mm}$ , which resulted in a dose distribution shown in Figure 4.10 (note: an increasing OD equals a decreasing dose; for relation between OD and dose see subsection 3.1.4). As the OD increase apparently starts between  $20$  and  $25\text{ mm}$ , this region was further analyzed with  $0.2\text{ cm} \times 2\text{ cm}$  boxes positioned every  $0.2\text{ cm}$ . This also lowered the corresponding standard deviations, since the dose variation within the thinner analyzed areas were lower. The analysis revealed a starting point for the OD increase of  $20.5\text{ mm}$ , i.e. approximately at the center of the film. This equals a distance of  $3.45\text{ cm}$  from the right edge (tilted towards to nozzle) of the  $7\text{ cm} \times 7\text{ cm}$  irradiation field.

For comparison, also a film irradiated in straight position was analyzed in more detail. Dose losses of  $1.5\%$  and  $3\%$  were found at left and right film edges, respectively, starting approximately  $1\text{ cm}$  from the edges.

In the further analysis only the part of the film which showed a homogeneous dose distribution was used. Since the films for these measurements were also calibrated with the calibration curve from subsection 3.1.4 and originated from the film batch 6291702, they also needed correction when comparing to the Markus chamber. In the same way as it was described in 4.1.1 for the measurement with  $195.2\text{ MeV}$ , the film values were adapted to the Markus chamber values at a depth of  $1620\text{ }\mu\text{m}$ . The resulting depth-dose curve is shown in Figure 4.11.

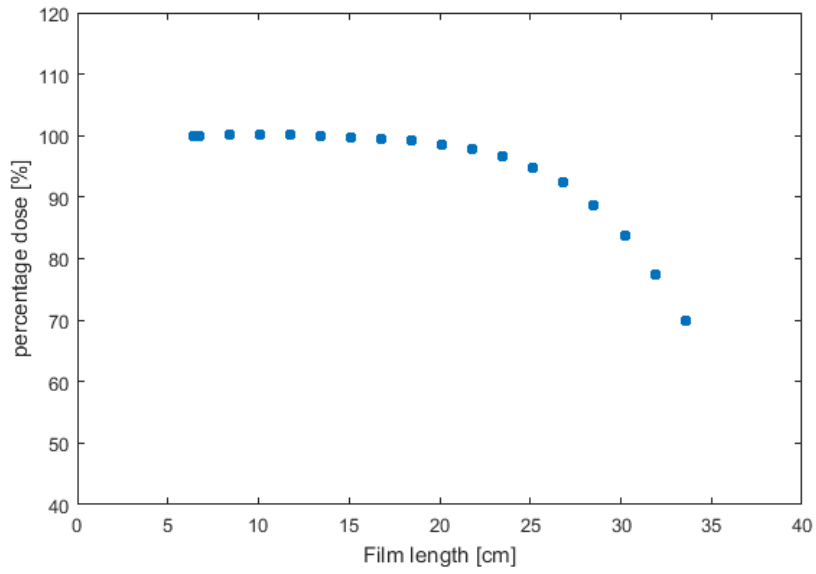


Figure 4.10: Dose distribution over film length in case of tilted films (own illustration)

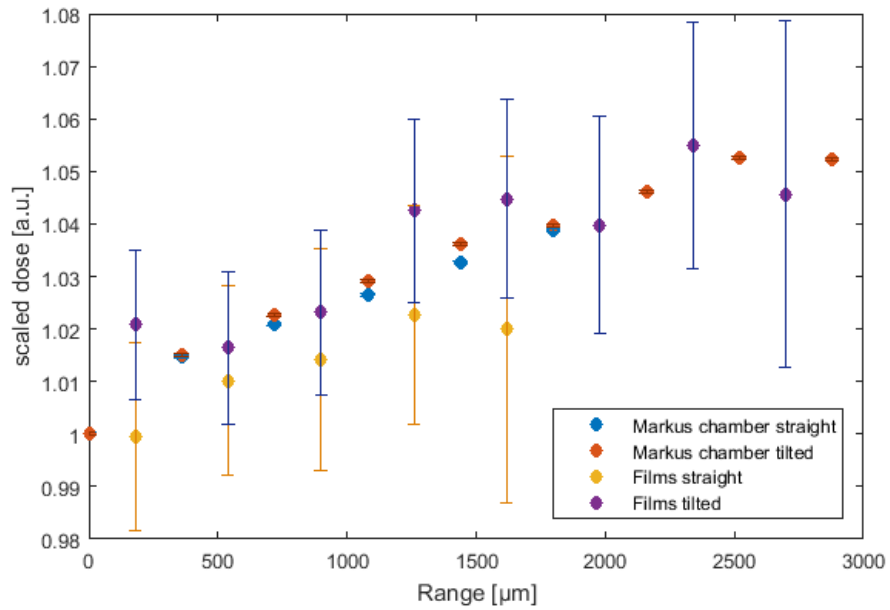


Figure 4.11: Comparison of film and Markus chamber measurements on straight and tilted surfaces at 62.4 MeV (own illustration)

### 4.1.5 SOBP measurements

In contrast to the single energy layer measurements less points were measured within the SOBP. The Markus chamber was positioned directly at the surface and behind a stack of three films in a depth of  $1080\ \mu\text{m}$ .

#### SOBP irradiation at straight and tilted surface

The SOBP irradiations were performed at straight and tilted surfaces, as described in subsection 3.1.3. The results were compared to the film and Markus chamber results of the single energy layer measurements.

The measurements on the straight surface as well as on the tilted surface resulted in quite good agreement of film and Markus chamber results, when considering the standard deviations of the films of approximately 5%. Combining film and Markus chamber values (scaled) and comparing them for straight and tilted cases resulted in a good agreement as well, as it can be seen in Figure 4.12. The deviation between the dose values of the Markus chamber on straight and tilted surface was 2.6% on average. The film dose values of the tilted measurement showed higher doses by 1.8% to 4.8%, compared to the straight measurement.

Comparing the SOBP results with the single energy layer measurements at different energies, they agreed very well. Considering the strong inhomogeneities in dose distribution over the film length in the tilted case that was described in subsection 4.1.4, the tilted films irradiated with the SOBP did not show this strong effect.

#### Application of build-up model on a SOBP

According to the calculations in subsection 4.1.3 the build-up for all energies that were used to create the SOBP could be modelled, as shown in Figure 4.13. The model predicted the two values measured with the Markus chamber in depths of  $0\ \mu\text{m}$  and  $1080\ \mu\text{m}$  quite well. It showed small underestimation of 0.12% to 0.9% in comparison to the depth-dose curves for the largest energy (104.7 MeV) up to the smallest energy (70.5 MeV).

### 4.1.6 Film and Markus chamber measurements at low dose levels

The measurements at lower dose levels showed quite good agreement between films and Markus chamber for all used energies. The major difference compared to the 2 Gy dose level was that the build-up was much less pronounced.

The film doses showed deviations from the Markus chamber of 0.7–3% for the 1 Gy dose level and 2–6% for the 0.5 Gy dose level. A comparison of the 1 Gy measurements at 179.2 MeV, nominal and acquired with RS, resulted in good agreement, as it can be seen in Figure 4.14.

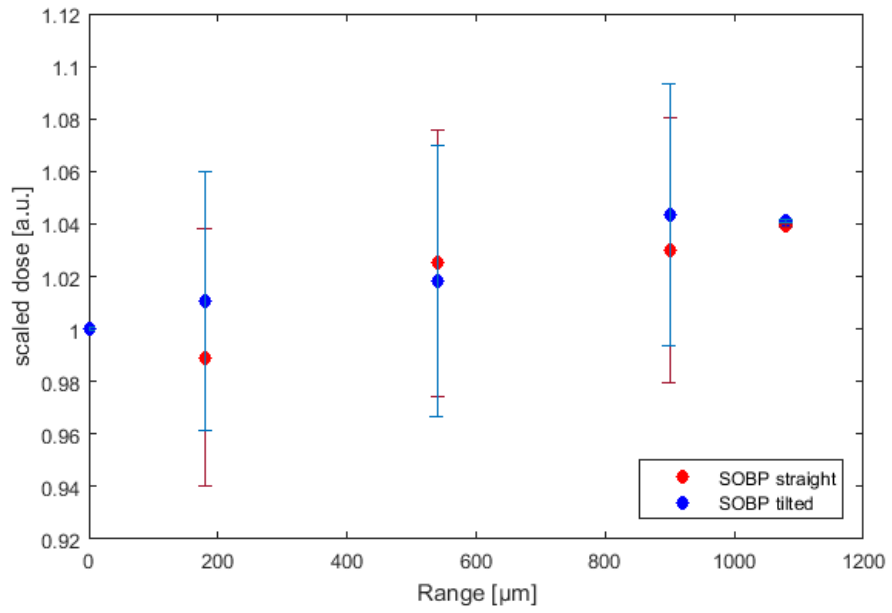


Figure 4.12: Comparison of SOBP measurements on straight and tilted surface with films and Markus chamber (own illustration)

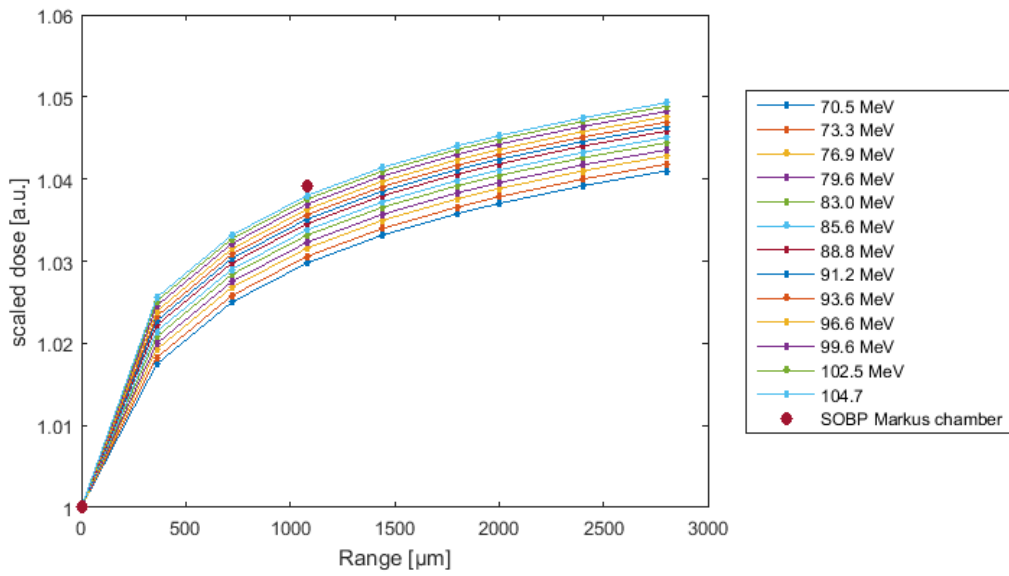


Figure 4.13: Application of model on the single energies used for the SOBP, compared to the Markus chamber results (own illustration)

Comparable to the results of the 2 Gy level, described in subsection 4.1.3, a higher steepness of the initial build-up within the first 360  $\mu\text{m}$  for higher energies was observed for the low dose levels, as Figure 4.14 shows.

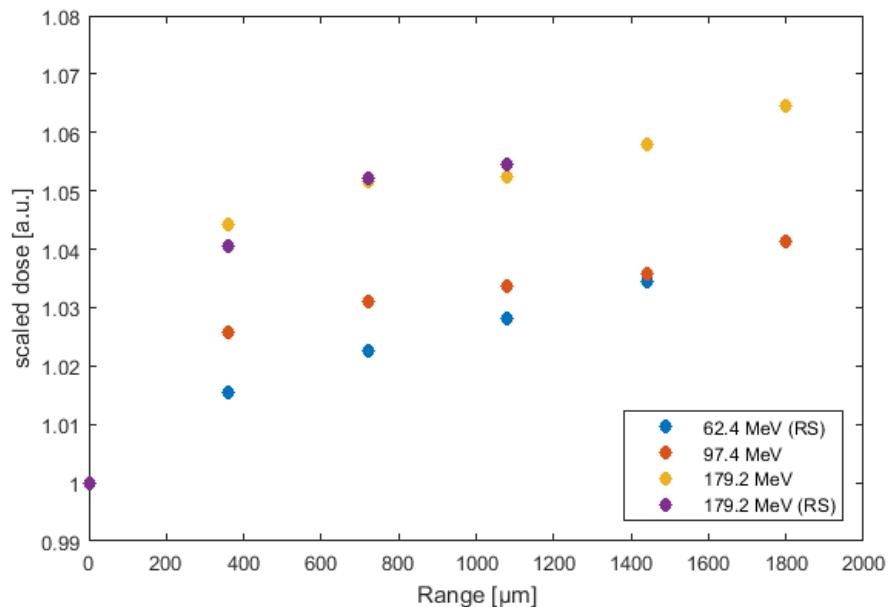


Figure 4.14: Measured Markus chamber results for a dose level of 1 Gy at different energies (own illustration)

## 4.2 Treatment planning

Five sarcoma cases were chosen for this study: P1, P2, P3, P4 and P5. As already listed in section 3.2, the target volumes differed in size, shape and location. The lengths of the matching fields were chosen as large as possible, limited only by the maximum irradiation field size of 20 cm  $\times$  20 cm (in effect 17 cm  $\times$  17 cm plus 1.5 cm at both edges for spot positioning outside the target; see Figure 4.15) available at MedAustron. As the overlap of two irradiation fields has to be considered as well, the maximum possible target size per field is further reduced, depending on the desired overlapping region, which should be as large as possible. Therefore the maximum field size is 17 cm  $\times$  17 cm when allowing one matching boarder and not considering any limitations for the overlapping length. The major challenge for ideal plan quality was to find the best matching field while sparing the skin volumes and being robust against mispositioning, as described in subsection 3.2.1.



Figure 4.15: Schematic illustration of matching technique (own illustration)

#### 4.2.1 Treatment plan setup

The examined sarcomas were located in the upper arm for P3 and in the left or right thigh for the other cases. The total planned dose of 60 Gy (RBE) was split into 30 fractions of each 2 Gy (RBE). The planning target volumes ranged from approximately  $400 \text{ cm}^3$  to  $4200 \text{ cm}^3$ , the average volume was  $2105 \pm 1230 \text{ cm}^3$ . Most of the examined sarcomas had a lateral extension of about 9 cm, only the one in the arm had a lower extension of 2.5–3 cm. The length of the tumors varied between 23 cm and 36 cm, resulting in different lengths of overlapping regions and required matching fields. The overlapping regions varied therefore between 2 cm and 14 cm. Obviously, the longest tumor resulted in the shortest overlapping region, except for one very long tumor (36 cm) that was planned with two matching borders instead of one (P4). In total, the skin volumes in the treatment field ranged from  $70 \text{ cm}^3$  to  $300 \text{ cm}^3$ , assuming a thickness of 2 mm. Bones like humerus or femur were located close to or partly within the PTV in three cases and were covered by the PTV in the other two cases.

#### 4.2.2 Plan design

In the treatment plans, one beam direction was chosen (one horizontal beam with  $0^\circ$  couch inclination), namely one beam per subfield, while the beams of the different subfields had different isocenters in order to fulfill the matching strategy (cf. subsection 3.2.2). The energies ranged from 68.5 MeV to 219.1 MeV, depending on the lateral expansion of the tumor in beam direction. Considering this lateral expansion and respecting the given EL spacing restrictions, the resulting number of energy layers per beam was below 60 for all patients, except for P4, as it will be explained later in more detail. The spot weighting was limited from  $0.92 \cdot 10^6$  to  $95 \cdot 10^6$  NP/fx, which resulted – combined with spot and EL spacing – in a total number of spots between 12000 and 49000. An EL spacing of equal or lower than 3.3 MeV was achieved for all plans, except P4, where the distance between the lowest few energies was up to 4 MeV. In all plans the spot spacing limit of 0.5 cm was only exceeded for the lowest energies, which was considered to be acceptable. The plan details for all patients are shown in Table 4.1. For all PTVs that included a large skin volume – e.g. when the sarcoma spread over the whole thigh – it was very difficult and partly impossible to fulfill the skin goal of  $V_{60 \text{ Gy}} < 4 \text{ cm}^3$  while not compromising the target coverage.

Table 4.1: Plan details

	<b>P1</b>	<b>P2</b>	<b>P3</b>	<b>P4</b>	<b>P5</b>
PTV volume [ $cm^3$ ]	1622	2240	420	4221	2022
CTV volume [ $cm^3$ ]	1245.18	1874.67	295.73	n.a.	1642.48
CTV thickness (BEV) [cm]	9	9	2.5-3	9	8.3
Length of overlapping region[cm]	5.6	2.3	14	8.7/8	3.7
Min. E [MeV]	70.5	68.5	68.5	68.5	68.5
Max. E [MeV]	170.3	156.3	113.7	219.1	171.3
Number of EL per beam	53/53	44/43	42/42	66/62/59	63/60
EL spacing setting	const.* 0.32	const.* 0.32	auto* 1.1	const.* 0.45	auto* 1.2
EL spacing range	1.0 - 2.8	1.6 - 2.9	0.8 - 1.6	1.7 - 4.0	0.8 - 3.0
Spot spacing setting	auto* 0.5	auto* 0.4/0.39	auto* 0.45	auto* 0.55	auto* 0.5/0.4
Spot spacing range	0.45 - 0.85	0.38 - 0.69	0.41 - 0.84	0.34 - 0.91	0.40 - 0.87
No. of spots per beam	26911 / 16304	46036 / 35941	11858 / 14802	49306 / 39582 / 28848	29222 / 36679

\* Definition of constant and automatic EL and spot spacing in subsection 3.2.1

### 4.2.3 Plan analysis

The following analyses contain results of all treatment plans, while the PTVs with the smallest and largest overlap (P2 and P3), as well as the PTV planned with three irradiation fields (P4), were chosen as examples for demonstration.

#### Nominal plans

For all plans an acceptable CTV coverage was achieved. The skin sparing resulted in an avoidance of spots in the superficial part of the tumor and further in several low dose areas within the PTV, especially for long PTVs with a big skin involvement, as already remarked in subsection 4.2.2. The dose statistics confirmed these observations. Only for P3 the clinical goal of  $D_{98\%} > 95\%$  (57 Gy), representing the minimum dose, was fulfilled, whereas for the others the received dose was compromised resulting in  $D_{98\%} \sim 51$  Gy (corresponds to 85%). In contrast, the clinical goal of  $D_2\% < 107\%$ , representing the maximum dose, was fulfilled in all plans. The requirement of  $V_{95\%} > 95\%$  was only fulfilled for the PTVs of P2 and P3, while in the other cases the  $V_{95\%}$  was slightly lower with about 91.2% to 93.6%, see Table 4.2.

The target at the arm (P3), with one of the shortest extensions in longitudinal direction (23 cm CTV length, including the largest overlapping region with 14 cm), showed the best coverage, but it exceeded the clinical skin goal  $V_{60\text{Gy}} < 4\text{ cm}^3$  by approximately  $3\text{ cm}^3$ . For one of the thigh PTVs (P1) with a CTV length of 23 cm (overlap 5.6 cm) the  $V_{60\text{Gy}}$  at the skin was  $0.4\text{ cm}^3$ .  $D_{98\%}$  of the CTV was only 85.5% for P1 and P5 caused by the skin sparing and the challenging target location. Bones received 56 Gy to 61 Gy (RBE), which is partly higher than the clinical maximum dose of  $D_2\% < 64.2$  Gy (RBE) but it was accepted in order to not further compromise the target coverage.

The PTV planned with three beams (P4) was a special case. The PTV covered almost the whole thigh with a planning target volume of 4.2 liters, a CTV length of 36 cm and a lateral extension of 9 cm. The PTV was divided in three parts because of the limited field size. The lengths of the overlapping regions were about 8 cm. For two of the three beams the maximum EL number of 60 was exceeded by maximum 6 energy layers. Concerning the coverage,  $D_{98\%}$  was about 89% (53 Gy) and  $V_{95\%}$  was 93.3%.  $V_{60\text{Gy}}$  of the skin was exceeded by  $2.8\text{ cm}^3$ . One of the biggest challenges was to achieve a proper coverage of the femur region (high bone density) without getting hot and cold spots. Since the beam got partially blocked by bone, the dose in the femur was partially low, but never below 75% (45 Gy), as it can be seen in Figure 4.25.

#### Robustness analysis (RA)

For the robustness analysis the isocenters of the single PTV parts were shifted together and apart by 5 mm each, which resulted in 1 cm more and less overlap, respectively. The coverage dropped especially for the PTV parts that were shifted apart. In the following, the plans with isocenters shifted together and apart will be called RA+ and RA-, respectively.

Table 4.2: Dose statistics: dose values exceeding the acceptable tolerance for the CTV:  $D_{98\%} > 95\%$  (57 Gy),  $D_{2\%} < 107\%$  (64.2 Gy) and  $V_{95\%} > 95\%$ , and the skin:  $V_{60\text{Gy}} < 4\text{cm}^3$  are marked in red; Note: since for P4 two cases of each perturbed scenario exist, they are separated in a) / b) and c) / d) in the respective RA sections

		<b>P1</b>	<b>P2</b>	<b>P3</b>	<b>P4</b>	<b>P5</b>
<b>Nominal</b>						
CTV	$D_{98\%}$ [Gy]	51.3	56.4	58.6	n.a.	51.2
CTV	$D_{2\%}$ [Gy]	61.7	61.8	61.3	n.a.	62.1
CTV	$D_{50\%}$ [Gy]	60.2	60.1	60.1	n.a.	60.0
CTV	$V_{95\%}$ [%]	94.9	97.5	99.9	n.a.	94.5
PTV	$D_{98\%}$ [Gy]	50.2	55.5	57.3	53.3	51.1
PTV	$D_{2\%}$ [Gy]	61.7	61.8	61.4	61.8	62.1
PTV	$D_{50\%}$ [Gy]	60.0	60.0	60.0	60.0	60.0
PTV	$V_{95\%}$ [%]	91.3	96.4	98.3	93.3	93.6
Bones	$D_{2\%}$ [Gy]	60.4	56.5	59.7	61.3	61.0
Skin	$V_{60\text{Gy}}$ [ $\text{cm}^3$ ]	0.4	3.8	7.3	6.9	2.8
<b>RA+</b>						
CTV	$D_{98\%}$ [Gy]	52.5	52.2	59.3	n.a.	53.1
CTV	$D_{2\%}$ [Gy]	69.4	61.8	65.7	n.a.	71.4
CTV	$D_{50\%}$ [Gy]	60.2	60.0	62.6	n.a.	60.1
CTV	$V_{95\%}$ [%]	94.9	95.6	99.7	n.a.	73.2
PTV	$D_{98\%}$ [Gy]	48.7	50.8	55.7	0.4/0.4	51.5
PTV	$D_{2\%}$ [Gy]	69.4	61.8	66.0	107.7/109.0	71.5
PTV	$D_{50\%}$ [Gy]	60.0	60.0	62.1	60.0	60.0
PTV	$V_{95\%}$ [%]	88.9	93.6	96.7	60.7/65.8	73.2
Bones	$D_{2\%}$ [Gy]	67.3	57.6	63.6	107.4/106.9	67.9
Skin	$V_{60\text{Gy}}$ [ $\text{cm}^3$ ]	4.4	3.7	20.7	83.9/64.2	7.5
<b>RA-</b>						
CTV	$D_{98\%}$ [Gy]	47.6	46.6	54.8	n.a.	47.8
CTV	$D_{2\%}$ [Gy]	62.4	62.0	60.4	n.a.	62.2
CTV	$D_{50\%}$ [Gy]	60.2	60.0	57.4	n.a.	60.0
CTV	$V_{95\%}$ [%]	70.8	77.9	59.5	n.a.	95.7
PTV	$D_{98\%}$ [Gy]	47.3	46.4	53.4	5.6/2.6	47.7
PTV	$D_{2\%}$ [Gy]	62.4	62.0	60.7	94.7/75.1	62.2
PTV	$D_{50\%}$ [Gy]	60.0	60.0	57.6	60.0	60.0
PTV	$V_{95\%}$ [%]	70.7	77.8	61.6	52.6/52.5	93.0
Bones	$D_{2\%}$ [Gy]	60.5	57.0	59.3	95.3/75.3	61.0
Skin	$V_{60\text{Gy}}$ [ $\text{cm}^3$ ]	1.4	3.9	1.1	102.8/94.5	3.9

In case of the RA+ plans, the clinical goal of  $D_{98\%}$  for the PTV was not fulfilled by any of the plans, while the plan for P3 (with the largest overlap) was very close to the intended  $D_{98\%}$  with 55.7 Gy, as it can be seen in Table 4.2.  $V_{95\%}$  was only fulfilled by P3, whereas the good coverage was at the cost of a homogeneous dose distribution, resulting in hot spots with  $D_{2\%} > 107\%$  especially in the inferior and proximal region of the PTV. For the other PTVs (P1, P2, P5), the low dose regions appeared in similar sizes but with lower intensities by 16 % ( $D_{98\%} < 84\%$ ), comparing the RA+ plans with the nominal plans. However, the high dose regions were quite different. Two of them – P1 and P5 – showed  $D_{2\%} > 104\%$ , increasing up to 119 %, in the RA+ scenarios. Anyhow, these hot spots only appeared within the overlapping area and 1– 4 cm beyond. In contrast to that, the hot spots of up to 110 % for P3 (tumor in the arm) were distributed over the whole PTV. For P2 the hot spots did not exceed the 107 % limit when moving the isocenters together.

Regarding the RA- plans, the high dose regions in the overlapping area, that were observed for P1 and P5 for the RA+ scenarios, changed into low dose regions and the largest part of the dose was located at the superior and inferior tumor edges (up to 35 % more dose in comparison to the nominal plan for P5), as it can be seen in Figure 4.16. Also the plan for P2, which was robust against shifting the isocenters together (RA+), showed these under- and overdosage patterns in the RA- case. Moreover, the region covered by 98 % of the dose was larger at the edges, compared to the nominal plan. The most robust plan in the RA+ scenario, namely the plan for P3 with 14 cm length of the overlapping region, showed in the RA- case an extensive underdosage by 5 % to 10 % almost over the whole PTV, which might be caused by the isocenter shift not being perpendicular to the beam entrance directions (the surface was tilted and the lateral extension very small, so a shift of the isocenters apart and together was connected with a shift away and towards the surface of the tumor, respectively). Only the edges received more than 98 % dose.

Figure 4.17 shows the dose-volume histograms for P2. The nominal  $D_{98\%}$  dose statistic was just below the 95 % level (see Table 4.2), which is also apparent in the DVH in Figure 4.17 (yellow). Concerning the robust analysis, the coverage was similar to the nominal case for the RA+ plan (dark blue) but significantly less ( $V_{95\%} = 78\%$ ) for the RA- plan (orange). Regarding the skin treatment area of 2 mm thickness, the DVHs of the different plans were similar, only few percent of the volume received more than 60 Gy, and the skin goal was fulfilled for the nominal and the RA plans. The femur DVHs and the  $D_{2\%}$  values were almost identical, which led to the assumption that the dose distribution in the bone was not affected by the isocenter shifts. The line doses over the PTV length displayed similar dose distributions for the nominal and the RA+ plan, whereas the RA- plan showed an underdosage by more than 20 % in the overlapping region and a PTV coverage of only 78 %, as it can be seen in Figures 4.18, 4.19 and Table 4.2.

Concerning the arm sarcoma (P3), the DVH of the PTV displayed a good coverage in the nominal case (see Figure 4.20), which was confirmed by  $V_{95\%} = 98.3\%$ . The

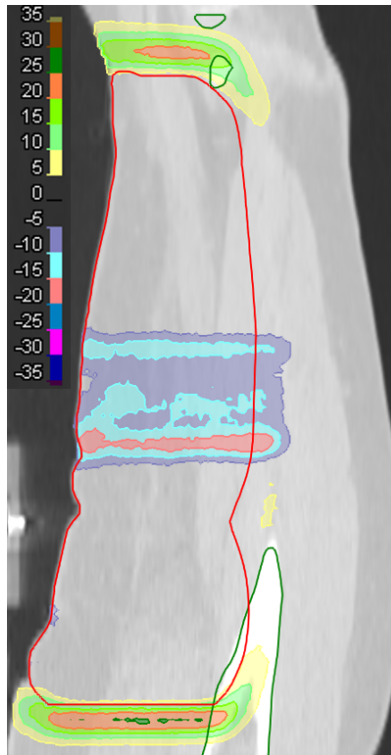


Figure 4.16: Dose difference map of nominal and RA- case for P5 (own illustration)

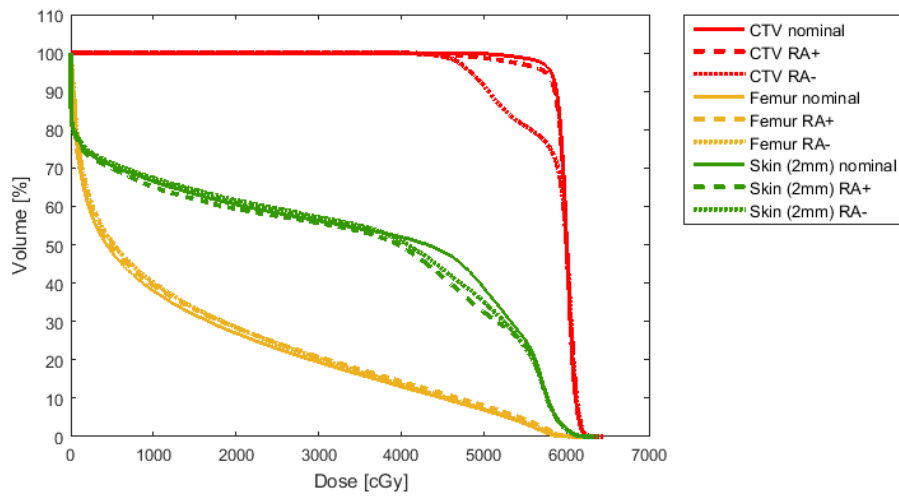


Figure 4.17: Dose-volume histograms of CTV, femur and 2 mm skin treatment area for P2 (own illustration)

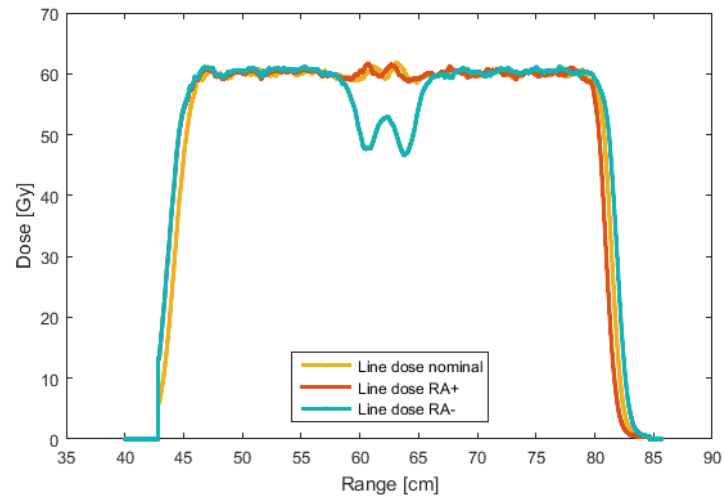


Figure 4.18: Line doses of nominal and RA cases for P2 (own illustration)

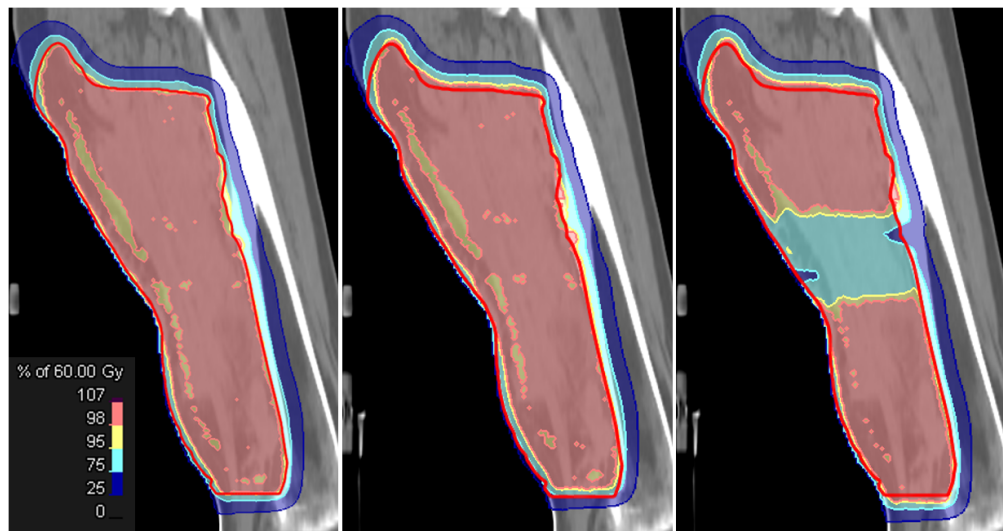


Figure 4.19: Dose distribution in nominal and RA plans of P2 (PTV delineation in red) (own illustration)

coverage was also good in the RA+ case ( $V_{95\%}=96.7\%$ ), but critical in the RA- case ( $V_{95\%}=61.6\%$ ). The dose statistics in Table 4.2 and the line doses in Figure 4.21 showed an overdosage by 10 % in the RA+ plan, and a broadly distributed underdosage by 11% in the RA- plan. According to the DVH, the skin treatment area received less dose in case of the RA- plan and a higher dose in case of the RA+ plan. This was again confirmed by the dose statistics in Table 4.2, where the skin goal was only fulfilled by the RA- plan and was exceeded by more than 400 % (about  $16\text{ cm}^3$ ) in the RA+ plan. The trend of the humerus DVH curves was similar for all three plans, while the closer PTV positions again caused an exceedance of the 60 Gy limit, which can be seen in the prolonged DVH and the dose statistics (Table 4.2).

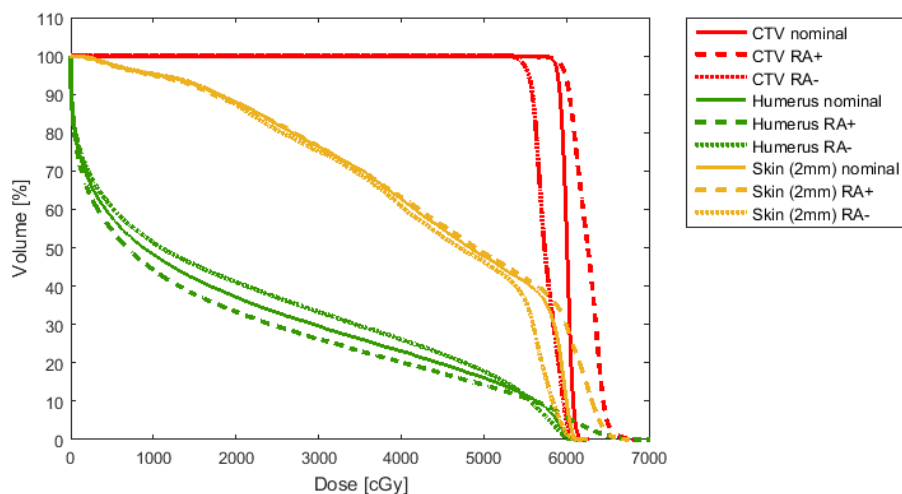


Figure 4.20: DVH for CTV, humerus and skin treatment area for nominal and RA cases of P3 (own illustration)

Regarding the PTV planned with three irradiation fields (see Fig. 4.23), four different shift possibilities were chosen for the three PTV parts: a) isocenter 1 shifted down and isocenters 2 and 3 shifted up, b) isocenters 1 and 2 shifted down and isocenter 3 shifted up, c) isocenter 1 shifted up and other isocenters shifted down and d) isocenters 1 and 2 shifted up and isocenter 3 shifted down. All possibilities showed significant differences, as it can be seen in Figure 4.25. In case a) the upper and middle region received up to 40 % more dose, the lower region was more underdosed and only continuously covered by the 10 % isodose. The femur received in the nominal plan about 92 % to 100 % of the dose, whereas in case a) it received up to 180 % (108 Gy). In case b) the high dose region was located in the middle to lower part of the PTV. The coverage of the upper part was quite good – mostly 98 % with some small parts of 95 % –, but the uppermost and undermost 2 cm received less than 5 %. The femur showed the same trend as before in case a) with an up to 190 % higher dose (112 Gy). Case c) showed a high overdosage of up to 150 % at the upper and lower part, ranging several centimeters beyond the PTV borders. The dose in the center region was only about 20 % and in

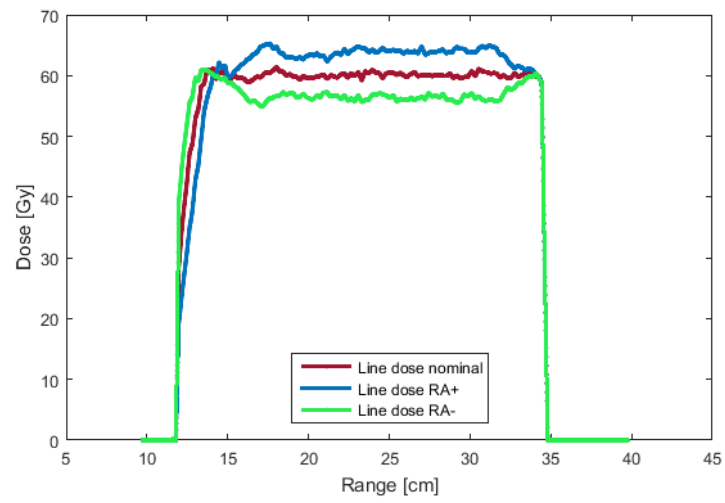


Figure 4.21: Line doses of nominal and RA cases for P3 (own illustration)

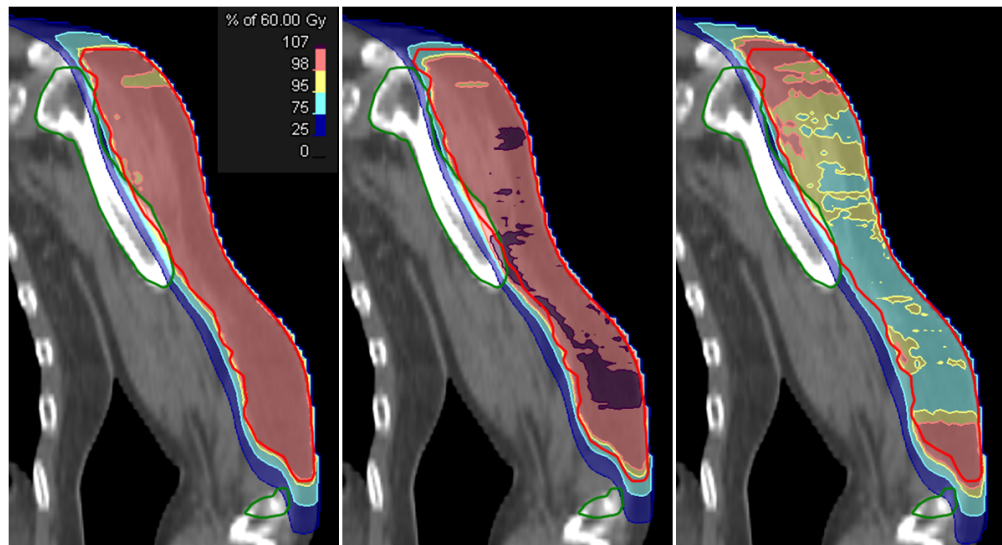


Figure 4.22: Dose distribution in nominal and RA plans of P3 (PTV delineation in red, humerus delineation in green) (own illustration)

the femur even partly just 2%, which equals less than 2 Gy. Case d) was similar to c), with only 1.22% to 20% dose in the middle part of the PTV. The overdosage at and beyond the edges amounted to 120% (about 70 Gy) on average. The dose in the femur varied from far above 107% to lower than 5%, as the DVH curves in Figure A.3 show. Further dose-volume histograms can be found in the Appendix. Regarding the nerves and vessels, the goals of maximum 70 Gy to 0.1 cm<sup>3</sup> of their volume were fulfilled only in the nominal plan, and highly exceeded in the RA plans with up to 155% of the 70 Gy limit. Concerning the skin, an increase of the PTV dose of course also entails an increase of the skin dose, as Table 4.2 shows. As the line doses in Figure 4.27 of the different cases show, a systematic evaluation of the perturbed scenarios was not possible.



Figure 4.23: Schematic illustration of PTV sections for P4, consisting of superior section (orange), middle section (blue) and inferior section (green) with respective isocenters and overlapping regions (striped); (own illustration)



Figure 4.24: Dose distribution in nominal plan of P4 (PTV delineation in red, femur delineation in green); (own illustration)

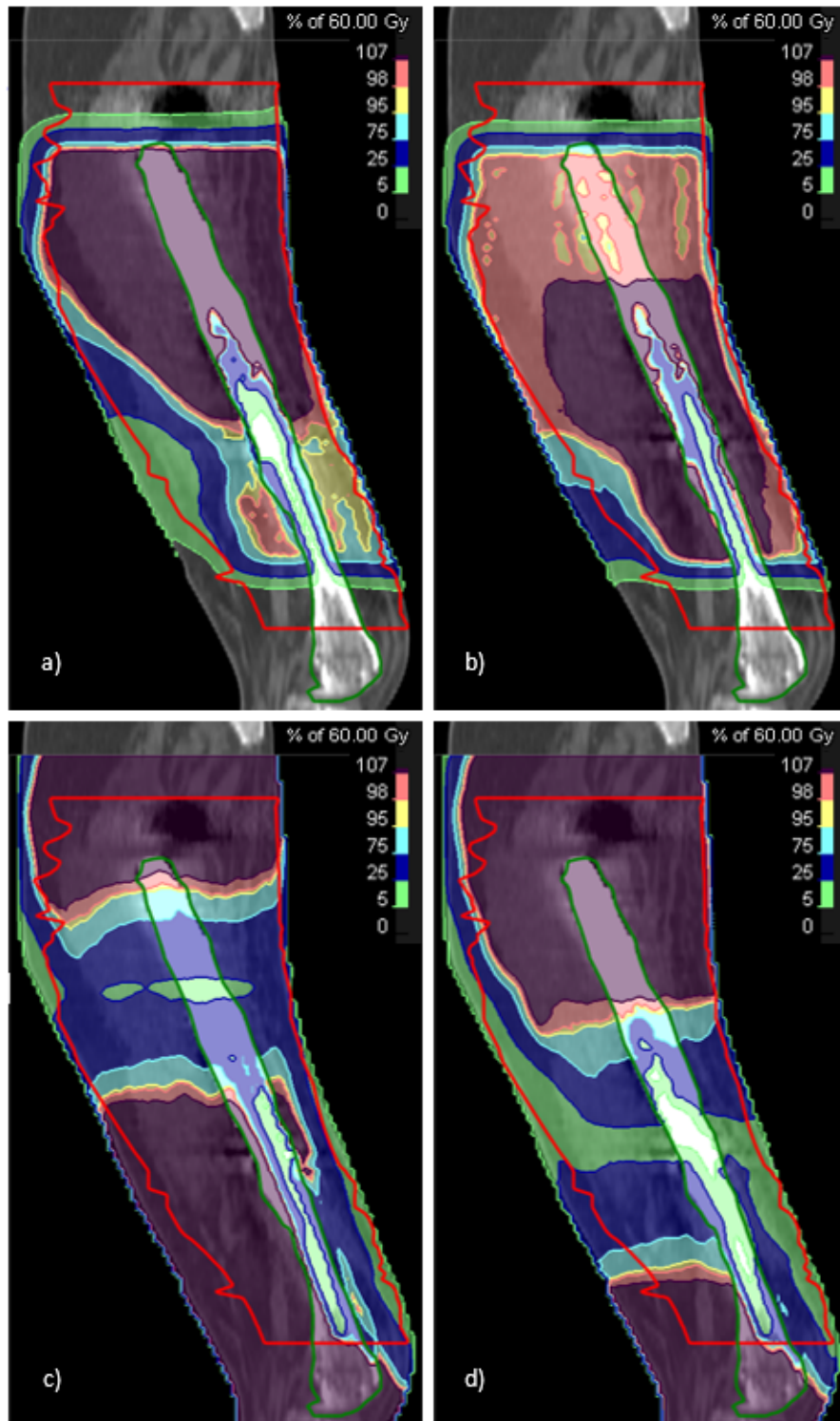


Figure 4.25: Dose distributions of cases a, b, c and d of the robust analysis for P4 (own illustration)

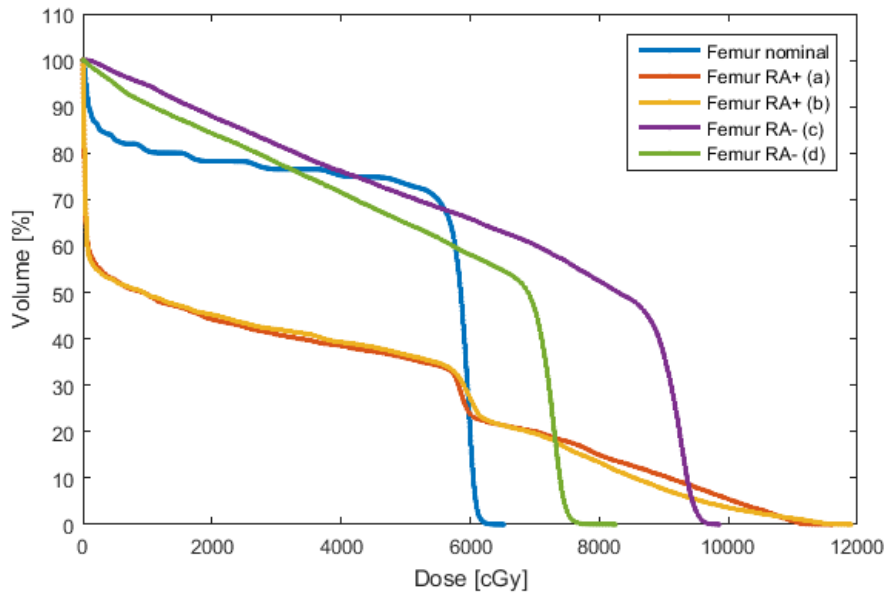


Figure 4.26: DVH of the femur of P4 for nominal and RA cases (own illustration)

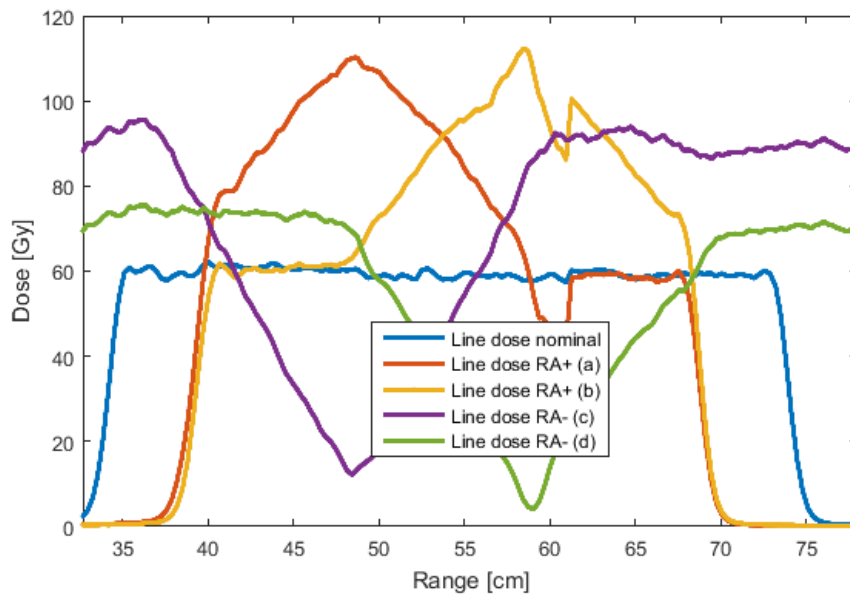


Figure 4.27: Line doses of P4 for nominal and RA cases (own illustration)



# 5 Discussion

## 5.1 Surface dose measurements

For the comparison of the results it was tried to consider all possible influences in the measurements. Therefore the impact of the range shifter in the beam line was investigated and calibration corrections for the films were established. The build-up characterization was used for the establishment of a simple model, which is able to predict the build-up within certain limits (see subsection 5.1.3). The tilted surface was the second step after the straight surface, approximating the real patient's geometry. It resulted in some challenges (see subsection 5.1.4) which need to be investigated in future works. A step towards clinical applications was done with the SOBP measurements (see subsection 5.1.5), which need further investigations as well.

### 5.1.1 Preliminary investigations

In order to setup the measurements as close as possible to the clinical reality it was decided to reduce the SSD when measuring with range shifter. This reduces spot widening and scattering, as it was described by Schaffner (Schaffner 2008) and Titt et al. (Titt et al. 2010). The position change brought along some challenges and inconsistency in the evaluation, as the smaller SSD resulted in an average dose increase by 25 %. The different SSD has to be considered during the measurement setup as well as in the treatment plan. However, the magnitude of the dose difference depends on the spot characteristics as well as the beam geometry. In order to facilitate the comparison of the measurement in different setup geometries all dosimetric values were normalized to the reliable Markus chamber dose at a defined depth.

Film calibration is well known to be a challenging procedure. The reliability and applicability strongly depends on the preparation of the measurements, the quality of the film batch, the stability of the devices used for evaluation etc. In the case of the presented film measurements (cf. section 4.1) the correction of the film measurements was necessary (cf. subsections 3.1.4 and 4.1.1). The established correction method worked well for all measurements where it was used, independent of the applied energy and the day of the measurement. Another approach that was tested and rejected was the establishment of a correction factor from reference measurements. Observing similar issues in film calibration variability, some ion beam centers follow the approach of calibrating each film sheet on the day of measurements.

### 5.1.2 Influence of the range shifter on film and Markus chamber doses

To reduce the depth of dose deposition, namely the energy in a reference depth, either range shifters which are incorporated in the nozzle, or boli which are positioned on the patients or phantoms surface can be used. A bolus is frequently used in conventional radiation therapy, but it can also be used for preserving the spot size of scanned proton beams in order to spare OARs (cf. Both et al. 2014) or for energy degradation instead of a range shifter when a close positioning of the range shifter to the patient is not possible (cf. Shen et al. 2015). A range shifter widens the spot size depending on the range shifter material and thickness, which is why a lower distance from range shifter to the patient's surface or a different range shifter design might be beneficial (cf. Schaffner 2008, Shen et al. 2015).

The aim of the performed measurements was to investigate the influence of the range shifter on the dosimetric behavior of films and Markus chamber, despite the reduction of the nominal energy at the reference measurement depth. In particular, it was investigated if the production of secondary particles in range shifter has an influence on the dosimetric performance of films.

Considering only Markus chamber values acquired with 97.4 MeV, the range shifter influence could be quantified as a small dose augmentation of approximately 7.4 % for a dose level of 2 Gy. However, at 179.2 MeV, acquired nominally and from 195.2 MeV with range shifter, respectively, the measurement results agreed almost perfectly within 8 % deviation. From the observed findings (cf. subsection 4.1.2) it can be concluded that the range shifter only changes the energy at the reference depth and therefore the particle range but has no further influence on dosimetric characteristics of films and Markus chamber and further on the build-up shape.

### 5.1.3 Build-up characterization

The purpose of this part was to characterize the dose build-up of scanned proton beams within the first 2 mm, namely to determine how the superficial build-up depends on the energy, the dose level and the surface character, and how it can be predicted.

In the measurements, the initial gradient between 0  $\mu\text{m}$  and 360  $\mu\text{m}$  depth increased for increasing energy, which was confirmed by the simulations of Kelleter where the contribution of secondary particles was found to be higher compared to primary protons when a higher energy was applied (cf. Kelleter 2017). According to Pfuhl, especially electrons are responsible for the superficial build-up effect within the first few millimeters, whereas this effect overlaps with the target fragment build-up effect, which occurs within the first 8 cm and is mainly caused by secondary protons originating from nuclear interactions (cf. Pfuhl et al. 2018).

Assuming a linear relation for the build-up dose between 0  $\mu\text{m}$  and 360  $\mu\text{m}$ , the fit of the gradient revealed a logarithmic dependency on the energy. A logarithmic fit for the further progression of the depth-dose curve was used since it mimics the plateau that might be reached in higher depths. However, concerning the plateau, there is no clear

definition in literature what can be called “plateau” in this superficial region and when it is reached. In this work the plateau was defined as not deviating more than 0.08 % in dose within a range of 100  $\mu\text{m}$ .

The equations for the build-up within 0  $\mu\text{m}$  and 360  $\mu\text{m}$  and for the dose in higher depths up to 2000  $\mu\text{m}$  can be used for estimation of depth-dose progressions for any arbitrary energy from 60 to about 250 MeV. Certainly, more measurement points would be necessary to validate and optimize these relationships, and adaptations would have to be established when the dose development in higher depths should be modelled. However, the current model is very simple, consisting of only two curves, developed from measurements at only three energies and a dose level of 2 Gy. It will not be suitable for other dose levels. Anyhow, accurate depth-dose curves can be determined exclusively with precisely calibrated measurement devices as ionization chambers, and by means of extensive simulations.

#### 5.1.4 Tilted surface

As part of a previous project, film measurements on a patient-like geometry, namely an anthropomorphic phantom, were performed. A superficial tumor on the upper arm was delineated according to a clinical example, a treatment plan was created and the resulting SOPB was delivered on the phantom. In order to determine the dose at the surface film stripes were fixed on the arm’s surface. Two sets of films were irradiated, once with a pencil beam optimized plan, the other one with a Monte Carlo optimized plan. The results were extremely poor, yielding deviations between the calculated and the measured dose of about 30 %. Since measurements of films and Markus chamber at a straight surface showed much better conformity, it was decided to take a few steps back and look into detail of the build-up region on straight and tilted surfaces. As summarized in 5.1.3, at first plane and upright surfaces were irradiated, followed by tilted surfaces.

The comparison of straight and tilted surface at 97.4 MeV showed a good agreement considering only the depth-dose trend of the Markus chamber values, as it was already noted in subsection 4.1.4. The dose difference of 8.6 % on average might be caused by the inclination.

While the film part further away from the nozzle agreed well with the Markus chamber values the part with the closer distance, starting at the center of the film and spreading over the whole film half, showed a severe dose loss of up to 31.5 %. To the author’s knowledge no study about the usage of radiochromic films with scanned protons on tilted surfaces exists. However, also the straight films showed a small dose loss at the lateral edges.

The build-up analysis of the tilted film parts that showed a homogeneous dose distribution when irradiated on a tilted surface agreed well with the measurement at the straight surface when dose values were scaled to the respective initial Markus chamber value (cf. subsection 4.1.4).

Simulations with Gate (v8.0)/Geant4.10.03.p1 were performed at the Medical University of Vienna in order to reproduce the effect and determine the origin of the severe

dose loss. The measured lateral dose profiles on tilted and non-tilted surfaces could not be reproduced by the same extent as observed in the measurements (see Figures 5.1 and 5.2). Nevertheless, the choice of the field size as well as the tilting degree caused a non-negligible effect. The comparison of a  $4\text{ cm} \times 4\text{ cm}$  field (Figure 5.3) and a  $7\text{ cm} \times 7\text{ cm}$  field (Figure 5.4), which was used in the measurements, shows that the dose loss at the film edges is less in the larger than in the smaller irradiation field. This can be easily explained by the scattering of primary protons and secondary particles from all directions, which partly contribute to the dose and assure a homogeneous field. At the edges of an irradiation field a different amount of particles is scattered away than the number of particles scattered into the field. Therefore no homogeneous field can be achieved (cf. Newhauser and Zhang 2015). Consequently, a  $4\text{ cm} \times 4\text{ cm}$  irradiation field applied on a  $4\text{ cm} \times 4\text{ cm}$  sized film would result in an inhomogeneous field and thus in a dose loss at the film edges. Dahle et al. also observed an asymmetric dose loss at the film edges for a straight setup but explained it with a possible bending of the films (cf. Dahle et al. 2017). However, also the degree of inclination affects the amount of dose deposition on the edges, as it can be further seen in Figure 5.4.

The larger the inclination, the higher the applied dose and the lower the dose drop at the edges. This can be explained as follows: due to the inclination the ratio of irradiated film size and irradiation field is lower (see Fig. 3.2b), which resulted in less inhomogeneity at the film edges. It was also observed in Figure 5.4 that the dose decrease on the film part closer to the nozzle became larger with increasing angle. Both most important dose contributions, namely from electrons and primary protons, showed this effect.

Regarding only the simulations, it could be concluded that a dose loss at the edges of a film can either be caused by a too small irradiation field or by an inclination of the surface. Anyhow, both effects could not be confirmed by the present measurements.

Consequently, the reason for the dose loss with inclination could not be clarified in the frame of this thesis and needs further investigations.

### 5.1.5 SOBP measurements

The measurement values acquired within the SOBP that was irradiated on a straight surface fitted well in the build-up behavior of the used single energy layers (cf. subsection 4.1.5). However, the dose within the SOBP was only determined at five points using films and Markus chamber. Therefore it would be interesting to repeat the SOBP measurements with more films in order to investigate the SOBP build-up shape in more detail.

Concerning the applicability of the established model for depth-dose progression on a SOBP, the results are quite promising. The deviation of the model from the measured values from the Markus chamber was less than 1%. However, the model is only based on single energy layer measurements and was not validated to predict the build-up shape in a SOBP.

Regarding the tilted films, the SOBP measurements could neither confirm nor refute the previous observations of the inhomogeneous dose distribution on the films (cf. sub-

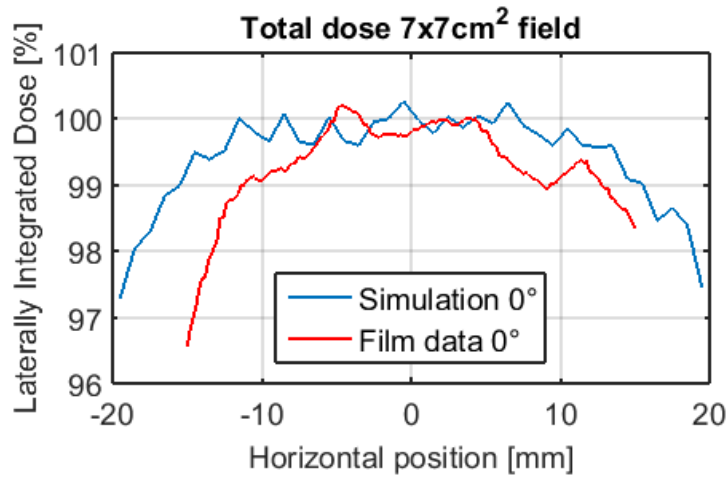


Figure 5.1: Comparison of simulation and film measurements at a straight surface (note: the curves are shown mirrored along the x-axis) (own illustration)

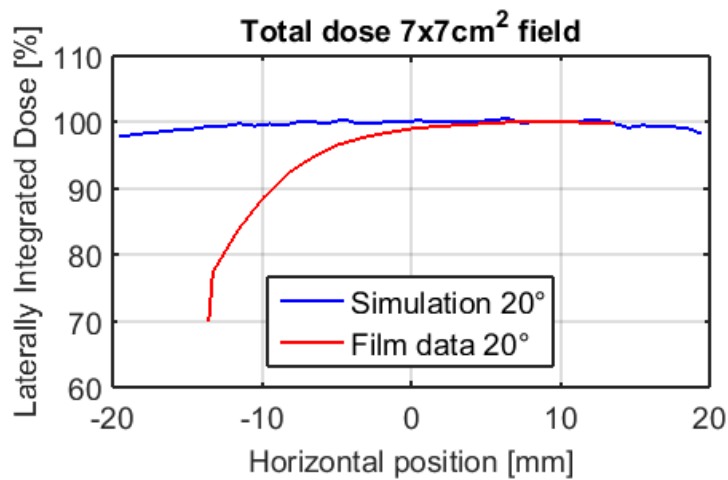


Figure 5.2: Comparison of simulation and film measurements at a 20° tilted surface (note: the curves are shown mirrored along the x-axis, compared to the results shown in Fig. 4.11) (own illustration)

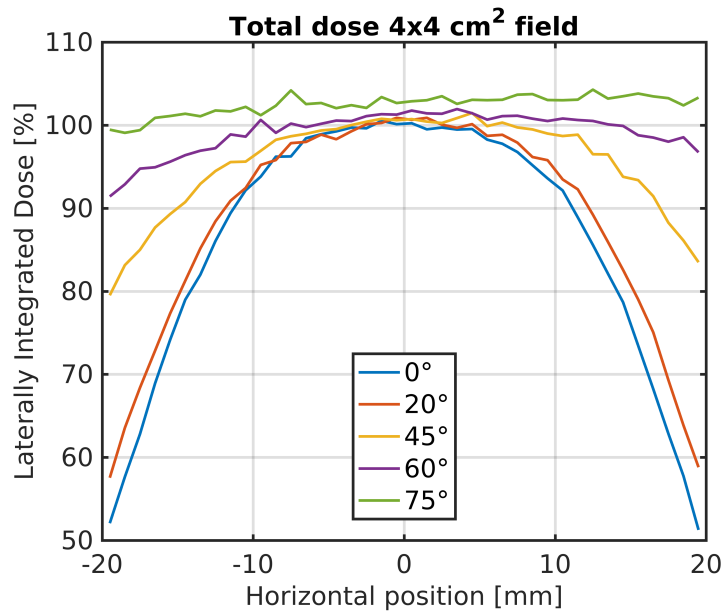


Figure 5.3: Result of Monte Carlo simulation on 4 cm × 4 cm field for different angles (own illustration)

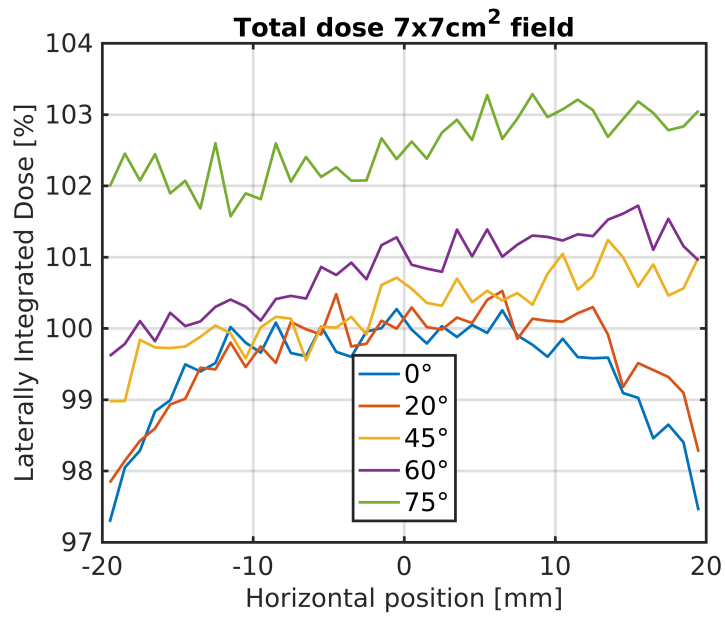


Figure 5.4: Result of Monte Carlo simulation on 7 cm × 7 cm field for different angles (own illustration)

section 4.1.4). First of all only one film value per depth was measured, which doesn't provide good statistics and impedes a qualitative statement. However, the doses did not indicate a dose loss similar to the tilted films irradiated at a single energy even when accounting for the uncertainties of the film dosimetry.

### **5.1.6 Film and Markus chamber measurements at low dose levels**

The lower dose levels confirmed the conclusions of subsections 5.1.2 and 5.1.3, that the range shifter only changes energy and range, and that the initial dose increase within the superficial  $360\ \mu\text{m}$  is higher with higher energies, whereas the build-up shape between  $360\ \mu\text{m}$  and  $2000\ \mu\text{m}$  is comparable for all energies.

### **5.1.7 Outlook**

The build-up characterization showed interesting results, calling for further investigations of the delta electron build-up and the target fragmentation build-up, including measurements in larger depths and simulations of the initial build-up behavior. This should also be investigated for SOBPs.

For the established build-up model in this thesis measurements at three energies were used. It would be interesting if a more sophisticated model could be created, using more energies and possibly also more dose levels.

Concerning the tilted surfaces it would be necessary to identify the origin of the dose drop with more measurements. Subsequent investigational steps, approximating the patient's surface, would then be symmetric curved surfaces and again the asymmetrically shaped anthropomorphic arm.

## **5.2 Treatment planning**

The purpose of the treatment planning part in the scope of this thesis was to analyze if the matching technique for larger tumors is robust enough to cope with setup or movement uncertainties. Especially the length of the overlapping region was thoroughly investigated with respect to any restrictions.

Five large extremity sarcomas were chosen for this investigation of robustness, which was performed by comparisons of coverage criteria, clinical goals, dose-volume histograms and line doses. Four of the five sarcomas were located in the thigh, one in the upper arm. This might be of importance, since the arm has less volume than the thigh, and therefore also the sarcoma in the arm was thinner, but not shorter, so it still required field matching. For the robustness analysis a shift of 5 mm was assumed, which of course represented an extreme case. Anyhow, mispositioning or movement uncertainties can easily be in the range of 2–3 mm for patients suffering from such big tumors.

In the course of the analysis it emerged that, in case of very large tumors with a big skin involvement, the attempt of skin dose reduction seems to always entail target coverage loss. Its magnitude depended on the ratio of skin to target volume. Target

coverage was further compromised by tissue inhomogeneities or due to bones etc. Even in the nominal plans it was partly difficult to achieve a good coverage of target and bone, and to reduce hot spots in the skin treatment area.

Regarding the two most robust plans, namely P2 and P3, the shift apart caused more severe problems than the shift together, concerning coverage, low dose areas, hot spots and sparing of OARs and other tissue outside the PTV. When the nominal plan had an insufficient PTV coverage, as it was for example the case for P1 and P5, it was even worse in the shifted plans. Besides skin overdosage in the RA+ cases, the dose outside the PTV increased in the RA- cases. In return, the overlapping region of the PTV received maximum doses of up to 119 % in RA+ cases and minimal doses of approximately 75 % in RA- cases. The bones that were located only close to or partly inside the PTV were not much affected by the shifts. Instead, bones that were almost completely surrounded by the PTV were insufficiently covered and showed partly high overdosage in the shifted scenarios.

In case of the very large sarcoma that was planned with three irradiation fields, both RA+ and RA- plans showed large overdosage and underdosage areas. While the edges received hardly any dose in the together shifted cases, more than 100 Gy were reached in the RA- cases for a large part ranging from the upper and lower third of the PTV, respectively, far beyond the PTV edges. Moreover, skin, nerves and vessels received too high doses in all shifted cases. It can be concluded that the application of more than two parallel irradiation fields on very large volumes greatly increases the risk of severe dose inhomogeneities, induced by positioning uncertainties or patient movement. In contrast, Zurlo et al. found that a higher number of noncoplanar (!) fields of intensity modulated photons or protons applied on large tumors is advantageous concerning dose homogeneity and compliance of OAR constraints (cf. Zurlo et al. 2000).

As the robustness analyses showed, tissue inhomogeneities (bones, muscles) might increase the risk of unintended under- or overdosage and impede plan robustness. Generally, the more homogeneous the dose distribution in a plan, the better the robustness against uncertainties. It emerged, that a variation of the tumor size due to patient movement (stretching, contracting, bending) can strongly influence OAR and healthy tissue sparing. Furthermore, the higher the skin to target volume ratio, the higher is the risk of skin reactions. Apart from the insufficient skin sparing, the coverage quality does not necessarily depend on the length of the overlapping region, as P2 (2.3 cm overlapping length) and P3 (14 cm overlapping length) showed. However, Knäusl et al. analyzed different lengths of the overlapping region and found significant improvements of robustness when choosing an overlapping length as large as possible (cf. Knäusl et al. 2016).

The combination of surgery and radiotherapy is a well-established procedure and many studies discuss the advantages and disadvantages of preoperative and postoperative radiotherapy with photons, neutrons or ions (Hoefkens et al. 2016, Jansen et al. 2014, Suit and Spiro 1994, Schmitt et al. 1983). Especially for extremity sarcoma preoperative radiotherapy seems to be in favor in order to avoid the complications caused by the side effects of the surgery (Jansen et al. 2014). Anyhow, independent of the used radiation

type, radiation-induced malignancies are possible after treatment. Concerning bones, several studies about radiation-induced fractures exist (Dickie et al. 2009, Livi et al. 2006, Holt et al. 2005, Helmstedter et al. 2001, Lin et al. 1998). Dickie et al. evaluated bone fracture and non-fracture incidence in sarcoma patients treated by external beam therapy and linked them to irradiated bone volume and length. They observed a 10 % higher occurrence of fractures in the upper leg, compared to the lower leg. Furthermore, they found a limit of maximum 64 % of the bone volume being exposed to 40 Gy ( $V_{40\text{Gy}} < 64\%$ ), a mean dose of maximum 37 Gy ( $D_{\text{mean}} < 37\text{Gy}$ ) and a maximum dose of 59 Gy ( $D_{2\%} < 59\text{Gy}$ ) in order to reduce the risk of radiation-induced fracture. In addition, a larger length of irradiated bone increased the risk. Concerning these limits in the current case, only P2, the thigh sarcoma with the most homogeneous and robust plan, would have a low risk of a radiation-induced fracture, whereas the extreme case P4 would have a very high probability, since in both nominal and perturbed cases almost all limits are significantly exceeded. Regarding the skin, the risk of severe complications during and after treatment increases when the irradiated volumes approach their clinically acceptable limit of  $V_{60\text{Gy}} < 4\text{cm}^3$  (cf. Yanagi et al. 2009). This is an important issue, especially when irradiating postoperatively, since tumor cells might potentially be located in the superficial region of the surgical wound. However, a compromise between target coverage and skin sparing has to be found in cases of PTVs with large skin parts. As it was published by Lee et al., the volume of skin receiving high doses can be reduced significantly by contouring the skin as a sensitive structure and considering it during dose optimization (cf. Lee et al. 2002), as it was also done in the scope of this thesis.



# Bibliography

- Ashland (s.a.). *GAFChromic EBT3 film specifications*. Ashland Inc.
- Bilge, H. et al. (2008). "Surface dose measurements with GafChromic EBT film for 6 and 18 MV photon beams". In: *Physica Med.* 25.
- Both, S. et al. (2014). "Development and Clinical Implementation of a Universal Bolus to Maintain Spot Size During Delivery of Base of Skull Pencil Beam Scanning Proton Therapy". In: *International Journal of Radiation Oncology, Biology and Physics* 90.1, pp. 79–84.
- Chiu-Tsao, S.-T. and Chan, M. F. (2009). "Photon beam dosimetry in the superficial buildup region using radiochromic EBT film stack". In: *Med. Phys.* 36.6, pp. 2074–83.
- Chung, H. et al. (2005). "Evaluation of surface and build-up region dose for intensity-modulated radiation therapy in head and neck cancer". In: *Med. Phys.* 32.8, pp. 2682–89.
- CIRS (2013). *ATOM Dosimetry Phantoms*. Computerized Imaging Reference Systems Inc.
- Creative Commons (2010). *Dose Depth Curves*. Creative Commons. URL: [https://commons.wikimedia.org/wiki/File:Dose\\_Depth\\_Curves.svg](https://commons.wikimedia.org/wiki/File:Dose_Depth_Curves.svg).
- Dahle, T. et al. (2017). "Monte Carlo simulations of a low energy proton beamline for radiobiological experiments". In: *Acta Oncologica* 56.6, pp. 779–786.
- Dance, D. et al., eds. (2014). *Diagnostic Radiology Physics: A Handbook for Teachers and Students*. International Atomic Energy Agency (IAEA).
- DEGRO (2015). *Supportive Maßnahmen in der Radioonkologie*. 1.2. Deutsche Gesellschaft für Radioonkologie (DEGRO). URL: <https://www.degro.org/ueber-uns/veroeffentlichungen/leitlinien/>.
- Devic, S. et al. (2006). "Accurate skin dose measurements using radiochromic film in clinical applications". In: *Med. Phys.* 33.4, pp. 1116–24.
- Devic, S. et al. (2005). "Precise radiochromic film dosimetry using a flat-bed document scanner". In: *Med. Phys.* 32.7, pp. 2245–53.
- Devic, S. et al. (2016). "Reference radiochromic film dosimetry: Review of technical aspects". In: *Physica Medica* 32, pp. 541–556.
- Dickie, C. et al. (2009). "Bone fractures following external beam radiotherapy and limb-preservation surgery for lower extremity soft tissue sarcoma: relationship to irradiated bone length, volume, tumor location and dose". In: *Int. J. Radiation Oncology Biol. Phys.* 75.4, pp. 1119–1124.
- Dreindl, R. et al., eds. (2017). *SOP: Use of film dosimetry system*. MedAustron.
- Drägerwerk AG & Co. KGaA (2009). *Protonentherapie - eine neue Chance bei Krebs. Prozessunterstützung durch Anästhesieverfahren*. White paper.

- Durante, M. and Paganetti, H. (2016). “Nuclear physics in particle therapy: a review”. In: *Reports on Progress in Physics* 79.
- Epson (s.a.). *Expression 11000XL - datasheet*. Seiko Epson Corporation.
- Fredriksson, A. et al. (2011). “Minimax optimization for handling range and setup uncertainties in proton therapy”. In: *Med. Phys.* 38.3. Copyright: American Association of Physicists in Medicine, pp. 1672–1684.
- Fuchs, H. (2018). *Dose Calculation*. Basic Seminar: Medical Physics VIII - Physical Fundamentals of Radio Oncology, Medical University of Vienna.
- Fujimoto, R. et al. (2011). “GPU-based fast pencil beam algorithm for proton therapy”. In: *Phys. Med. Biol.* 56, pp. 1319–1328.
- Georg, D. (2018). *Medical Linear Accelerators*. Basic Seminar: Medical Physics VIII - Physical Fundamentals of Radio Oncology, Medical University of Vienna.
- Gerward, L. (1999). “Paul Villard and his Discovery of Gamma Rays”. In: *Physics in Perspective* 1, pp. 367–383.
- Goitein, M. et al. (2002). “Treating cancer with protons”. In: *Physics Today* 55.9. Copyright: American Institute of Physics, pp. 45–50.
- Helmstedter, C. et al. (2001). “Pathologic Fractures After Surgery and Radiation for Soft Tissue Tumors”. In: *Clinical Orthopaedics and Related Research* 389, pp. 165–172.
- Hoefkens, F. et al. (2016). “Soft tissue sarcoma of the extremities: pending questions on surgery and radiotherapy”. In: *Radiation Oncology* 11.
- Holt, G. et al. (2005). “Fractures following radiotherapy and limb-salvage surgery for lower extremity soft-tissue sarcomas”. In: *The Journal of Bone and Joint Surgery* 87-A.2, pp. 315–319.
- ICRU (1999). “ICRU Report 62: Prescribing, Recording and Reporting Photon Beam Therapy (Supplement to ICRU Report 50)”. In: *Journal of the ICRU*.
- (2007). “ICRU Report 78: Prescribing, Recording, and Reporting Proton-Beam Therapy”. In: *Journal of the ICRU* 7.2.
- Jansen, N. et al. (2014). “La radiothérapie moderne pré- ou postopératoire pour les sarcomes des tissus mous des membres”. In: *Rev. Med. Liège* 69, pp. 53–57.
- Kelleter, L. (2017). *Dose Build-up effect and Secondary Particles in Proton Therapy*. University College London (UCL). URL: <http://www.hep.ucl.ac.uk/pbt/wikiData/presentations/2017>.
- Khachonkham, S. et al. (2017). “Characteristics of EBT-XD and EBT3 radiochromic film dosimetry for photon and proton beams”. submitted to *Phys. Med. Biol.*
- Knäusl, B. et al. (2016). *Treatment of extremity soft tissue sarcoma using protons - robustness of single and matched fields*. ESTRO.
- Knutson, N. C. (2012). “Evaluation of a proton pencil beam algorithm for dose calculations in heterogeneous media”. MA thesis. Louisiana State University. URL: [https://digitalcommons.lsu.edu/cgi/viewcontent.cgi?article=4978&context=gradschool\\_theses](https://digitalcommons.lsu.edu/cgi/viewcontent.cgi?article=4978&context=gradschool_theses).
- Krieger, H. (1998). *Strahlenphysik, Dosimetrie und Strahlenschutz*. 4th ed. Vol. 1. Springer Fachmedien Wiesbaden.
- (2011). *Strahlungsmessung und Dosimetrie*. 1st ed. Vieweg + Teubner Verlag, Springer Fachmedien Wiesbaden GmbH.

- Lechner, W. (2018). *Dosimetry*. Basic Seminar: Medical Physics VIII - Physical Fundamentals of Radio Oncology, Medical University of Vienna.
- Lee, N. et al. (2002). "Skin toxicity due to intensity-modulated radiotherapy for head-and-neck carcinoma". In: *Int. J. Radiation Oncology Biol. Phys.* 53.3, pp. 630–637.
- Lin, P. et al. (1998). "Treatment of Femoral Fractures After Irradiation". In: *Clinical Orthopaedics and Related Research* 352, pp. 168–178.
- Linz, U., ed. (2012). *Ion Beam Therapy - Fundamentals, Technology, Clinical Applications*. 1st ed. Biological and Medical Physics, Biomedical Engineering. Springer, Berlin, Heidelberg.
- Livi, L. et al. (2006). "Late treatment-related complications in 214 patients with extremity soft-tissue sarcoma treated by surgery and postoperative radiation therapy". In: *The American Journal of Surgery* 191, pp. 230–234.
- Lomax, A. (2016). "Particle Radiotherapy". In: ed. by A. Rath and N. Sahoo. Springer, New Delhi. Chap. SFUD, IMPT, and Plan Robustness, pp. 169–194.
- Luks, S. and Stillger, M. (s.a.). *Strahlentherapie: Häufige Fragen*. Gemeinschaftspraxis für Strahlentherapie Dr. (Univ. Zagreb) Luks, Dr. med. Stillger. URL: <http://www.strahlentherapie-do.de/faq.html>.
- Lynn J. Verhey, P. L. P. (2010). "Leibel and Phillips Textbook of Radiation Oncology". In: ed. by R. Hoppe et al. 3rd ed. Saunders. Chap. Principles of Radiation Physics.
- MedAustron (2017). *Homepage MedAustron*. MedAustron. URL: <https://www.medaustron.at/>.
- Meroli, S. (s.a.). *The interaction of photons with the matter*. CERN. URL: [http://meroli.web.cern.ch/Lecture\\_photon\\_interaction.html](http://meroli.web.cern.ch/Lecture_photon_interaction.html).
- Nakano, M. et al. (2012). "A study of surface dosimetry for breast cancer radiotherapy treatments using Gafchromic EBT2 film". In: *J Appl Clin Med Phys* 13.3, pp. 83–97.
- Nesvacil, N. and Kirisits, C. (2018). *Physical Fundamentals of Radio Oncology: Brachytherapy*. Basic Seminar: Medical Physics VIII - Physical Fundamentals of Radio Oncology, Medical University of Vienna.
- Newhauser, W. D. and Zhang, R. (2015). "The physics of proton therapy". In: *Phys. Med. Biol.* 60.
- Nucletron (s.a.). *Patientenratgeber: Brachytherapie*. Vincentius-Kliniken. URL: [http://www.vincentius-kliniken.de/uploads/media/Patientenratgeber\\_Brachy\\_General.pdf](http://www.vincentius-kliniken.de/uploads/media/Patientenratgeber_Brachy_General.pdf).
- Paganetti, H. (2009). "Comparing pencil-beam generated and Monte Carlo generated dose-to-water and dose-to-tissue distributions for proton therapy patients". In: *World Congress on Medical Physics and Biomedical Engineering, September 7 - 12, 2009, Munich, Germany*. Ed. by O. Dössel and W. Schlegel. Vol. 25. IFMBE Proceedings 1. Springer, Berlin, Heidelberg, pp. 137–140.
- Paganetti, H. et al. (1997). "Calculation of relative biological effectiveness for proton beams using biological weighting functions". In: *Int. J. Radiat. Oncol. Biol. Phys.* 37.3, pp. 719–729.
- Pflugfelder, D. et al. (2008). "Worst case optimization: a method to account for uncertainties in the optimization of intensity modulated proton therapy". In: *Phys. Med.*

- Biol.* 53. Copyright: Institute of Physics and Engineering in Medicine, pp. 1689–1700.
- Pfuhl, T. et al. (2018). “Dose build-up effects induced by delta electrons and target fragments in proton Bragg curves—measurements and simulations”. In: *Phys. Med. Biol.* 63.
- Podgoršak, E. B., ed. (2005). *Radiation Oncology Physics: A Handbook for Teachers and Students*. IAEA.
- (2010). *Radiation Physics for Medical Physicists*. Ed. by E. Greenbaum. 2nd ed. Springer-Verlag Berlin Heidelberg.
- PTW (2017). *Acrylic and RW3 Slab Phantoms*. URL: [http://www.ptw.de/acrylic\\_and\\_rw3\\_slab\\_phantoms0.html](http://www.ptw.de/acrylic_and_rw3_slab_phantoms0.html).
- (2017/18). *Detectors*.
- RaySearch (2017a). *Proton Monte Carlo dose calculation in RayStation*. White paper. Stockholm, Sweden.
- (2017b). *RayStation 7: User Manual*. RaySearch Laboratories.
- Roberson, P. L. et al. (2008). “Radiographic film dosimetry for IMRT fields in the near-surface buildup region”. In: *J Appl Clin Med Phys* 9.4, pp. 87–97.
- RSD (2014). *The Alderson Radiation Therapy Phantom*. URL: [http://rsdphantoms.com/rt\\_art.htm](http://rsdphantoms.com/rt_art.htm).
- Saini, J. et al. (2017). “Dosimetric evaluation of a commercial proton spot scanning Monte-Carlo dose algorithm: comparisons against measurements and simulations”. In: *Phys. Med. Biol.* 62, pp. 7659–7681.
- Schaffner, B. (2008). “Proton dose calculation based on in-air fluence measurements”. In: *Phys. Med. Biol.* 53, pp. 1545–1562.
- Schmitt, G. et al. (1983). “Neutron and neutron-boost irradiation of soft tissue sarcomas: A 4.5 year analysis of 139 patients”. In: *Radiotherapy and Oncology* 1.
- Schwarz, M. (2011). “Treatment planning in proton therapy”. In: *Eur. Phys. J. Plus* 126.67.
- Shani, G. (2001). *Radiation Dosimetry: Instrumentation and Methods*. 2nd ed. CRC Press LLC.
- Shen, J. et al. (2015). “Impact of range shifter material on proton pencil beam spot characteristics”. In: *Med. Phys.* 42.3, pp. 1335–40.
- St. Vincentius-Kliniken Karlsruhe (2015). *Patienteninformation: Strahlentherapie bösartiger Erkrankungen*.
- Stock, M. and Georg, D. (2018). *Ion beam therapy*. Basic Seminar: Medical Physics VIII - Physical Fundamentals of Radio Oncology, Medical University of Vienna.
- Suit, H. and Spiro, I. (1994). “Role of Radiation in the Management of Adult Patients With Sarcoma of Soft Tissue”. In: *Seminars in Surgical Oncology* 10, pp. 347–356.
- Titt, U. et al. (2010). “Adjustment of the lateral and longitudinal size of scanned proton beam spots using a pre-absorber to optimize penumbrae and delivery efficiency”. In: *Phys. Med. Biol.* 55, pp. 7097–7106.
- Unkelbach, J. et al. (2009). “Reducing the sensitivity of IMPT treatment plans to setup errors and range uncertainties via probabilistic treatment planning”. In: *Med. Phys.* 36.1. American Association of Physicists in Medicine, pp. 149–163.

- Wagner, A. (2006). “Energiesmessung & Teilchenidentifikation”. Johannes Gutenberg Universität Mainz.
- Wesener, J. and Günther, S. (s.a.). *Auger-Elektronenspektroskopie*. RÖMPP. URL: <https://roempp.thieme.de/roempp4.0/do/data/RD-01-04280>.
- Westerly, D. et al. (2013). “A generalized 2D pencil beam scaling algorithm for proton dose calculation in heterogeneous slab geometries”. In: *Med. Phys.* 40.6.
- Wiegel, T. (2018). *Strahlentherapie und Radioonkologie: Patienteninformationen - Wie ist der typische Ablauf Ihrer Strahlentherapie*. Universitätsklinikum Ulm. URL: <https://www.uniklinik-ulm.de/strahlentherapie-und-radioonkologie/patienteninformationen/wie-ist-der-typische-ablauf-ihrer-strahlentherapie.html>.
- www.nuclear-power.net (s.a.). *Interaction of Gamma Radiation with Matter*. Nuclear Power. URL: <https://www.nuclear-power.net/nuclear-power/reactor-physics/interaction-radiation-matter/interaction-gamma-radiation-matter/>.
- Yanagi, T. et al. (2009). “Dose-volume histogram and dose-surface histogram analysis for skin reactions to carbon ion radiotherapy for bone and soft tissue sarcoma”. In: *Radiother. Oncol.* 95, pp. 60–65.
- Zurlo, A. et al. (2000). “The role of proton therapy in the treatment of large irradiation volumes: a comparative planning study of pancreatic and biliary tumors”. In: *Int. J. Radiation Oncology Biol. Phys.* 48.1, pp. 277–288.



# Appendix

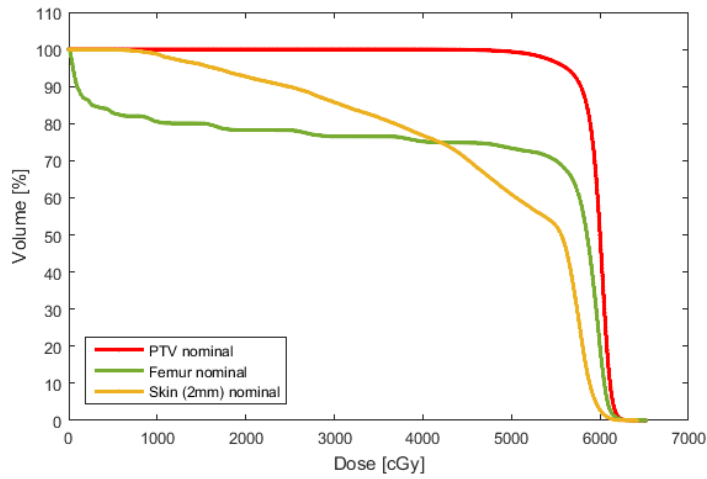


Figure A.1: Dose-volume histogram of P4: nominal case (own illustration)

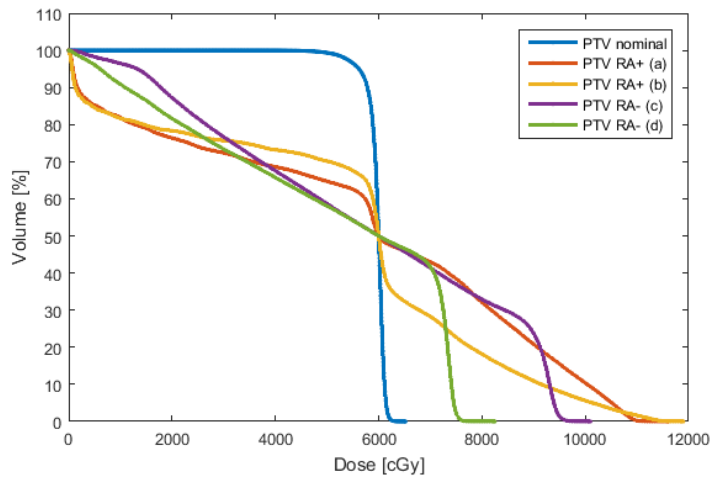


Figure A.2: Dose-volume histogram of P4: comparisons of nominal and perturbed cases regarding the PTV (own illustration)

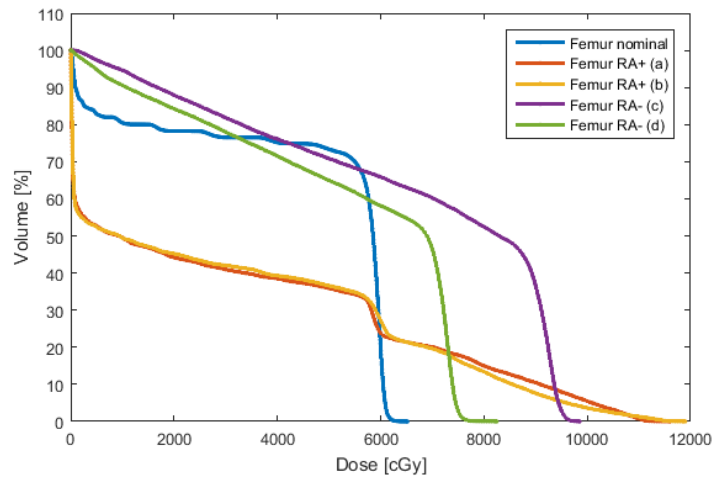


Figure A.3: Dose-volume histogram of P4: comparisons of nominal and perturbed cases regarding the femur (own illustration)

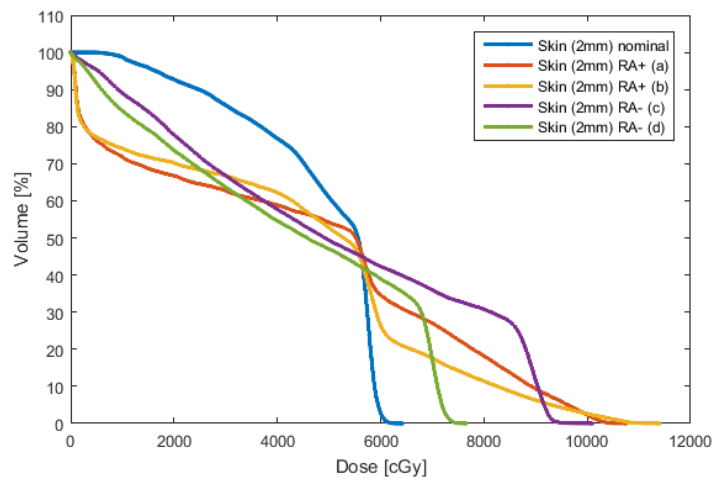


Figure A.4: Dose-volume histogram of P4: comparisons of nominal and perturbed cases regarding the 2 mm skin treatment area (own illustration)

**CALIBRATION CERTIFICATE**  
**No. 1402263**



PTW-Freiburg, Lörracher Str. 7, 79115 Freiburg, Germany ☎ +49-(0)761- 49055-0 FAX +49-(0)761- 49055-70 E-Mail info@ptw.de

**Calibration Object**

Radiation Detector

Detector **[REF] TM34045 [SN] 001540**  
 Detector Type Ionization Chamber

Manufacturer PTW-Freiburg  
 Customer EBG MedAustron GmbH Order No. : AU1401566  
 Marie Curie-Strasse 5 Order Date : 2014-05-26  
 A-2700 Wiener Neustadt

**Calibration Results**

Measuring Quantity Absorbed Dose to Water ( $D_w$ )

Detector Calibration Factor  $N_{D,w} = 1.329 \cdot 10^9 \text{ Gy / C}$

Beam Quality Correction	Beam Quality	Correction Factor $k_Q$	Uncertainty
	$^{60}\text{Co}$	1.000	1.1 %

Reference Conditions  
 Beam Quality:  $^{60}\text{Co}$   
 Temperature: 293.2 K (20°C)  
 Air Pressure: 1013.25 hPa  
 Relative Humidity: 50%  
 Chamber Voltage/Polarity: + 300 V  
 Ion Collection Efficiency: 100 %

Calibration Date **2014-06-05**  
 Recalibration Interval 2 years (recommended)

Freiburg, 2014-06-06

PTW-Freiburg  
 Physikalisch-Technische  
 Werkstätten Dr. Pöchlau GmbH

*Peiffer*  
 (Signature)

Figure A.5: Calibration certificate of Advanced Markus chamber (MedAustron)

**Calibration Conditions and Set-up**

Climatic Conditions	Temperature Range: ( 294.2 ± 3 ) K / ( 21 ± 3 ) °C Air Pressure Range: ( 1000 ± 50 ) hPa Rel. Humidity Range: ( 40 ± 20 ) %										
Beam Quality and Geometry	<table border="1" style="width: 100%; border-collapse: collapse;"> <thead> <tr> <th style="text-align: left;">Quality</th> <th style="text-align: left;">Filter [mm]</th> <th style="text-align: left;">HVL [mm]</th> <th style="text-align: left;">SDD [cm]</th> <th style="text-align: left;">Size [cm]</th> </tr> </thead> <tbody> <tr> <td><sup>60</sup>Co</td> <td style="text-align: center;">-</td> <td style="text-align: center;">-</td> <td style="text-align: center;">100</td> <td style="text-align: center;">10 x 10</td> </tr> </tbody> </table> <p style="margin-left: 40px;">           Quality: Beam qualities according to DIN 6809-5 / DIN 6809-4            Filter: Total filtration (inherent and additional filters)            HVL: Half value layer at the point of measurement            SDD: Distance between radiation source and reference point            Size: Field size at reference point, diam. = Field Diameter            Reference depth: 5 g cm<sup>-2</sup> H<sub>2</sub>O         </p>	Quality	Filter [mm]	HVL [mm]	SDD [cm]	Size [cm]	<sup>60</sup> Co	-	-	100	10 x 10
Quality	Filter [mm]	HVL [mm]	SDD [cm]	Size [cm]							
<sup>60</sup> Co	-	-	100	10 x 10							
Detector Arrangement	The membrane faced towards the radiation source Reference point position at stated measuring depth / distance to the radiation source (For further information see manual and data sheet of detector.)										
Dose and Dose Rate	Absorbed Dose To Water : min.: 5.0 · 10 <sup>-2</sup> Gy / max.: 5.0 Gy Absorbed Dose To Water rate : min.: 50 mGy/min / max.: 300 mGy/min										
Polarity Effect	≤ 0.5 % ( not accounted for in the detector calibration factor )										
Saturation Correction Factor	k <sub>s</sub> = 1.000										
Leakage	Negligible during calibration										

**Remarks**

1. The uncertainty stated corresponds to the double standard deviation (k=2). The standard deviation was calculated according to ISO GUM from the partial uncertainties arising from the standard used, the calibration procedure, the environmental conditions and short time effects of the object of measurement. The uncertainties stated are composed of the uncertainties of the calibration procedure and those of the specimen during calibration. A share for the long-term instability of the object under calibration is not included.
2. The calibration is traceable to national standards of the German National Laboratory, PTB, Braunschweig. This calibration certificate may not be reproduced other than in full except with the permission of the issuing laboratory. This certificate is valid only with the ionization chamber showing the intact sticker with the certificate number. Calibration factors of chambers having been opened for repair are not comparable to previous calibrations. Calibration certificates without signature are not valid.
3. The components of the calibration object fully comply with the respective specifications given in the data sheet and user manual.
4. The calibration factor presented in this certificate can be equally used for Absorbed-Dose-To-Water determination with dosimetry protocols IAEA TRS 398, AAPM TG-51 und DIN 6800-2. However, it must be guaranteed that the reference temperature given in this certificate is in agreement with the reference temperature of the chosen dosimetry protocol. In the case of disagreement of reference temperatures an appropriate correction of the presented calibration factor with respect to the dosimetry protocols reference temperature must be applied.

# CALIBRATION CERTIFICATE

No. 1402262



PTW-Freiburg, Lörracher Str. 7, 79115 Freiburg, Germany ☎ +49-(0)761- 49055-0 FAX +49-(0)761- 49055-70 E-Mail info@ptw.de

## Calibration Object

Radiation Detector

Detector **[REF] TM34001 [SN] 002460**  
Detector Type Ionization Chamber

Manufacturer PTW-Freiburg  
Customer EBG MedAustron GmbH Order No. : AU1401566  
Marie Curie-Strasse 5 Order Date : 2014-05-26  
A-2700 Wiener Neustadt

## Calibration Results

Measuring Quantity Absorbed Dose to Water ( $D_w$ )

Detector Calibration Factor  $N_{D,w} = 8.396 \cdot 10^7 \text{ Gy / C}$

Beam Quality Correction	Beam Quality	Correction Factor $k_Q$	Uncertainty
	$^{60}\text{Co}$	1.000	1.5 %

Reference Conditions Beam Quality:  $^{60}\text{Co}$   
Temperature: 293.2 K (20°C)  
Air Pressure: 1013.25 hPa  
Relative Humidity: 50%  
Chamber Voltage/Polarity: + 200 V  
Ion Collection Efficiency: 100 %

Calibration Date **2014-06-03**  
Recalibration Interval 2 years (recommended)

Freiburg, 2014-06-06

PTW-Freiburg  
Physikalisch-Technische  
Werkstätten Dr. Pöchlau GmbH

(Signature)

Page 1 / 2

Figure A.7: Calibration certificate of Roos chamber (MedAustron)

**Calibration Conditions and Set-up**

Climatic Conditions	Temperature Range:	( 294.2 ± 3 ) K / ( 21 ± 3 ) °C			
	Air Pressure Range:	( 1000 ± 50 ) hPa			
	Rel. Humidity Range:	( 40 ± 20 ) %			
Beam Quality and Geometry	Quality	Filter [mm]	HVL [mm]	SDD [cm]	Size [cm]
	<sup>60</sup> Co	-	-	100	10 x 10
	Quality:	Beam qualities according to DIN 6809-5 / DIN 6809-4			
	Filter:	Total filtration (inherent and additional filters)			
	HVL:	Half value layer at the point of measurement			
	SDD:	Distance between radiation source and reference point			
	Size:	Field size at reference point, diam. = Field Diameter			
	Reference depth:	5 g cm <sup>-2</sup> H <sub>2</sub> O			
Detector Arrangement	Inscription "Focus" faced towards the radiation source Reference point position at stated measuring depth / distance to the radiation source (For further information see manual and data sheet of detector.)				
Dose and Dose Rate	Absorbed Dose To Water :	min.: 5.0 · 10 <sup>-2</sup> Gy / max.: 5.0 Gy			
	Absorbed Dose To Water rate :	min.: 50 mGy/min / max.: 300 mGy/min			
Polarity Effect	≤ 0.2 % ( not accounted for in the detector calibration factor )				
Saturation Correction Factor	k <sub>S</sub> = 1.000				
Leakage	Negligible during calibration				

**Remarks**

- The uncertainty stated corresponds to the double standard deviation (k=2). The standard deviation was calculated according to ISO GUM from the partial uncertainties arising from the standard used, the calibration procedure, the environmental conditions and short time effects of the object of measurement. The uncertainties stated are composed of the uncertainties of the calibration procedure and those of the specimen during calibration. A share for the long-term instability of the object under calibration is not included.
- The calibration is traceable to national standards of the German National Laboratory, PTB, Braunschweig. This calibration certificate may not be reproduced other than in full except with the permission of the issuing laboratory. This certificate is valid only with the ionization chamber showing the intact sticker with the certificate number. Calibration factors of chambers having been opened for repair are not comparable to previous calibrations. Calibration certificates without signature are not valid.
- The components of the calibration object fully comply with the respective specifications given in the data sheet and user manual.
- The calibration factor presented in this certificate can be equally used for Absorbed-Dose-To-Water determination with dosimetry protocols IAEA TRS 398, AAPM TG-51 und DIN 6800-2. However, it must be guaranteed that the reference temperature given in this certificate is in agreement with the reference temperature of the chosen dosimetry protocol. In the case of disagreement of reference temperatures an appropriate correction of the presented calibration factor with respect to the dosimetry protocols reference temperature must be applied.